

SARS-CoV-2 PROTEIN-BASED DETECTION USING LOCALIZED SURFACE PLASMON RESONANCE

A Thesis Submitted to the Committee of Graduate Studies
in Partial Fulfillment of the Requirements for the Degree of Master of Science
in the Faculty of Arts and Science

TRENT UNIVERSITY

Peterborough, Ontario, Canada

© Copyright by **Tyra M. Lewis 2022**

Environmental and Life Sciences M.Sc Graduate Program

September 2022

Abstract

SARS-CoV-2 Protein-Based Detection Using Localized Surface Plasmon Resonance

Tyra M. Lewis

During the COVID-19 pandemic, nucleic acid and antibody-based testing methods were heavily relied upon, but can be costly, time-consuming and exhibit high false -negative and -positive rates. Thus, alternative strategies are needed. Viral antigens such as the SARS-CoV-2 spike (S) glycoprotein are critical in the function of the virus and useful as diagnostic biomarkers for viral infections. For biosensing applications, aptamers are suitable high-affinity and cost-effective binding partners for their specific targets. Using localized surface plasmon resonance (LSPR), real-time, rapid acquisition of results can be achieved, essential for improving the efficacy of a sensor. Herein, LSPR aptamer sensors were fabricated for the detection of the SARS-CoV-2 protein. Data indicate that the best performing aptasensor was the streptavidin-biotin sensor, while the current gold aptasensor exhibited lower sensitivity and the fabrication of the carboxyl aptasensor was unsuccessful. The S1 aptamer selectively bound the S1 protein with high binding affinity. Excellent shelf-life stability, reusability, and high recovery in complex matrices was also maintained. Additionally, a receptor binding domain (RBD) functionalized sensor was fabricated to examine the interactions with angiotensin converting enzyme 2 (ACE2), for future assessment of inhibitors used in drug therapies. Overall, LSPR has been demonstrated as a viable tool for measuring SARS-CoV-2 related aptamer-protein and protein-protein interactions, and this strategy may be applied to other viral or non-viral antigen targets.

Keywords: Antigen-based Detection, ACE2, Coronavirus, COVID-19, Localized Surface Plasmon Resonance, Inhibition, RBD, SARS-CoV-2, Spike Protein

Abbreviations: ACE2, angiotensin converting enzyme 2; AuNPs, gold nanoparticles; BSA, bovine serum albumin; COVID-19, coronavirus 2019; DNA, deoxyribonucleic acid; EDC, 1-Ethyl-3-(3-dimethylaminopropyl)carbodiimide; ELISA, enzyme-linked immunosorbent assay; LOD, limit of detection; LOQ, limit of quantification; LSPR, localized surface plasmon resonance; MERS-CoV, middle eastern respiratory syndrome coronavirus; NHS, N-Hydroxysuccinimide; PCR, polymerase chain reaction; PDB, protein data bank; POCT, point-of-care testing; RBD, receptor binding domain; RNA, ribonucleic acid; RU, resonance units or response units; SARS-CoV-2, severe acute respiratory syndrome beta-coronavirus 2; ssDNA, single-stranded deoxyribonucleic acid

Acknowledgments

I wish to thank all the persons whose assistance and encouragement contributed to the completion of this project and the advancement of my education at Trent University.

I cannot go without recognizing the invaluable guidance and support offered by my supervisor, Dr. Sanela Martic, during my studies. I wish to thank her especially, for her encouragement and for the many opportunities she exposed me to, to expand my knowledge and experiences. Without her persistence over the years, my goals and those of this project would not have been fulfilled. I will forever be grateful.

I also wish to extend my sincere gratitude to Dr. Barry Saville and Dr. Neil Emery for their guidance and encouraging words shared throughout my MSc journey.

A sincere thank you to the Martic Lab group members (2019-2022), for their continued support and feedback throughout my studies; Uncle Bruce, Andria & family, Kahlea, Galair, Lanae and Shacia for their unremitting and unwavering support, upliftment, and kind words of encouragement (and reminders to sleep) that kept me going.

Lastly, I wish to express my whole-hearted love and appreciation to my parents, George, and Wendy Lewis. Their never-ending support has greatly contributed to all my successes. My academic accomplishments would not have been possible without them. Thank you for always being there for me, and for your advice and reassurance through all the tough times.

“Watch out that you do not lose what we have worked so hard to achieve. Be diligent so that you receive your full reward.” 2 John 1:8

Table of Contents

Abstract.....	ii
Acknowledgments	iv
List of Figures.....	vii
List of Tables	xi
Chapter 1: Introduction and proposed research strategy for the analysis of SARS-CoV-2 protein interactions.....	1
1.1 Introduction	1
1.2 Significance.....	2
1.3 Biological relevance of the SARS-CoV-2	2
1.4 Strategies for detection of SARS-CoV-2	5
1.4.1 Nucleic acid detection.....	8
1.4.2 Antibody detection.....	10
1.4.3 Antigen detection	12
1.5 Biosensors for SARS-CoV-2 antigen detection.....	13
1.5.1 Bioreceptors used for detection of SARS-CoV-2 antigens.....	14
1.5.2 Biosensor transducer platforms for SARS-CoV-2 antigen detection	19
1.6 Proposed research strategy and objectives	26
Chapter 2: Localized surface plasmon resonance aptasensor for selective detection of SARS-CoV-2 S1 protein.....	29
2.1 Introduction	29
2.2 Material and methods	34
2.2.1 Chemicals and reagents.....	34
2.2.2 LSPR measurements	35
2.2.3 Fabrication of LSPR aptasensor.....	36
2.2.4 S1 protein detection and quantification	37
2.2.5 Selectivity studies	37
2.2.6 S1 protein detection in artificial saliva	38
2.2.7 S1 protein detection in serum albumin	38
2.2.8 Shelf-life stability of sensor chip	39
2.2.9 Repeatability and reusability of sensor	39
2.2.10 Docking modeling of S1 protein and S1 aptamer.....	40
2.2.11 Scanning electron microscopy	40
2.3 Results and discussion.....	40
2.3.1 Aptasensor fabrication	42
2.3.2 Optimization of aptamer concentration, buffer composition and regeneration conditions.....	44
2.3.3 Quantification of S1 protein with S1 aptasensor	46
2.3.4 Selectivity of aptasensor for S1 protein	47

2.3.5	S1 aptasensor selectivity for S1 protein across related coronaviruses.....	51
2.3.6	S1 protein detection in spiked artificial saliva and serum albumin	53
2.3.7	Repeatability and shelf-life	54
2.4	Conclusions	56
Chapter 3: Evaluation of amide and gold-thiol covalent coupling methods for studying aptamer-protein interactions		59
3.1	Introduction	59
3.2	Materials and Methods	66
3.2.1	Chemicals and reagents.....	66
3.2.2	LSPR measurements	67
3.2.3	Fabrication and testing of the S1 aptasensor on a bare Au surface	67
3.2.4	Testing aptamer-protein interactions on functionalized carboxyl sensors..	69
3.3	Results and Discussion.....	71
3.3.1	Au-thiol coupling using aptamer functionalized AuNP sensor surface.....	71
3.3.2	Amide coupling using carboxyl sensors	78
3.4	Conclusions	92
Chapter 4: Assessing SARS-CoV-2 RBD-ACE2 interactions using a LSPR protein functionalized carboxyl sensor.....		94
4.1	Introduction	94
4.2	Materials and Methods	98
4.2.1	Chemicals and reagents.....	98
4.2.2	LSPR measurements	98
4.2.3	Screening ACE2 interactions with a RBD functionalized carboxyl surface	99
4.3	Results and discussion.....	100
4.3.1	Optimization of protein-protein regeneration conditions	100
4.3.2	Evaluation of ACE2 protein with RBD functionalized surface.....	104
4.3.3	Effects of surface coverage on ACE2 binding to the RBD functionalized surface	107
4.4	Significance and future applications	109
4.5	Conclusion.....	111
Chapter 5: Summary and Future Work.....		112
5.1	Summary	112
5.2	Future Work	115
References		118
Appendix i: Supplementary Information (Chapter 2)		139
Appendix ii: Supplementary Information (Chapter 3)		161
Appendix iii: Supplementary Information (Chapter 4)		166
Appendix iv: Copyright Releases		168

List of Figures

Figure 1.1. Illustration of the SARS-CoV-2 with structural proteins identified and depiction of SARS-CoV-2 attachment to the host cell by ACE2 binding. Created using biorendor.com.	3
Figure 1.2. Timeline for detection of SARS-CoV-2 antibodies as a function of infection period; Figure reprinted from Ghaffari et al., (2020). ⁵¹	11
Figure 1.3. Illustration of common components of a biosensor. Created using biorendor.com.	13
Figure 1.4. (A) Electrochemical aptasensor based on the conformational change of a methylene blue redox tagged aptamer for detection of the SARS-CoV-2 S1 protein ⁹⁹ ; (B) Illustration of concept of sampling procedure for application of a CNT-FET antibody based biosensor for detection of SARS-CoV-2 S1 antigen ⁹⁷ ; (C) Scheme of SPR set up for the detection of SARS-CoV-2 N protein using antibody functionalized AuNP surface with a secondary AuNP/antibody conjugate and the linear range SPR signal as a function of N protein concentration ¹⁰⁷	21
Figure 1.5. General concept of (A) SPR <i>versus</i> (B) LSPR operational principle. Created using biorendor.com.	24
Figure 1.6. Illustration of the flow through mechanism and typical sensorgram generated for LSPR measurement. Created using biorendor.com.	25
Figure 1.7. Various covalent and capture coupling strategies that are being explored along with the ideal immobilization targets using differently modified AuNP sensor surfaces. Created using biorendor.com.	27
Figure 2.1. (A) Illustration of SARS-CoV-2 virus and structure of the full-length S protein. (B) Structure of the SARS-CoV-2 S1 protein, (C) RBD protein, (D) S2 protein; (PDB: 6VSB structure of protein subunits obtained using Discovery Studio Visualizer Software).	31
Figure 2.2. Secondary and tertiary structures of the S1 aptamer, S1 aptamer-T and N aptamer-T (2D structures were generated using Mfold software and 3D structures were generated using RNAComposer).	42

Figure 2.3. (A) Photo of the LSPR chip; (B) Schematic of 2-channel sensor with flow system, and depiction of differential immobilization of S1- and N-aptamers on channel 2 and 1, respectively; (C) Representative LSPR sensorgrams for the fabrication of aptasensors using 2-channel system. The streptavidin-biotin-AuNP surface functionalization (1) on channel 1 and 2, followed by biotinylated S1-aptamer immobilization (2) on channel 2, then N-aptamer immobilization on channel 1 (3) ([streptavidin] = 0.5 μM ; [aptamer] = 50 $\mu\text{g mL}^{-1}$; flow rate = 20 $\mu\text{L min}^{-1}$).....43

Figure 2.4. (A) Representative LSPR sensorgrams for S1 protein binding to the S1 aptasensor as a function of S1 protein concentrations; (B) Plot of LSPR signal change as a function of S1 protein concentrations derived from sensorgram (A) ([S1 protein] = 0-32 nM (0-2.5 $\mu\text{g mL}^{-1}$); flow rate = 10 $\mu\text{L min}^{-1}$).....47

Figure 2.5. Representative LSPR sensorgrams of S1, RBD, S2 and BSA protein binding to (A) S1 aptamer sensor and (B) N aptamer-T sensor. (C) Plot of LSPR signal differences for binding of S1, RBD, S1 and BSA proteins to N aptamer-T sensor or S1 aptamer sensor ([Proteins] = 2.5 $\mu\text{g mL}^{-1}$, (N-T or S1 aptamer) = 50 $\mu\text{g mL}^{-1}$); (D) Molecular docking modelling of S1 protein and S1 aptamer using PatchDock WebServer and visualized with Discovery Studio Visualizer Software.....49

Figure 2.6. (A) LSPR sensorgrams and (B) plot of LSPR signal change for SARS-CoV-2 S1 and SARS-CoV S1 protein binding to S1 aptasensor ([Protein] = 2.5 $\mu\text{g mL}^{-1}$; [S1 aptamer] = 50 $\mu\text{g mL}^{-1}$; Flow rate = 10 $\mu\text{L min}^{-1}$; dissociation = 15 min; signal change measured at 1600 s). (C) LSPR sensorgrams and (D) plot of LSPR signal change for SARS-CoV-2 S1 protein in spiked buffer solution (channel 1 + 2) compared to 100x diluted spiked artificial saliva solution (channel 2) ([S1 protein] = 2.5 $\mu\text{g mL}^{-1}$; signals represent average of triplicate measurements with standard deviation shown as error bars).....53

Figure 3.1. Schematic of elements of the LSPR sensor surface and various surface chemistries used for attachment of ligands. Created using biorendor.com.61

Figure 3.2. Schematic representation of the sensor fabrication procedure (A) of a carboxyl-graphene oxide-peptide based SPR chip from a bare Au sensor for detection of human chorionic gonadotropin protein¹⁵; (B) for direct attachment of a thiolated aptamer for detection of virus coat protein, PSA-H by imaging SPR¹²; (C) of an antibody-antigen based

sensor functionalized through amide coupling on a carboxymethyl dextran chip for detection of matrix metalloproteinase-9. ²²	63
Figure 3.3. Design of the S1 aptasensor fabricated on a bare Au surface using a SS-S1 aptamer, and cystamine surface blocker.	71
Figure 3.4. Illustration of bare Au sensor chip cleaning process for (A) protocol 1 or (B) protocol 2 to achieve a cleaned bare Au sensor surface; Created using Biorender.com. (C) Representative LSPR sensorgram of surface fabrication with the immobilization solution, following a 5- or 120- min. piranha solution etching. Immobilization solution = [aptamer] = 50 µg/mL and [cystamine] = 250 µg/mL; Flow rate = 20 µL/min; Dissociation time = 15 min.	74
Figure 3.5. (A) Representative LSPR sensorgram and (B) plots of LSPR signals for the blank buffer, BSA and S1 protein screening following the ligand immobilization procedure; (C) Comparison of LSPR signals generated using the S1 aptasensor fabricated on the bare Au surface or the streptavidin-biotin surface; [Proteins] = 2.5 µg/mL; Flow rate = 10 µL/min.	77
Figure 3.6. (A) Scheme of process of activation of carboxyl coated surface using EDC/NHS chemistry for attachment of an aminated ligand. (B) Representative sensorgram demonstrating the sensor fabrication process.	79
Figure 3.7. Illustration of sensor fabrication protocol for preparation of the (A) aptamer or (B) protein functionalized carboxyl sensor chips. Created using Biorender.com.	81
Figure 3.8. (A) Representative sensorgram and (B) average LSPR signal change with sequential addition of RBD protein; for each injection [RBD] = 10 µg/mL; flow rate = 10 µL/min.	85
Figure 3.9. (A) Representative LSPR signals and (B) plot of LSPR signal differences showing RBD protein attachment at concentration of 1, 5, 10, 25 or 50 µg/mL to the activated carboxyl coated AuNP surface; flow rate = 10 µL/min; $t_f \approx 740$ s.	87
Figure 3.10. (A) Structure of the SARS-CoV-2 RBD protein (PDB ID: 6VSB); structure of protein subunits obtained using Discovery Studio Visualizer Software. Tertiary structures of the (B) S1 and (C) S1-T aptamers generated using RNAComposer. ^{57,58} Molecular docking modelling of SARS-CoV-2 RBD protein and (D) S1 and (E) S1-T	

aptamer using PatchDock WebServer and visualized with Discovery Studio Visualizer Software.⁵⁸⁻⁶⁰91

Figure 4.1. (A) Structure of the SARS-CoV-2 RBD bound to ACE2 (PDB: 6M0J). Fitted SPR sensorgrams representing (B) SARS-CoV-2 RBD binding to ACE2 surface and respective binding affinities; Figure (B) reproduced from Lan et al., (2020).³96

Figure 4.2. (A) Schematic illustration and (B) representative LSPR sensorgram demonstrating binding of the ACE2 protein to RBD functionalized sensor and (2) regeneration of the functionalized surface; [RBD] = 10 $\mu\text{g/mL}$; [ACE2] = 100 nM; [HCl] = 5 mM; flow rate for RBD immobilization (10 $\mu\text{L/min}$), ACE2 binding (10 $\mu\text{L/min}$), HCl regeneration (150 $\mu\text{L/min}$).....101

Figure 4.3. (A) Representative LSPR signals and (B) plot of LSPR signal comparison with blank buffer, BSA and ACE2 using the RBD functionalized carboxyl/AuNP surface; immobilized [RBD] = 25 $\mu\text{g/mL}$; [BSA and ACE2] = 100 nM; flow rate = 10 $\mu\text{L/min}$; regeneration of RBD-ACE2 interaction with 10 mM HCl, flow rate = 150 $\mu\text{L/min}$105

Figure 4.4. Comparison of LSPR signals of ACE2 binding as a function of RBD loading during the immobilization step; [RBD] = 1, 10, or 25 $\mu\text{g/mL}$, [ACE2] = 100 nM; flow rate = 10 $\mu\text{L/min}$; regeneration with 10 mM HCl, flow rate = 150 $\mu\text{L/min}$108

Figure 4.5. Illustration of protein-protein interaction system showing the mechanism of virus neutralization. Created using Biorender.com.....109

List of Tables

Table 1.1. Current diagnostic strategies used for determination of COVID-19	6
Table 1.2. Examples of aptamers designed for detection of SARS-CoV-2 antigens.....	16
Table 4.1. Results of regeneration using 1-10 mM HCl solutions after ACE2 binding to the immobilized RBD on the activated carboxyl surface.	103

Chapter 1:

Introduction and proposed research strategy for the analysis of SARS-CoV-2 protein interactions

1.1 Introduction

The first confirmed case of the coronavirus disease 2019 (COVID-19) was reported in Wuhan, China late December 2019.^{1,2} High-throughput sequencing revealed that this was a case of a novel SARS-like virus, now known as the severe acute respiratory syndrome beta-coronavirus 2, or “SARS-CoV-2”.²⁻⁵ By the end of January 2020, the global spread of COVID-19 had begun to make its impact in four different countries outside of China, including Germany, Japan, the USA and Vietnam.⁶ With a spike in the number of coronavirus cases reaching >120,000 and >4,000 related deaths worldwide, the World Health Organization (WHO) declared COVID-19 a pandemic on March 11, 2020.⁶⁻⁸ Since then, the number of cases have continued to increase, affecting millions of persons everywhere.

The history of coronavirus outbreaks dates to as early as 2003. The 2003 SARS-CoV outbreak in China and the 2012 Middle East Respiratory Syndrome Coronavirus (MERS-CoV) outbreak in the Saudi Arabia hold precedents over the current 2019 SARS-

CoV-2 pandemic.^{3,9} Although these events did not present as widespread impact as the current pandemic, they have significantly contributed to today's knowledge of the SARS-CoV-2 and set the foundation for the growing knowledge into advanced diagnosis, treatment and detection of COVID-19.¹⁰⁻¹³

1.2 Significance

The significant global impact and rapid spread of COVID-19 has demonstrated the immediate need for alternative solutions to mitigating the effects of the pandemic. The inaccessibility to efficient and effective solutions to rapid viral detection of SARS-CoV-2 was a main challenge that delayed authorities' instantaneous control of the pandemic. During the pandemic, health professionals were heavily reliant on both rapid diagnostic tests and confirmatory tests for patient diagnosis. However, the conventional approaches to viral detection are generally costly, labor-intensive, time consuming and/or have relatively slow response time.^{3,11,13} Considering the widespread consequences of the current pandemic, significant progress has since been made within the scientific community toward the development and advancement of detection methods and treatment for viral infections.

1.3 Biological relevance of the SARS-CoV-2

The SARS-CoV-2 is a single-strand enveloped ribonucleic acid (RNA) virus, belonging to the Coronaviridae family and the *betacoronavirus* genus.^{2,14,15} The coronavirus encodes several structural proteins including the nucleocapsid (N), spike (S), envelope (E) and membrane (M) protein (Figure 1.1). The structural proteins are important to the general

function of the virus and the regulation of viral gene expression.^{3,14} Located in the virus' envelope, the M protein is the most abundant of the structural proteins. It has roles in maintaining the shape of the viral envelope, viral fusion, and assembly. The E protein is the smallest in size but plays a major part in development of the virions in assembly, pathogenesis, and release. The N protein forms a viral capsid outside of the RNA genome, as depicted in Figure 1.1. It facilitates the nucleic synthesis, replication, and transcription. Lastly, the S glycoprotein protrudes the surface of the virus and plays a vital role in viral attachment and entry into host cells.

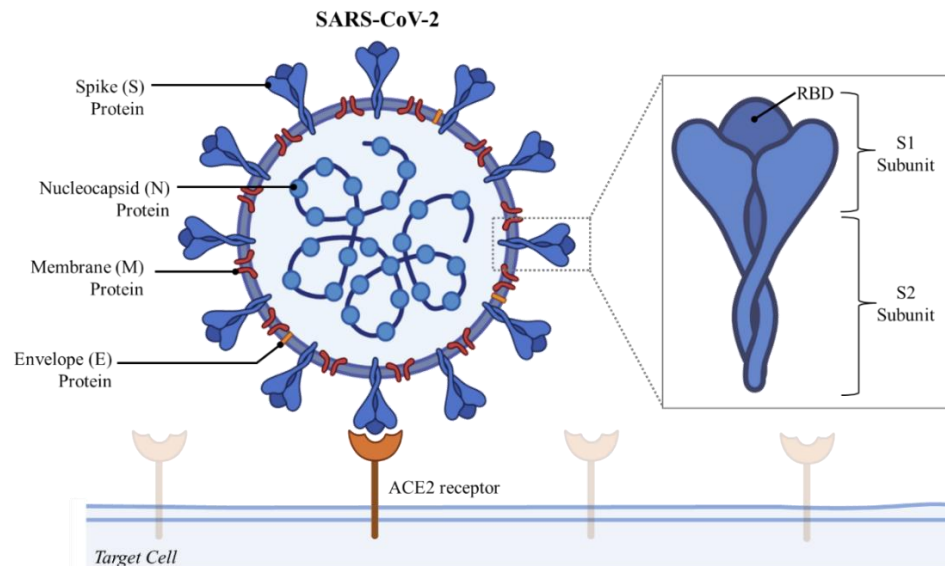


Figure 1.1. Illustration of the SARS-CoV-2 with structural proteins identified and depiction of SARS-CoV-2 attachment to the host cell by ACE2 binding. Created using biorendor.com.

The S protein is composed of two subunits, named S1 and S2, each having their own responsibilities (Figure 1.1). The S2 subunit provides structural support for the S protein and is critical in viral fusion and entry of the virus into the host cell. On the other

hand, the S1 subunit is important for the attachment of the virus to the host cell receptor. Specifically, the receptor binding domain (RBD) located within the S1 subunit is a key component in facilitating any coronavirus infection.^{4,14,16} The SARS-CoV and SARS-CoV-2 share similarities in the genome structure of S (76-78%), S2 (73-76%) and RBD (50-53%).³ With ~50 conserved amino acids within the S1 subunit, this makes the S protein an important tool for further understanding of the coronavirus activity and the development of new diagnostic tools, therapeutics and vaccines.^{3,16}

Previous understanding of the infection mechanism of SARS-CoV also provided insight to the function and activity of the SARS-CoV-2. It was known that cells expressing the cellular receptor, angiotensin converting enzyme 2 (ACE2) bind the SARS-CoV RBD, thus resulting in the viral infection (Figure 1.1).^{2-4,17,18} Research into this mechanism revealed that, the RBD-ACE2 binding initiates S protein fusion and viral entry, first through cleavage of the S1/S2 boundary, leading to the activation of the S2 subunit, and subsequently resulting in membrane fusion.^{4,17,18} Furthermore, considering the similarity in sequences between the novel coronavirus and its predecessor, this understanding of the attack mechanism involving the coronavirus and ACE2 also translates to the understanding of the activity of SARS-CoV-2 infections.^{3,4,16,17,19-21} However, the binding affinities for SARS-CoV and SARS-CoV-2 RBD with the ACE2 differ ($K_D = 31$ nM and 4.7 nM, respectively), likely as a result of the small differences in amino acid sequences.^{4,16} Overtime, the evolution of SARS-CoV-2 has also resulted in the development of several variants, with some classified as variants of concern (VOCs) due to their increased transmissibility, and reduced response to antibody treatments and vaccines compared to the wildtype virus. Some variants, such as Alpha, Beta, Gamma, Delta, Omicron amongst

others generally exhibit multiple mutations at the S protein, which may affect their affinity towards the human cell receptor.²²⁻²⁴

SARS-CoV-2 is a rapidly spreading and mutating virus affecting millions of persons worldwide. Hence, to reduce the significant impact of the virus, there is need for the development of rapid, efficient, sensitive, and selective viral detection strategies suitable for mass testing amid a pandemic.

1.4 Strategies for detection of SARS-CoV-2

In response to the demands on testing and need for reliable and rapid alternatives, various techniques have been developed that have contributed to the advancement of diagnostic methods for COVID-19. The current diagnostic methods primarily rely on direct detection of the SARS-CoV-2 genetic material or proteins through nucleic acid and antigen detection or indirect detection of the virus *via* analysis of virus culture, antibody based or imaging-based techniques (Table 1.1).²⁵⁻²⁸ Although virus culture and imaging techniques can be useful confirmatory tests for viral infection, their access is limited.^{25,29} One of the main disadvantages with virus culture is that its operation requires a biosafety level three containment, which is not widely accessible.²⁵ Additionally, diagnostic imaging-based methods like computerized tomography (CT) scans and electron microscopy (EM) can be used for confirmation of false-negative results. However, they lack specificity, are generally expensive and are only performed on hospitalized patients which limits its availability and opportunities for carrying out mass testing.³⁰ Hence, biomarkers such as nucleic acids, antibodies and antigens are more prominently studied and applied in viral detection strategies.

Table 1.1. Current diagnostic strategies used for determination of COVID-19

	Diagnostic Methods	Analysis	Sensitivity	Specificity	Advantages	Disadvantages
Virus Culture	-	Live virus <i>(direct)</i>	N/A	N/A	<ul style="list-style-type: none"> · Measure the spread of the infection and detection of viral mutation · Determines active infection 	<ul style="list-style-type: none"> · Require biosafety level 1 safety lab environment · Not often used or suitable for diagnostic purposes
Imaging based detection	CT Scan, EM	Images of chest or Coronavirus-specific morphology <i>(indirect)</i>	90 – 97%	21 – 37%	<ul style="list-style-type: none"> · Rapid analysis · Capable of early detection · Able to monitor patient progress · Localization of viral infection of tissues/cells 	<ul style="list-style-type: none"> · Requires expensive, technical equipment and trained personnel for operation · Costly · Low specificity · Limited to hospital analysis (not ideal for mass testing) · Ineffective for asymptomatic individuals
Nucleic acid based detection	RT-PCR, NGS, CRISPR, RT-LAMP, EC	E, N, S or Orf1ab genes <i>(direct)</i>	68 – 97%	97 – 99%	<ul style="list-style-type: none"> · Standardized methods - considered the gold standard for viral detection · High specificity · Determines active infection 	<ul style="list-style-type: none"> · Requires expensive, technical equipment and trained personnel for operation (<i>except RT-LAMP</i>) · Insufficient amount of genetic material leads to false-negative results · Time consuming

Antibody based detection	Immunoassays (e.g., ELISA, LFIA, CLIA), EC	IgG or IgM (<i>indirect</i>)	67 – 87%	67 – 97%	<ul style="list-style-type: none"> · Rapid and cost-effective · Determines active infection - available as POCT · No need for specialized equipment – can be used for at-home testing 	<ul style="list-style-type: none"> · Detection of antibodies several days after infection · Levels of antibody produces can vary amongst age, gender, and health status · Potential for cross-reactivity with related coronaviruses.
Antigen based detection	Immunoassays (e.g., ELISA, EC), Immunochromatography (e.g., LFC, FIC), Aptasensors (e.g., EC, optical, piezoelectric etc.)	S (S1 and RBD), or N antigens (<i>direct</i>)	70 – 86%	95 – 97%	<ul style="list-style-type: none"> · Rapid and cost-effective · Capable of early detection · Determines active infection - available as POCT · User-friendly · No need for specialized equipment · No pre-treatment required · No need for specialized equipment – can be used for at-home testing · High sensitivity and specificity 	<ul style="list-style-type: none"> · Inability to determine past infection · Negative tests need to be confirmed by a confirmatory test

* CT (computerized tomography); EM (electron microscopy); RT-PCR (reverse transcriptase-polymerase chain reaction); NGS (next generation sequencing); CRISPR (clustered regularly interspaced short palindromic repeats); RT-LAMP (reverse-transcription Loop-mediated isothermal amplification); ELISA (enzyme-linked immunosorbent assay); LFIA (lateral flow immunoassay); CLIA (chemiluminescence immunoassay); EC (Electrochemistry); LFC (lateral flow chromatography); FIC (fluorescence immunochromatographic)

1.4.1 Nucleic acid detection

The early determination of the nucleic acid sequence for the SARS-CoV-2 has played a vital role in the design and development of probes and primers now being used for SARS-CoV-2 detection.^{28,31} With the need for confirmatory diagnostic methods for COVID-19, nucleic acid-based techniques have been developed over the past two years which target the N, E or RNA-dependent RNA polymerase (RdRp) genes.^{25,28,32,33} Amongst these methods is the gold standard polymerase chain reaction (PCR)-based technology, routinely used for testing respiratory-related viral infections.^{2,34-36}

Reverse-transcriptase PCR (RT-PCR) is widely accepted for viral detection and was therefore predominantly used as a confirmatory method for COVID-19 diagnosis during the pandemic. However, these methods are generally costly, labor-intensive, time consuming, and have relatively slow response time (hours to days).^{25,28} Furthermore, the increased demands of testing during the pandemic as well as the decreased availability of essential reagents and equipment to handle the high day-to-day testing demands resulted in delayed response times, overworked and limited trained personnel. The lack of immediate and accurate acquisition of diagnostic results can affect the efforts toward limiting the spread of the virus as patients await their results. Hence, it is important that techniques offering more rapid response times be developed and implemented to help reduce the impact of the disease. Also, of concern regarding PCR based tests is the sensitivity, precision, and accuracy which may be affected by factors such as the type of sample matrix, the correctness of the sample collection process performed and transfer to the testing laboratory. For example, the sensitivity of the RT-PCR method used varies for

respiratory samples such as bronchoalveolar lavage (BAL) fluid (93%), sputum (72%), nasal swabs (63%), or throat swabs (32%).^{31,36} This variability limits the type of samples that can be tested with RT-PCR techniques and can therefore become a challenge for mass testing. Additionally, the proper collection of the sample is crucial toward the analytical process as collection of insufficient amounts of genetic material from a suspected COVID-19 carrier can lead to inaccurate results with PCR based assays, which accounts for the high false-negative rates (2-30%) reported for SARS-CoV-2 testing.¹⁴

Apart from PCR based tests, next generation sequencing (NGS) and reverse-transcription Loop-mediated isothermal amplification (RT-LAMP) are other types of nucleic acid-based test.^{25,28} NGS was imperative in the initial determination of the novel SARS-CoV-2 genome sequence and can also be used for identification of viral variants, assessing immune responses, amongst other applications.^{25,37} Similar to PCR based methods, NGS requires expensive equipment and highly trained personnel with knowledge of the technical operational procedures, which makes it less attractive as a day-to-day viral detection tool. Alternatively, colorimetric tests, based on RT-LAMP methods have also been developed and used for SARS-CoV-2 detection.^{38,39} These were fabricated specifically as a rapid technique for determination of SARS-CoV-2 RNA. These tests are reportedly easy-to-use, cost-effective methods suitable as point-of-care tests (POCT).

Overall, PCR based techniques are proven to be great confirmatory tests for viral infections based on their standardized protocols, high specificity, and the ability for modification of the technique to further enhance its performance. However, PCR methods generally require expensive reagents and equipment for use only by highly trained

personnel, involves more complicated processes and does not address the limitations of rapid acquisition necessary for mass testing during the pandemic.²⁵ Thus, alternative methods that can provide rapid, sensitive, and highly specific detection are needed to meet the needs of mass testing during a pandemic.

1.4.2 Antibody detection

Serological tests, based on antigen-antibody interactions have long been used for determining viral infection. Antibody-based serological tests are typically developed in immunoassays such as enzyme-linked immunosorbent assays (ELISA), lateral flow immunoassays (LFIAs) and chemiluminescent immunoassays (CLIAs), which rely on the presence of viral antibodies in the patient sample for a positive result.^{15,25,40-43} Recently, antibody detection using electrochemistry and optical methods have also been explored.⁴⁴⁻⁴⁶ COVID-19 serological tests based on these methods have focused on anti-SARS-CoV-2 neutralizing antibodies IgA, IgG or IgM.^{25,44,47,48} Remarkably, they have quickly become commercialized as diagnostic kits, specifically for use as rapid response alternatives to RT-PCR methods. Serological tests are known for their high specificity and present benefits as easy-to-use, less expensive and labor-intensive alternatives, and are ideal as POCT, making them useful for at home testing kits.^{30,49,50} However, their applications are limited to only determining previous exposure to the virus and not active infection.^{25,49} Thus, serological tests are not suitable for monitoring the progress of a viral infection or for early prognosis of a disease because antibodies are generally only detected after 7-21 days post infection (Figure 1.2).⁴⁹

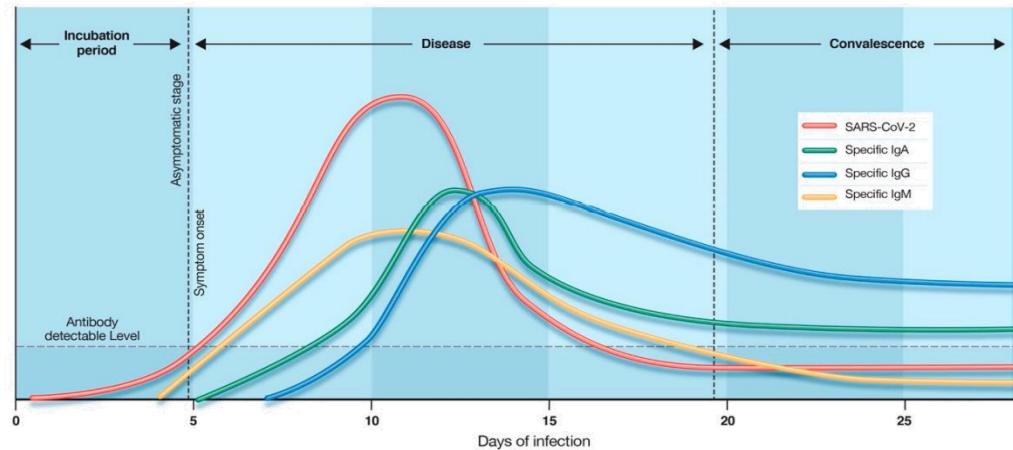


Figure 1.2. Timeline for detection of SARS-CoV-2 antibodies as a function of infection period; Figure reproduced from Ghaffari et al., (2020).⁴⁹

The reliability of serological tests may also depend on the type of antibody being targeted and the stage of the disease. As demonstrated in Figure 1.2, on average, IgA and IgG antibodies reach detectable levels only after about ten days following the onset of symptoms. IgM can be detected around five days after symptom onset. However, compared to other antibodies, it shows lower levels in infected patients and their antibody detection levels deplete much faster with progression of the disease. Thus, early diagnosis is not possible by antibody detection methods and sampling outside of the window correlated with high antibody detection levels (>10 days after infection) can result in false-negative results.⁴⁹ Overall, this serves as a disadvantage to health professionals due to the high testing demands throughout the current COVID-19 pandemic.

The serological antibody detection methods present as a rapid alternative to other conventional methods, which is vital for mass testing during the pandemic and improving turn-around times for results. However, these methods suffer from low sensitivity and lack

of reliability, contributing to high false -positive and -negative rates. Additionally, since these methods rely on the detection of SARS-CoV-2 antibodies, challenges due to cross reactivity with other coronaviruses are likely.

1.4.3 Antigen detection

Antigen-based detection also provides great promise as a rapid and cost-effective detection strategy. Fundamentally, these systems are based on the direct detection of viral related proteins which serve as biomarkers for viral infection. These tests offer the advantages of early detection and diagnosis, and rapid response, which cannot be achieved by conventional testing methods such as nucleic acid or antibody targeted techniques.

Several antigen testing methods and devices, typically targeting the SARS-CoV-2 S and N proteins have recently been developed for COVID-19.^{11,51-55} The SARS (2003) and MERS (2012) outbreaks revealed the value of structural proteins as indicators for coronavirus related diseases. Specifically, high sensitivity has been associated with the SARS-CoV N protein (90%) as the target, opposed to using antibody (21%) or viral nucleic acid (43%) approaches.^{11,56} The excellent performance is also identified in antigen-based assays for the novel SARS-CoV-2 demonstrating high sensitivity and specificity compared to other approaches. Additionally, unlike antibody-based tests, there is potential for early diagnosis of coronavirus related illness since there is no incubation time needed to determine the presence of the viral proteins.²⁵ Furthermore, the consistency of viral proteins throughout the time of infection allows for direct monitoring of patient progress based on the protein detection levels. This approach, using coronavirus surface proteins as

markers for viral infection can therefore be applied to the detection of SARS-CoV-2 or other viral protein targets.

1.5 Biosensors for SARS-CoV-2 antigen detection

Biosensors are analytical devices used for the identification of target analytes and typically includes four main components including the analyte (section 1.4), the bioreceptor, the transducer and signal output (Figure 1.3).^{57,58} Use of biosensors is generally more advantageous than the laboratory-based methods due to their possibility for portability/miniaturization, low cost, and less complicated sample preparation and operational procedures.^{30,57,59} Additionally, while the analyte detection can be monitored through interactions occurring between the analyte and the bioreceptor, biosensors may also provide quantitative results. These features make biosensors ideal for POCT, in-patient monitoring of treatments and a great rapid alternative to the traditional and more complex laboratory tests.

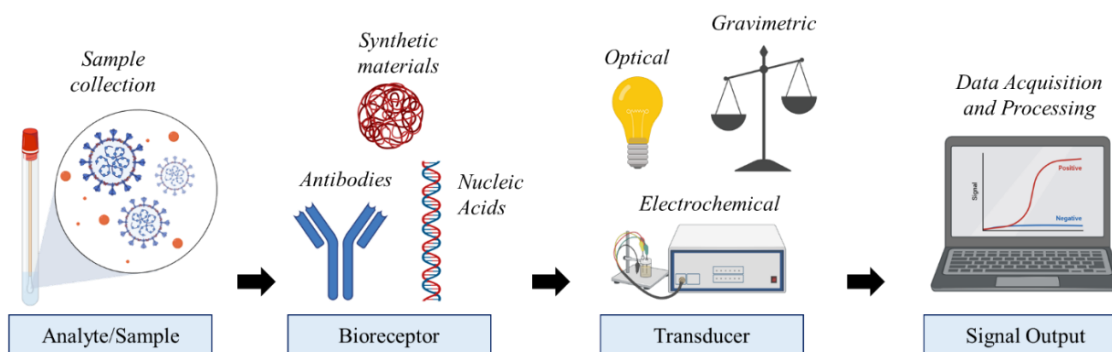


Figure 1.3. Illustration of common components of a biosensor. Created using biorendor.com.

Many biosensors based on SARS-CoV-2 nucleic acid and antibody detection have been explored.^{42,44,55,60-64} However, the rapid, cost-effective, and higher performing nature of antigen detection previously discussed have made antigen-based techniques attractive for application in biosensing platforms. Particularly for antigen detection, bioreceptors such as synthetic materials, antibodies and nucleic acids can be used with electrochemical, gravimetric, thermal, or optical platforms.⁵⁸

1.5.1 Bioreceptors used for detection of SARS-CoV-2 antigens

Common bioreceptors used for antigen detection are proteins, peptides, antibodies, or aptamers, which offer high affinity and specificity to their desired targets. Alternatively, synthetic materials such as molecular imprinted polymers (MIPs), metal organic frameworks (MOFs), quantum dots or graphene oxide may be used to avoid challenges related to bioreceptor applications, such as reduced shelf-life and increased cost of production.⁶⁵⁻⁷³ However, in biosensing applications, the use of synthetic materials can be affected by their low selectivity, challenges with regeneration, biosensor surface modifications, and the toxicity depending on the components used in its fabrication.⁶⁵ Hence, protein, antibody and aptamer bioreceptors specifically designed as binding partners for the SARS-CoV-2 antigens are more prominently used.

Traditionally, antibodies have been used as highly specific binding partners for whole cells or viruses, nucleic acids, and proteins. Several antibody functionalized biosensors have been developed and applied toward rapid detection of SARS-CoV-2 proteins. In fact, the rapid antigen tests used for at-home testing kits distributed during the pandemic are based on this mechanism. These assays are reliable and exhibit great


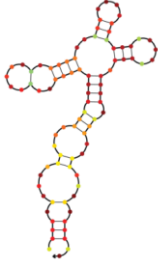
sensitivity and specificity. For example, commercially available rapid antigen tests such as the Panbio™ COVID-19 Ag Rapid Test, the BinaxNOW™ COVID-19 Ag CARD or the Roche's SARS-CoV-2 Rapid Antigen Test have exhibited sensitivity >95% and specificity >99% when tested on COVID-19 positive subjects confirmed by RT-PCR.⁷⁴ However, similar to challenges where antibodies can be used as target analytes, antibody receptors can suffer from cross-reactivity with other related viruses, which eliminates the possibility of determining the origin of the positive result and likely produce false-positive results.^{25,58} Additionally, they have a high batch-to-batch variation which limits their reproducibility and uses in biosensor devices.

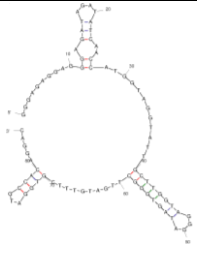

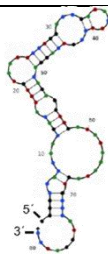
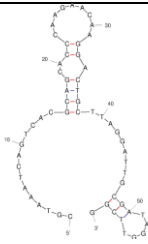
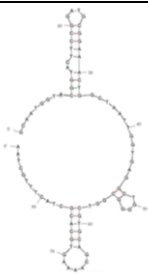
Proteins and peptides are also useful bioreceptors for some antigen detection mechanisms. For SARS-CoV-2 determination, the human cell receptor, ACE2, has become a common bioreceptor for S, S1 or RBD antigens. By probing the protein-protein binding events or peptide interactions, with the coronavirus' S protein, highly selective and specific detection of the coronavirus can be achieved.^{24,75-79} Additionally, some anti-S or anti-ACE2 peptide sequences have also been identified and used for exploiting S protein binding and disrupting the interaction between ACE2-S complexes.^{80,81} Thus, peptides can serve a dual purpose as bioreceptors and antiviral agents for therapeutic remedies.

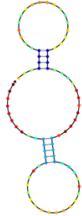
Aptamers are promising alternatives to antibodies that share the advantage of having high specificity to their targets. Common targets for aptamers include whole cells or viruses, bacteria, peptides, nucleic acids, small inorganic and organic molecules, amino acids, nucleotides, or proteins.^{82,83} Compared to the conventional antibodies, these single-stranded nucleic acid (RNA or DNA) molecules present high binding affinity (usually 0.1

to 50 nM) and specificity to their targets, are smaller in size, more thermally stable, less expensive and can easily be modified.^{82,84} Unlike antibodies, aptamers can also be stored at room temperature, with an unlimited shelf life, and remain stable in different environmental conditions.⁸³ Considering these properties and their excellent bio-affinity exhibited, aptamers are suitable bioreceptors for biosensing applications. Through SELEX (systematic evolution of ligands through exponential enrichment) -based methods, several aptamer sequences have been identified that target the SARS-CoV-2 specific proteins S or N and subunits, RBD or S1 (Table 1.2). Nonetheless, no aptamer-based technologies have entered the market yet.

Table 1.2. Examples of aptamers designed for detection of SARS-CoV-2 proteins.

Aptamer	Aptamer Name	Target Protein	K_D (nM)	Reference
	MSA1	Trimeric S (wild type and B.1.1.7)	1.8	[85]
	SNAP1	S1 (N terminal domain)	39	[86]

	SP5	S	9.2	[87]
	CoV2-RBD-1C	RBD	5.8	[88]
	RBD-PB6	RBD	18	[23]
	cb-CoV2-6C3	RBD	0.13	[89]
	N Aptamer 1	N	N/A	[11]

	nCoV-S1-Apt3	RBD	0.12	[90]
---	--------------	-----	------	------

Owing to their high affinity and sensitivity, aptamers are promising bioreceptors for application in biosensing technology. However, as the virus continues to evolve and mutate, the variations in binding sites at the target can present a challenge for biosensors. To address this shortcoming, universal aptamers that are insensitive to key mutations, particularly on the S protein, have been developed and applied.^{91,92} For instance, Zhang et al., (2022) developed a universal aptamer named MSA52 (reassembled from the MSA1 aptamer) as a binder to the trimeric S protein of the SARS-CoV-2 wildtype, as well as variants of concern, Alpha (B.1.17), Beta (B.1.351), Gamma (P.1), Epsilon (B.1.429), Delta (B.1.617.1), Kappa (B.1.617.2) and Omicron (B.1.1.529) with K_D values ranging from 3 – 10 nM.⁹¹

In addition to their application as bioreceptors, like peptides, aptamers may also be used for therapeutic purposes.^{89,93,94} One of the main pathways in which aptamers may serve as antiviral agents is through virus neutralization whereby the aptamer binds to the target S protein, thus blocking ACE2 binding sites and preventing infection. For example, the circular bivalent CoV2-6C3 was the first published evidence of aptamer inhibition of the SARS-CoV-2 S-ACE2 complex.⁸⁹ Using this aptamer, the binding affinity between the RBD and ACE2 was 0.13 nM with an 87.01% inhibition efficiency achieved and a half inhibitory concentration (IC_{50}) of 0.42 nM, when the potency of the aptamer was tested

with the SARS-CoV-2 virus. Other aptamers such as the nCoV-S1-Apt1 ($IC_{50} = 80.12 \text{ nM}$) and SP6 (IC_{50} not reported), and SNAP ($IC_{50} = 142.80 \text{ fM}$) have also shown effective inhibitory activity against the S1, S and RBD proteins, respectively.^{87,90,95}

The design of a variety of aptamers for different SARS-CoV-2 antigens, the extension of these aptamers to identify multiple targets with high affinity and the demonstrations of their potential in therapeutics, establishes the versatility of these biomolecules and their advantages as bioreceptors for their application in biosensing techniques.

1.5.2 Biosensor transducer platforms for SARS-CoV-2 antigen

detection

Biosensor transducers are used to measure the interactions occurring between the sample analyte and the bioreceptor used. Compared to typical laboratory-based tests, biosensors can be packaged as a simple-to-use POC device for detecting and monitoring viral infections. Furthermore, the pairing of biosensor transducers with excellent performing bioreceptors can significantly improve the sensitivity of the detection method. A variety of systems including electrochemical or optical sensors with a diverse array of bioreceptors have been used in antigen-based detection designs.

Electrochemical-based biosensors have become a popular sensing platform due to their portability, ease of use, rapid response, and good sensitivity. They convert the chemical activity of an analyte into a readable electrical signal for both qualitative and quantitative analysis. With the high demand for well performing viral detection strategies

amidst the pandemic, several electrochemical antigen detection biosensors have been developed (Figure 1.4A-B). The electrochemical platforms explored are based on potentiometric, amperometric and impedimetric sensing using functionalized carbon nanotube surfaces, plasmon-enhanced photoactive materials, graphene, carbon surfaces amongst others.^{54,66,70,96-104} Curti et al., (2022) developed an indirect DNA aptamer based amperometric screening system for the SARS-CoV-2 S1 protein. Fundamentally, the interaction mechanism of the analyte and bioreceptor relies on rearrangement of the S1 aptamer (CoV2-63) in the presence of the S1 protein (Figure 1.4A). Prior to the introduction of the S1 protein, the aptamer is in a folded configuration, where the methylene blue (MB) tag is positioned in close proximity to the electrode surface. On the other hand, when the protein is introduced and binds to its bioreceptor, the distance between the MB increases, leading to a decrease in the electron transfer process, which is translated as a decrease in the current measured (Figure 1.4A). The sensor exhibited a limit of detection (LOD) of 7 nM, which is outside of the clinically relevant range (~250 fM) for SARS-CoV-2, but displayed low cross-reactivity when tested with other potentially interfering species such as MERS-CoV or Influenza A.^{53,98} In another approach, the SNAP1 aptamer was used on a electrode modified with copper hydroxide nanorods for a high performing, label-free S protein electrochemical aptasensor.⁹⁹ When tested in real samples of saliva and other medium, the sensor maintained its performance with >97% recovery. The performance of this aptasensor and other electrochemical protein- or antibody-based sensors are also comparable to the conventional PCR or ELISA based tests, which demonstrates the reliability as alternative detection strategies.^{10,62,77,99,104,105}

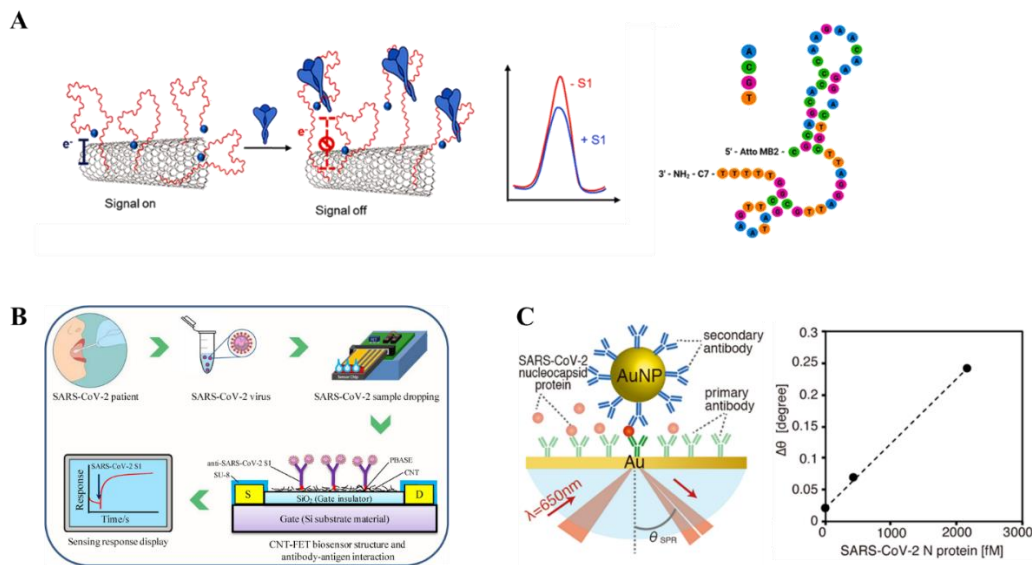


Figure 1.4. (A) Electrochemical aptasensor based on the conformational change of a methylene blue redox tagged aptamer for detection of the SARS-CoV-2 S1 protein; Figure reproduced from Curti et al., (2022).⁹⁸ (B) Illustration of concept of sampling procedure for application of a CNT-FET antibody based biosensor for detection of SARS-CoV-2 S1 antigen; Figure reproduced from Zamzami et al., (2022).⁹⁶ (C) Scheme of SPR set up for the detection of SARS-CoV-2 N protein using antibody functionalized AuNP surface with a secondary AuNP/antibody conjugate and the linear range SPR signal as a function of N protein concentration; Figure reproduced from Yano et al., (2022).¹⁰⁶

Field effect transistor (FET)-based biosensors also depend on electrochemical signaling with the added advantage of real-time monitoring of the current response. Recently, Zamzami et al., (2022) developed a single wall carbon nanotube (SWCNT) FET biosensor for the direct detection of the SARS-CoV-2 S1 protein (Figure 1.4B). The sensor was fabricated using source and drain (S-D) electrodes with CNT ink pattern printed over Si/SiO₂ materials between the active areas of the S-D electrodes. For detection of the S1

protein, the complementary monoclonal SARS-CoV-2 S1 antibodies were used as the bioreceptor, achieving a LOD of 4.12 fg/mL and a wide dynamic range. The authors also demonstrated that the FET sensor was capable of selective SARS-CoV-2 detection. Moreover, despite their similarities in genomic makeup to the target, the immunosensor displayed no cross-reactivity with related viruses, SARS-CoV and MERS-CoV S1 antigen. Several of the FET based sensors recently explored, including nucleic acid and antibody-based sensors, have demonstrated quick response times (<10 min) and the ability to detect small concentrations of the target, which reflect the features of a model biosensor.^{61,96,97} Electrochemical based biosensors offer attractive benefits such as portability, low cost, and rapid response. However, many are limited in their sensitivity, reproducibility, and ultimate upscaling opportunities, which are essential for mass testing during a pandemic.^{58,84}

The basic principle of optical transducers relies on a physical measurement of light passing through a system, which is converted to an electronic signal for qualitative and quantitative analysis. Optical based biosensors are generally easy-to-use, thus not requiring extensively trained personnel for its operation or expensive equipment. Recently developed SARS-CoV-2 detection techniques based on optical sensing include fluorescence, surface-enhanced Raman scattering (SERS), colorimetry and surface plasmon resonance (SPR)-based methods.^{38,60,102,107–112}

SPR is a label-free plasmonic technique that monitors changes to the refractive index at a thin metallic surface (Figure 1.5A).¹¹³ In principle, the light energy applied excites electrons at the surface causing electron movement (“plasmons”) near the surface, generating a plasmon field ~250 – 1000 nm. The SPR angle at which the resonance occurs

is measured and produces the SPR signal dependent on the refractive index of the surface.¹¹⁴⁻¹¹⁷ The signal output is directly related to the response of biomolecular interactions such as antigen-antigen, antigen-nucleic acid, antibody-antigen, amongst others. Yano et al., (2022) developed a SPR biosensor for detection of the N protein that is capable of femtomolar levels of detection (Figure 1.4C). This was achieved by using a sandwich-type assay with primary N antibody and secondary antibody conjugated with large AuNPs of diameters 150 nm, which enhanced the sensitivity of the technique.¹⁰⁶ Overall, the performance of SPR biosensor (LOD = 4 pg/mL) was within the clinical range and comparable to a conventional RT-PCR method (4.5 pg/mL), which indicates its potential as a reliable diagnostic tool. Notably, SPR techniques are generally useful for the evaluation of receptor-analyte interactions and offer many benefits as an alternative method to current SARS-CoV-2 detection methods. SPR has the potential for automation, requirements of only a few biological reagents necessary for testing, and small amount of sample needed. It also offers real-time monitoring between binding partners without labeling requirements, which is beneficial for the development of POC devices essential for advancing approaches toward patient care and treatment.

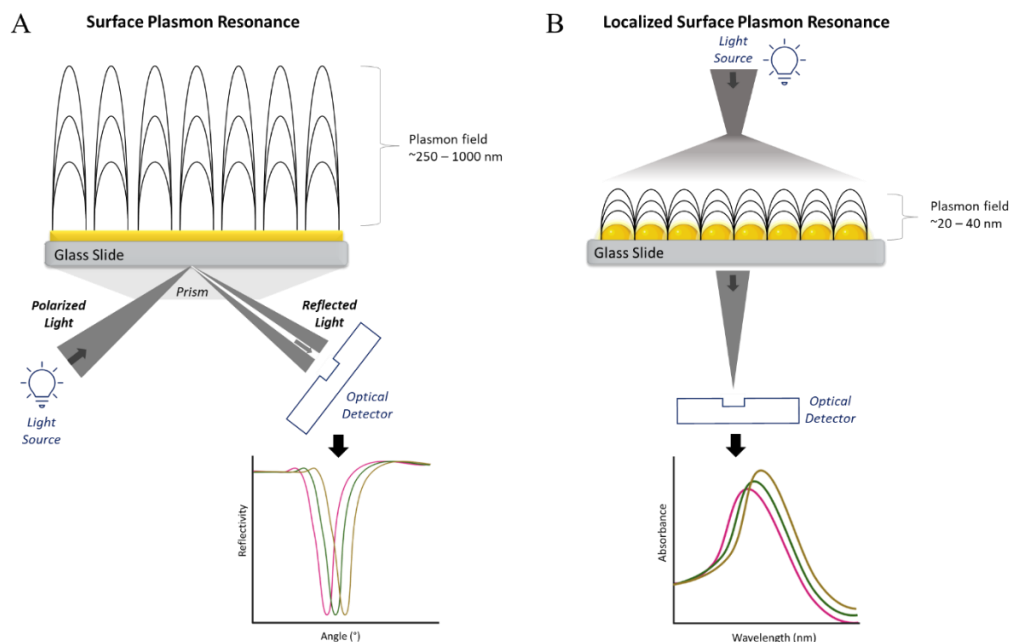


Figure 1.5. General concept of (A) SPR *versus* (B) LSPR operational principle. Created using biorendor.com.

In contrast to traditional SPR techniques, the localized surface plasmon resonance (LSPR) method uses a nano-structured surface that can detect small changes in binding events and reports the photophysical characteristics based on the binding activity at the sensor surface (Figure 1.5B).^{115,116,118–120} In this case, a prism is not used. The signal output is dependent on changes in the wavelength of the resonance absorbance peak which are closely related to the local refractive index. The plasmonic field for LSPR (20 – 40 nm) is more localized compared to what is measured for SPR, which in turn corresponds to LSPR being more sensitive to molecular binding events at the surface.¹¹⁴ The analysis of interactions performed using SPR and LSPR biosensors involves four main stages, including the association phase, steady state, dissociation phase and regeneration (Figure 1.6). Once the ligand is attached to the sensor surface, the target molecules that are

dissolved in a solution, are allowed to flow over the functionalized surface to probe the ligand-analyte complex formation. The interactions of the biomolecules as they pass through the flow channel can then be monitored by SPR or LSPR.

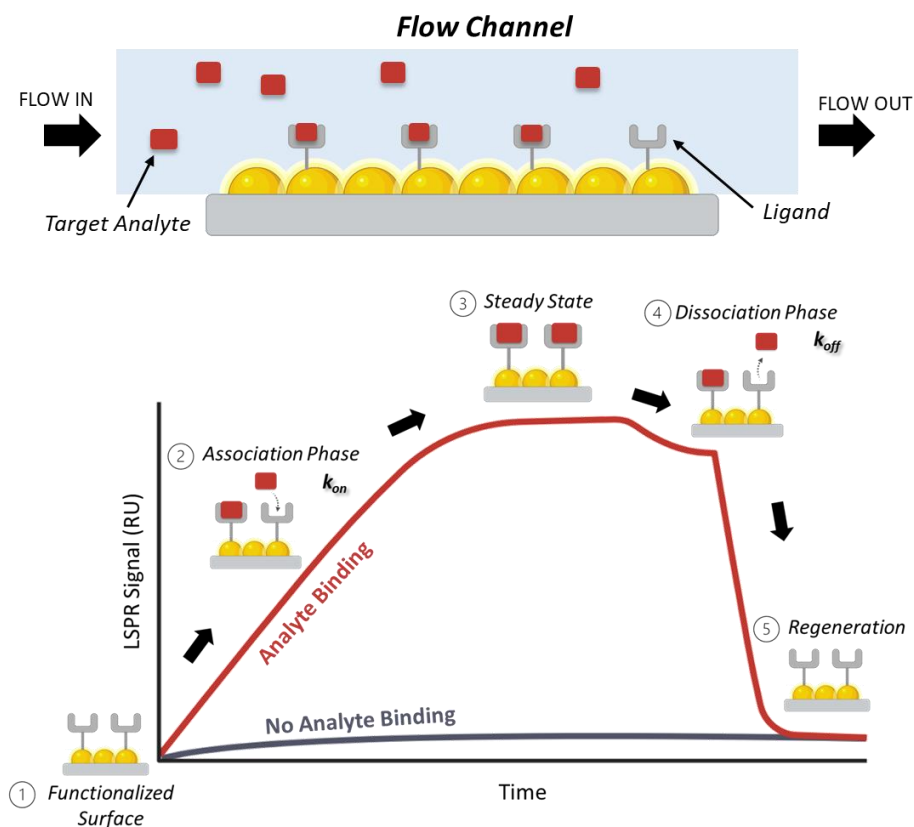


Figure 1.6. Illustration of the flow through mechanism and typical sensorgram generated for LSPR measurement. Created using biorendor.com.

The changes to the LSPR signal and trends in sensorgram profiles can provide quantitative and qualitative information about the ligand-analyte interactions occurring at the surface. Analyte binding to the ligand induces a change in the refractive index or resonance absorbance, which is translated as a signal increase measured as resonance units or response units (RU). The amount of analyte binding is directly related to the signal

generated. As demonstrated in Figure 1.6, this period of ligand-analyte binding is referred to as the “association phase” and the rate at which this binding occurs can be measured (k_{on}). When all sites are completely saturated with the analyte, the “steady state” is observed, where no significant change to the signal is recorded. Following this, the “dissociation phase” describes the period in which there is release of analyte from the ligand, owing to low or weak binding. This process can be slower or quicker, depending on the affinity of the ligand-analyte complex. The rate at which the analyte is removed from the ligand (k_{off}) is related to the dissociation events during this period. Finally, complete chemical regeneration of the sensor surface can be done and is beneficial to allow for repeat reuse of the sensor surface over multiple measurements. The reusability of the surface is an attractive asset as this directly lowers costs per test. Based on these processes, which can be observed in real-time, SPR methods can be useful for evaluating kinetic and affinity (K_D) parameters of biomolecular interactions. This contrasts with other biosensor applications like electrochemistry which do not offer these advantages for biomolecular processes.

1.6 Proposed research strategy and objectives

To address the need for alternative, user-friendly, and rapid testing methods for SARS-CoV-2 detection, we propose the use of LSPR for the development of a SARS-CoV-2 antigen detection test. The proposed technique is based on single-stranded DNA (ssDNA) aptamer recognition of SARS-CoV-2 structural protein, which enhanced the specificity and selectivity of the biosensor. Use of the platform is ideal for POCT allowing for user-friendly, rapid, real-time, quantitative measurement of SARS-CoV-2, with the potential for

early diagnosis— all of which cannot be achieved using a single traditional method. Development of this biosensor will improve the response times for test results furthermore reducing the burden on health professionals to meet the high demand of testing during the current pandemic and future ones.

Within this research, testing surfaces used are based on covalent and capture/affinity coupling (Figure 1.7). For the fabrication of a biosensor reliant on surface-based interactions, the surface chemistry may affect the detection limit and sensitivity of the biosensor. Hence, it is important to apply and compare various surface chemistries of the biosensor to determine the most optimal configuration. Commercially available surfaces such as carboxyl, nitrilotriacetic acid, streptavidin, and gold are commonly used for assessing the interaction of various biomolecules.

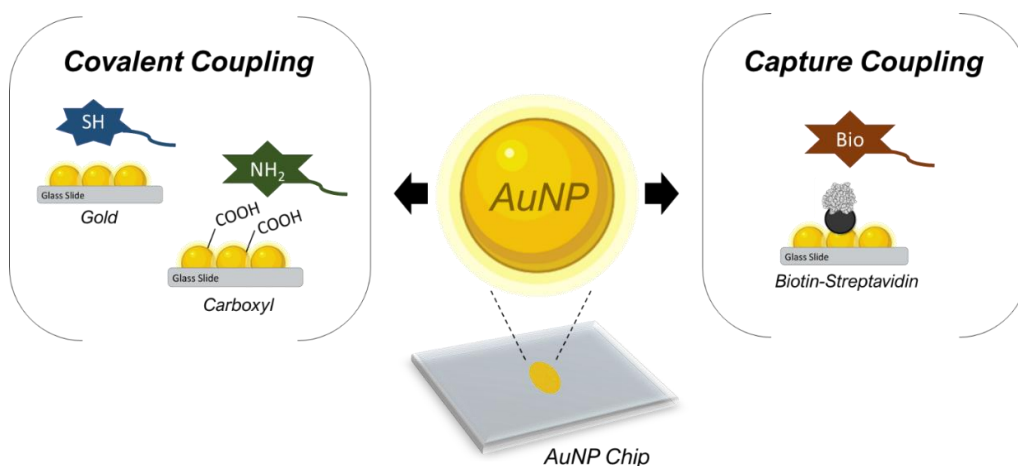


Figure 1.7. Various covalent and capture coupling strategies that are being explored along with the ideal immobilization targets using differently modified AuNP sensor surfaces. Created using biorendor.com.

The comparison of these sensor surfaces allowed us to evaluate and compare the sensitivity and selectivity of the biosensors for the respective antigen target. A variety of sensor chip/surfaces are commercially available for LSPR and the appropriate chip to be used for an assay is determined based on the surface chemistry intended for the sensor, including the characteristics of the bioreceptor being used. For this project, surfaces explored included biotin-streptavidin sensors (for biotinylated labeled targets), gold sensors (for thiol labeled targets) and carboxyl sensors (for amine labeled targets).

The goals of this project were addressed through three main objectives including: (1) development of an LSPR streptavidin-biotin sensor chip, (2) evaluating the role of sensor surface functionalization on sensitivity and selectivity of the assay and (3) application of the aptamer sensor as a ready-made sensor kit. Within Chapter 2 of this thesis, objectives 1 and 3 are addressed using the best performing sensor, the aptamer functionalized streptavidin-biotin sensor. The performance of the gold and carboxyl sensor surfaces with protein-aptamer interactions are further evaluated within Chapter 3 of the thesis. Lastly, protein-protein interactions are discussed in Chapter 4, which can further be applied in studies of interference involving aptamers as antiviral agents.

Chapter 2:

Localized surface plasmon resonance aptasensor for selective detection of SARS- CoV-2 S1 protein

2.1 Introduction

The severe acute respiratory syndrome coronavirus 2 (SARS-CoV-2) resulted in a worldwide COVID-19 outbreak. The primary concerns related to this virus are early detection and diagnosis to mitigate spreading, and the development of antiviral therapies. Detecting unique viral ribonucleic acid (RNA) sequences of SARS-CoV-2 requires nucleic acid amplification tests through real-time reverse-transcription polymerase chain reaction (rRT-PCR). While PCR-based techniques are highly sensitive, these procedures are complex and time-consuming, require extensive sample preparation and technical expertise, and may lead to false-negative and false-positive results. Alternative methods to traditional PCR testing have recently been developed, such as using combined plasmonic photothermal and localized surface plasmon resonance for sensitive detection of SARS-CoV-2 facilitated by nucleic acid hybridization.⁶⁰ Additionally, colorimetric assays based on antisense oligonucleotides and gold nanoparticles were designed for detection of SARS-CoV-2.^{121,122} The quantification of viral nucleic acids was also achieved using hybridization between target and capture strands and magnetic iron oxide nanoparticles.³²

Similarly, polymeric magnetic nanoparticles were used for efficient extraction of viral RNA to detect COVID-19 infection.¹²³

An alternative to nucleic acid testing, is the COVID-19-antibodies detection. Serological testing for SARS-CoV-2 requires the production of antibodies due to an infection. While antibodies may be detected in the later stage of a disease, antibodies persist in bodily fluids longer than viral RNA or antigens and allow for monitoring of both late-stage and past infections.³¹ Several serological-based sensors have been reported for SARS-CoV-2.^{41,43,50,109,124–127} Lateral flow immunoassays based on gold nanoparticles were used for detection of IgM and IgG antibodies of SARS-CoV-2 using test strips.^{41,43} The use of colorimetric tests for detection of antibodies was also achieved using vertical flow cellulose-based assay and an HRP/TMB detection system.¹²⁴

Testing for the SARS-CoV-2 antigens, represents a valuable diagnostic strategy. Several structural proteins such as the spike (S) glycoprotein (located at the viral surface) (Figure 2.1), and nucleocapsid (N) protein (located in the virus) are critical for viral function. The S1 subunit (Figure 2.1(B)) within the S protein interacts with the angiotensin-converting enzyme 2 (ACE2) expressed on the host cell. Hence, the S1 protein is a key target for the diagnosis, treatment, and vaccination of SARS-CoV-2. Antigen tests for SARS-CoV-2 S or N proteins have been achieved using enzyme-linked immunosorbent assay (ELISA). However, ELISA requires extensive labelling and use of multiple antibodies for viral detection or antigen detection. Recently, electrochemical methods have been used for detection of SARS-CoV-2 S protein using immunosensors.^{103,128} The SARS-CoV-2 antigen proteins were also detected using a real-time immunosensor based on the

field-effect transistor, lateral flow, microfluidic, electrochemical, nanoplasmonic, and paper-based sensors, all towards the development of the point-of-care diagnostics.^{55,61,129,130}

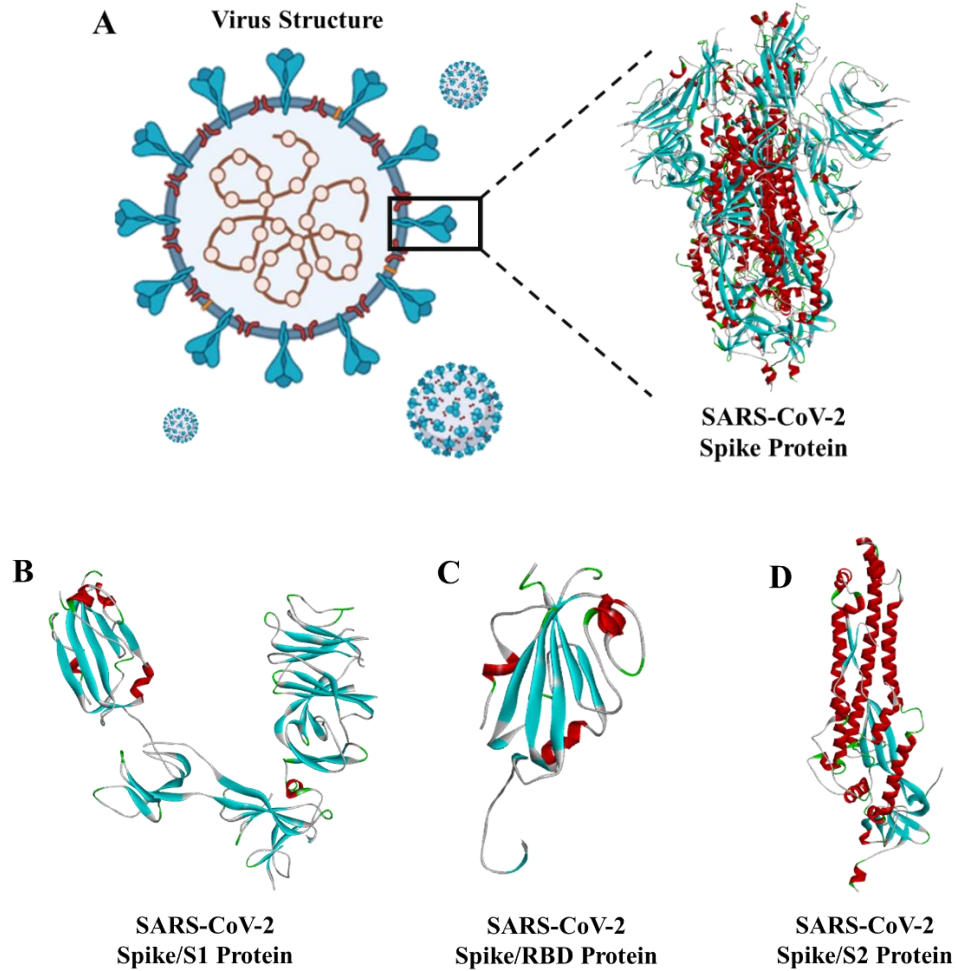


Figure 2.1. (A) Illustration of SARS-CoV-2 virus and structure of the full-length S protein. (B) Structure of the SARS-CoV-2 S1 protein, (C) RBD protein, (D) S2 protein; (PDB: 6VSB structure of protein subunits obtained using Discovery Studio Visualizer Software).

Aptamers are small nucleic acids with high stability and high affinity for their targets and offer a number of advantages over antibodies for sensor design. The aptamers

to SARS-CoV-2 proteins were not available prior to 2020, but given the recent COVID-19 pandemic, a handful of aptamers have been generated using the SELEX procedure, and their identity reported. For example, several single strand DNA aptamers were tested with the N protein using ELISA, towards development of antigen sensors for SARS-CoV-2.¹³¹ A silicon thin film transistor-based sensor was also developed using aptamers for the S1 protein of SARS-CoV-2 in the 1 pM–1 nM range.¹² In addition, aptamers to the receptor binding domain (RBD) of SARS-CoV-2 were selected by SELEX and exhibited high binding affinities as determined by flow cytometry.⁸⁸ The S protein was also detected through a plasmonic D-shaped plastic optical fiber aptasensors.¹⁰⁷ The off-the-shelf glucometer was also developed for detection of S protein using aptamer based beads.¹⁰

The use of “label-free” assaying strategies that require minimal reagent labeling, one step of incubation with the sample, and a subsequent fast signal read out in real time is of high value. The surface plasmon resonance (SPR) method has been extensively used as a method of choice for label-free detection of proteins, nucleic acids, and antibodies. Recently, SPR was used for detection of the SARS-CoV-2 N protein, for monitoring S protein binding to ACE2, and to monitor antibody-RBD binding.^{60,132} More recently, it has been demonstrated that the vastly different limit of detections for Spike protein can be obtained when using different aptamer-based optical methods such as biolayer interferometry, surface plasmon resonance and surface-enhanced Raman spectroscopy.⁵³ Compared to traditional SPR, localized surface plasmon resonance (LSPR) utilizes gold nanoparticles on the surface of SPR chip and is sensitive to refractive index changes and molecular binding.^{116,119,133} LSPR has been used for detection of viral nucleic acids from

SARS-CoV-2 through DNA–RNA hybridization.^{55,60} However, LSPR has not been explored using aptamers for detection of SARS-CoV-2 S protein or its domains.

To test the ability of aptamers to be used for selective and sensitive detection of SARS-CoV-2, we created an aptasensor based on a streptavidin–biotin interface for LSPR applications. We chose SARS-CoV-2 proteins as antigens for the target aptamer because proteins are the most abundant antigens at the early stage of infection. The LSPR platform, based on measuring changes in the LSPR absorbance peak, can provide a real-time response due to binding between aptamer and protein. The tunable nature of aptamers allows for the use of a tailored sensor against various proteins, allowing for differentiation of the S protein from the N protein. Ultimately, aptamer selection can also be optimized for selective detection of the S protein of SARS-CoV-2 compared to SARS-CoV, or other viruses in the Coronaviridae family. In the present study, we probed several aptamers as differential sensors for the S1 protein domain, compared to RBD or S2 protein domains. The LSPR method with a 2-channel system was used to allow for simultaneous testing of positive and negative controls. Using the optimized aptasensor for S1, we successfully demonstrated that the sensor was selective for this protein domain, in spiked buffer samples and spiked artificial saliva samples. Finally, we verified the function of the aptasensor for the S1 protein of SARS-CoV-2 versus SARS-CoV, confirming the utility of the aptasensor to produce distinctly higher signals for SARS-CoV-2 than SARS-CoV. Therefore, an LSPR aptasensor for S1 protein of SARS-CoV-2 has potential applications for diagnosis, treatment, and prevention of the diseases.

2.2 Material and methods

2.2.1 Chemicals and reagents

SARS-CoV-2 Spike/S1 (cat: 40591-V08B1), SARS-CoV-2 Spike/S2 (ECD) (cat: 40590-V08B), SARS-CoV Spike/S1 (cat: 40150-V08B1) His-tagged recombinant proteins, SARS-CoV-2 Spike/RBD protein (cat: 40592-VNAH) and SARS-CoV-2 N protein (cat: 40588-V08B) were purchased from Sino Biological (Beijing, China). Bovine serum albumin (BSA) acquired from Sigma Aldrich, sodium chloride (BioShop), sodium phosphate dibasic (Westlab), potassium chloride (EMD Chemicals), potassium phosphate monobasic (MP Biomedicals), magnesium chloride (Caledon Laboratories), Tween20 (Fisher Bioreagents) were used to prepare the binding/running buffer. Sodium dodecyl sulfate (SDS) was purchased from BioRad. Artificial saliva (Modified Fusayama/Meyer pH 6.5) was purchased from Pickering Laboratories. The biotin–streptavidin sensor kit containing biotin functionalized gold chips and streptavidin protein aliquots was obtained from Nicoya LifeSciences.¹³⁴ The 5'-biotinylated aptamers, S1 Aptamer (5'-Biotin-CAGCACCGACCTTGTGCTTTGGGAGTGCTGGTCCAAGGGCGTTAATGGACA-3'), S1 Aptamer-T (5'-Biotin-TTTTTTCAGCACCGACCTTGTGCTTTGGGAGTGCTGGTCCAAGGGCGTTAATGGACA-3'), N Aptamer-T (5'-Biotin-TTTTTTGCAATGGTACGGTACTTCCGGATGCGGAAACTGGCTAATTGGTGAGGCTGGGGCGGTCGTGCAGCAAAAGTGCACGCTACTTTGCTAA-3') were purchased from Integrated DNA Technologies.

2.2.2 LSPR measurements

Protein-aptamer interactions were investigated using a LSPR instrument (OpenSPR, Nicoya Lifesciences, Canada), equipped with a 2-channel detection and an automatic sample injection system. By using the OpenSPR instrument the absorbance versus wavelength was collected to determine the absorbance peak of the AuNPs on the sensor (biotin-Au chip) (548 nm), which is the LSPR peak of the sensor chip. The response graph provides the real-time tracking of the LSPR absorbance wavelength of the resonance peak position as a signal in resonance units (RU) units (y-axis) over time (x-axis). Once sample is injected then the data are collected as signal (RU) versus time (s). All experiments were performed at 20 °C. Prior to surface activation, the biotin functionalized gold (Au) nanoparticle sensor was cleaned by injection of 10 mM HCl at a flow rate of 150 $\mu\text{L min}^{-1}$. The biotin-gold sensor was then functionalized with 0.5 μM of streptavidin protein solution in buffer at a flow rate of 20 $\mu\text{L min}^{-1}$ for 5 min. This flow rate was selected to allow for the optimal binding to occur as previously reported. All experiments were completed using a binding/running buffer consisting of 136.8 mM NaCl, 10.1 mM Na_2HPO_4 , 2.7 mM KCl, 1.8 mM KH_2PO_4 , 0.55 mM MgCl_2 , 0.05% Tween20 (v/v), 0.1% BSA (w/v), pH 7.4.⁸⁸ The binding/running buffer was filtered with a 0.45 μm nylon syringe filter, non-sterile from Canadian Life Science (cat: SF6054-06N) and used for all dilutions, rinsing steps and dissociation phase. All measurements were performed in triplicate (N = 3) or multiples (N = 9), with mean and standard deviation reported. The data was analyzed using the TraceDrawer software to determine the association rate (k_a), dissociation rate (k_d) and dissociation constant (K_D). The 1:1 binding model was based on the eqn (1):

$$dY/dt = (k_a \times c - k_d) \times Y, \quad (1)$$

wherein, Y , the signal, c , the protein concentration of the bulk protein solution, k_a , the association rate constant (1/(M s)), and k_d , the dissociation rate constant (1/s). From the LSPR binding curves, the signal difference ($(I_f - I_i)$ in Δ RU units) was calculated as the difference between the final LSPR signal (at 800 s, I_f) and the initial signal prior to protein injection (at 100 s, I_i). The linear fit equation obtained from the standard curve and the signals from the measurements of the blank were used to estimate the limit of detection (LOD) and limit of quantification (LOQ); $y_{LOD} = \text{mean of the blank measurement} + 3 \times (\text{standard deviation of the blank})$; $y_{LOQ} = \text{mean of the blank measurement} + 10 \times (\text{standard deviation of the blank})$.¹³⁵ The blank solution was based on the binding/running buffer free of any SARS-CoV-2 protein.

2.2.3 Fabrication of LSPR aptasensor

100 μ M stock solutions of aptamers were prepared by dissolving the solid S1 aptamer (16 180.6 g mol⁻¹, 0.93 mg) in 577 μ L water, S1 aptamer-T (18 005.8 g mol⁻¹, 0.61 mg) in 340 μ L water, and N aptamer-T (29 586.3 g mol⁻¹, 0.5 mg) in 169 μ L water. For immobilization step, each aptamer was diluted in running buffer to a concentration of 50 μ g mL⁻¹ by addition of 6.2 μ L S1 aptamer to 193.8 μ L buffer, 5.6 μ L S1 aptamer-T to 194.4 μ L buffer and 3.4 μ L N aptamer-T to 196.6 μ L buffer. A single injection of each aptamer solution was then performed at a flow rate of 20 μ L min⁻¹.

2.2.4 S1 protein detection and quantification

Once the sensor surface was prepared with the selected aptamer, an injection of 150 μL of protein was performed and passed over the immobilized aptamer at a flow rate of 10 $\mu\text{L min}^{-1}$ for 10 min. A dissociation period followed each sample injection, with the running buffer passed over the sensor for at least 5 min. Prior to introduction of any sample, the injection port was rinsed with the binding buffer, and subsequently purged with $\sim 0.5\text{--}1$ mL air. For concentration-dependent analyses, the S1 protein was prepared by serial dilution to concentrations of 0.03, 0.1, 0.5, 1, 2, 4, 6, 8, 10, 12, 14, 16, 32, 66 and 131 nM (2.4 ng mL^{-1} to $10 \mu\text{g mL}^{-1}$) in the binding buffer. The binding buffer was also used as the blank solution with no analyte present. The sensor surface was regenerated with an injection of 0.5% SDS buffer at a flow rate of 150 $\mu\text{L min}^{-1}$ for 15 s. After completion of the regeneration step, and prior to subsequent injection of another sample, the running buffer was allowed to flow over the sensor again for 5 min, or until the baseline stabilized. The procedure used for this assay involved the following steps: baseline (1 min), association (10 min), dissociation (5 min), regeneration (15 s).

2.2.5 Selectivity studies

The S1 aptasensor and N aptasensor were tested with $2.5 \mu\text{g mL}^{-1}$ SARS-CoV-2 S1, S2, and RBD proteins, SARS-CoV S1 protein and BSA protein for 10 min interaction time each at a flow rate of 10 $\mu\text{L min}^{-1}$. A 0.25 mg mL^{-1} stock solution of each protein was prepared by addition of 400 μL of water to 0.1 mg of protein solid. 2 μL of each stock solution was added to 198 μL of binding buffer and mixed by vortex to prepare separate $2.5 \mu\text{g mL}^{-1}$ working solutions of SARS-CoV-2 and SARS-CoV proteins, unless otherwise

mentioned. A 1 mg mL^{-1} stock solution of the BSA protein in water was diluted to $2.5 \text{ }\mu\text{g mL}^{-1}$ by addition of $0.5 \text{ }\mu\text{L}$ of BSA to $199.5 \text{ }\mu\text{L}$ binding buffer for LSPR measurements. Various protein mixtures were prepared by combining specific proteins, such that each protein was at $2.5 \text{ }\mu\text{g mL}^{-1}$.

2.2.6 S1 protein detection in artificial saliva

For assessment of signal recovery with the S1 protein and S1 aptamer, samples of spiked, diluted artificial saliva were tested. A $100\times$ diluted saliva samples were prepared by adding $2 \text{ }\mu\text{L}$ of artificial saliva to $198 \text{ }\mu\text{L}$ of the binding buffer. Spiked solutions were prepared by mixing $2 \text{ }\mu\text{L}$ of the 0.25 mg mL^{-1} stock S1 protein solution with $198 \text{ }\mu\text{L}$ $100\times$ diluted saliva samples. $150 \text{ }\mu\text{L}$ of the prepared samples was injected for analysis with a flow rate of $10 \text{ }\mu\text{L min}^{-1}$ (10 min association phase) with the S1 aptamer. The percent recovery was calculated by dividing the LSPR signal of the spiked saliva sample with the signal of the spiked buffer and multiplying the ratio by 100.

2.2.7 S1 protein detection in serum albumin

For assessment of signal recovery with the S1 protein and S1 aptamer, samples of spiked, diluted serum albumin were tested. The bovine serum albumin (BSA) at 40 g L^{-1} was prepared, and subsequently diluted $1000\times$ ($40 \text{ }\mu\text{g mL}^{-1}$) in running buffer. The spiked serum albumin samples were prepared by mixing $2 \text{ }\mu\text{L}$ of the 0.25 mg mL^{-1} stock S1 protein solution with $198 \text{ }\mu\text{L}$ of the $1000\times$ diluted serum albumin. $150 \text{ }\mu\text{L}$ of the prepared sample was injected for analysis with a flow rate of $10 \text{ }\mu\text{L min}^{-1}$ (10 min association phase) with the S1 aptamer. The percent recovery was calculated by dividing the LSPR signal of

the spiked serum albumin sample with the signal of the spiked buffer and multiplying the ratio by 100.

2.2.8 Shelf-life stability of sensor chip

For offline sensor preparation (prepared outside of the instrument), the fresh chip was thoroughly rinsed with running buffer then air dried. The sensor surface was spotted with 50 μL of 10 mM HCl and incubated at RT for 1 min. The sensor was then thoroughly rinsed with buffer and air dried. The sensor surface was then spotted with 50 μL of 0.5 μM streptavidin solution and incubated at RT for 1 h. Following the incubation, the sensor was thoroughly rinsed with buffer then air dried. Finally, 50 μL of 50 $\mu\text{g mL}^{-1}$ biotinylated S1 aptamer was spotted onto the sensor surface, and sensor was incubated at RT for 1 h. The chip was thoroughly rinsed with buffer then air dried. Next, the offline prepared sensor, referred to as $t = 0$ day, was mounted into the OpenSPR instrument and used immediately for the measurements with SARS-CoV-2 S1 protein. Other offline chips were prepared in an identical manner and were stored in the running buffer for $t = 10$ days or 24 days, at 5 $^{\circ}\text{C}$, prior to being used for the measurements with SARS-CoV-2 S1 protein.

2.2.9 Repeatability and reusability of sensor

The online and offline prepared chips were tested for repeatability and reusability. The offline chip was prepared as described above shelf-life stability measurements. Briefly, various solutions were drop-casted onto the chip outside of the instrument, stepwise with intermittent rinsing. The offline chip which was functionalized with the S1 aptamer was then mounted into the instrument and used immediately. The online chip was mounted into

the instrument, and all the chip functionalization steps were carried out online prior to the measurements. For each chip tested, at least 9 repetitions of the SARS-CoV-2 S1 protein injections ($1 \mu\text{g mL}^{-1}$) were carried out, with regeneration steps in between. The buffer and BSA protein were used as controls.

2.2.10 Docking modeling of S1 protein and S1 aptamer

The S protein structure derived from Cryo-EM data was used for modeling (PDB: 6VSB).¹³² Mfold was used to generate 2D aptamer structure, and RNAComposer to generate 3D structure of aptamer–protein complex.^{136,137} The Patchdock was used to perform docking studies for aptamer–protein complex.^{138,139}

2.2.11 Scanning electron microscopy

The biotin-Au chip was characterized using the Hitachi's FlexSEM 1000 Scanning Electron Microscope (SEM) (Ontario Technological University, Canada).

2.3 Results and discussion

The sensor for SARS-CoV-2 antigens, such as S protein, is ideal for determination of viral loading in early stages of disease and for drug screening, due to its binding with the ACE2 receptor.^{3,4,9,13,40,49,140,141} Figure 2.1A illustrates the viral structure with the S protein highlighted, which is located at the outer coating of the virus. The S protein is composed of S1 (B), and S2 (D) domains (Figure 2.1). The S1 domain is surface exposed, while S2 domain is membrane bound. In addition, the S1 domain also contains the RBD sequence (C) (Figure 2.1) which has been recently identified as the critical binding site for ACE2

receptor and represents the potential drug target. In the current study, S1, RBD and S2 proteins were tested for with various aptamers using LSPR.

Recent discoveries have been made into identifying a handful of aptamers for binding to the SARS-CoV-2 proteins.⁸⁸ The secondary and tertiary structures of aptamers selected in this study are depicted in Figure 2.2. The secondary structure of S1 aptamers is significantly different from the S1 aptamer-T which contains 6 thymine residues, indicating that T-rich terminal residues may also modulate binding to protein. The S1 aptamer-T and N aptamer-T sequences reportedly bind S protein and N protein, respectively, however, the binding affinities have not been reported yet.¹⁰ In this study, the N aptamer-T (Figure 2.2) was used as a control aptamer for S1 protein.

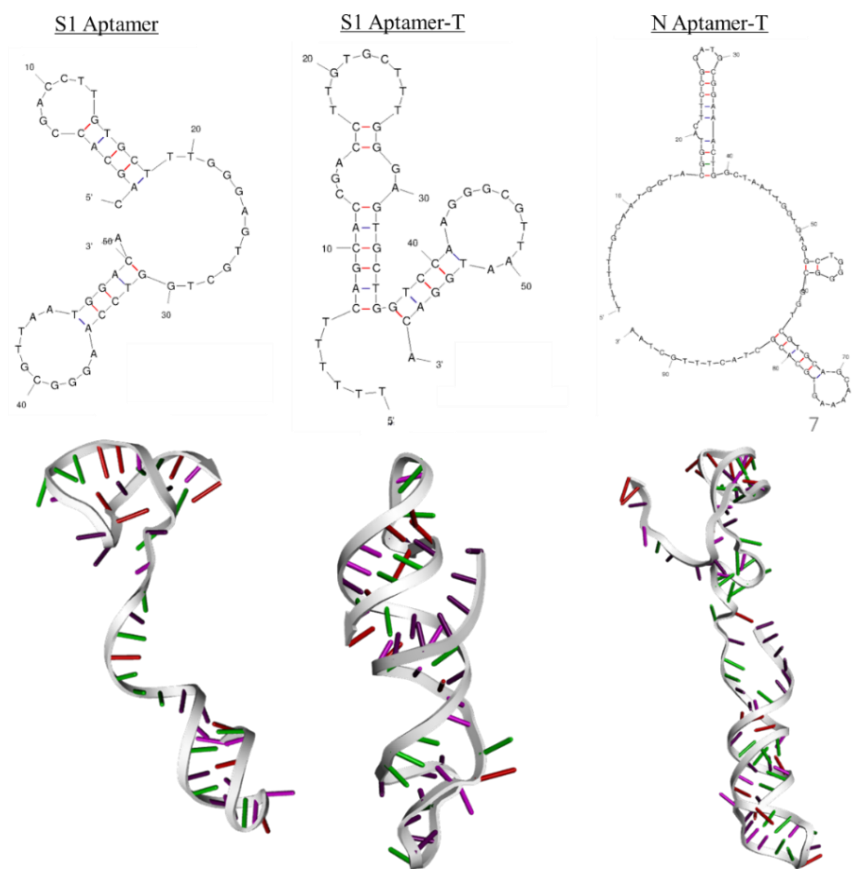


Figure 2.2. Secondary and tertiary structures of the S1 aptamer, S1 aptamer-T and N aptamer-T (2D structures were generated using MFold software and 3D structures were generated using RNAComposer).

2.3.1 Aptasensor fabrication

The benchtop portable LSPR instrument was used with the 2-channel biotinylated-nanogold (nano Au) sensor chip (Figure 2.3A). The Scanning Electron Microscopy was used to characterize the sensor chip surface (Figure A2.1). The size of gold nanostructures on the surface was ~280 nm, with overall particles being homogeneously dispersed. The Au NPs generate the LSPR. The resonance peak of the biotin-Au chip was found at 548

nm (Figure A2.2). The shift in the LSPR absorbance wavelength as a function of analyte was measured and expressed in resonance units (RU).

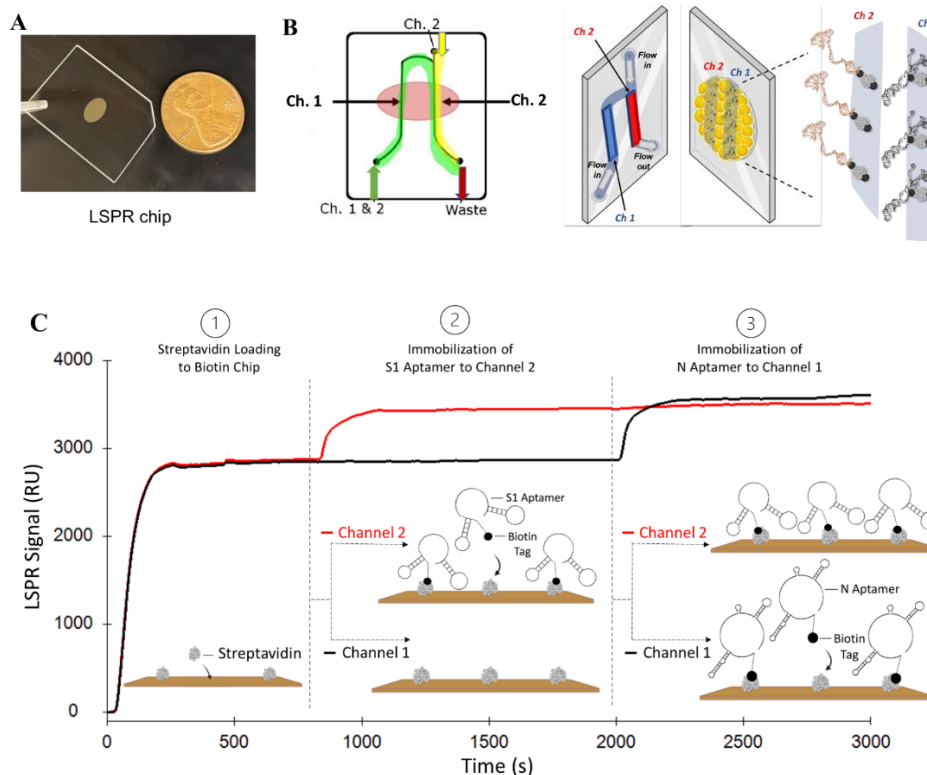


Figure 2.3. (A) Photo of the LSPR chip; (B) Schematic of 2-channel sensor with flow system, and depiction of differential immobilization of S1- and N-aptamers on channel 2 and 1, respectively; (C) Representative LSPR sensorgrams for the fabrication of aptasensors using 2-channel system. The streptavidin-biotin-AuNP surface functionalization (1) on channel 1 and 2, followed by biotinylated S1-aptamer immobilization (2) on channel 2, then N-aptamer immobilization on channel 1 (3) ([streptavidin] = 0.5 μM ; [aptamer] = 50 $\mu\text{g mL}^{-1}$; flow rate = 20 $\mu\text{L min}^{-1}$).

The LSPR sensorgram was then collected as the signal (RU) (y-axis) versus time (s) (x-axis). The 2-channel system (Figure 2.3B) allowed for immobilization of two distinct

aptamers for simultaneous measurements on both channels. Once the analytes interact with the surface, the plasmon resonance peak changes position. The 2-channel system is very beneficial because it allows for the measurements of positive and negative samples at the same time, in order to validate the sensor. The fabrication of the aptasensor was based on using a biotin-Au chip and functionalization with streptavidin (Figure 2.3C). The biotinylated aptamers were subsequently immobilized onto specific channels (Figure 2.3C) and allowed for monitoring protein binding in real-time. As seen in Figure 2.3C, streptavidin–biotin-Au modification resulted in a continuous increase in the LSPR signal, on both channels, during the association phase, indicating streptavidin–biotin binding. Due to the 2-channel system, the LSPR chip allowed for simultaneous monitoring of two separate sensor surfaces during measurement. For example, the biotinylated S1 aptamer was immobilized as a specific recognition probe for S1 protein on channel 2 (Figure 2.3B), while the biotinylated N aptamer was immobilized on channel 1 and tested as a non-interactive control for the S1 protein. Similarly, S1-T aptamer could be immobilized on a channel 1 while S1-aptamer was loaded onto channel 2 (Figure A2.3). Hence, both positive and negative samples (control) can be analyzed on a single LSPR chip by using the 2-channel system.

2.3.2 Optimization of aptamer concentration, buffer composition and regeneration conditions

To ensure sufficient coverage of the aptamer on the sensor surface, the working aptamer concentration of $50 \mu\text{g mL}^{-1}$ was used for all aptamers tested. For all aptamers at this concentration, the signal obtained surpassed the calculated minimum immobilization target

set during the immobilization step (Figure A2.4). Additional concentration of S1 aptamer was also used ($16 \mu\text{g mL}^{-1}$), with repeat injections (Figure A2.5) and cumulative RU response was similar to that of a single injection of $50 \mu\text{g mL}^{-1}$ (~ 530 RU). Hence, $50 \mu\text{g mL}^{-1}$ was considered to be optimal.

Additional aptamer injections did not result in an increase in LSPR signal significantly, indicating that the sensor surface was saturated with the aptamer. The composition of binding/ running buffer was adopted from the previously reported literature, to include 0.05% Tween 20 and 0.1% BSA in order to minimize non-specific binding.⁸⁸ One of the main advantages of using LSPR assay over other analytical methods such as ELISA, is the ability to reuse the sensor for multiple measurements. To attain a reusable sensor surface after analysis of a sample, the bound analyte had to be released from the aptamer binding partner, through a regeneration step. Optimization of this step involved selecting the appropriate concentration for the regeneration solution that would break up the protein-aptamer interactions, without compromising the aptamer on the surface or the streptavidin–biotin layer. Here, 0.01%, 0.1% and 0.5% SDS solutions were tested to determine the optimal regeneration buffer concentrations for this sensor. These conditions were also used in other SPR publications.^{142,143}

After injection of 0.01% or 0.1% SDS solution, the final signal response remained unchanged, indicating insufficient surface regeneration at these concentrations. However, when 0.5% SDS buffer solution was used, optimal regeneration capacity ($\sim 91\%$ surface recovery) was achieved in a single regeneration step (Figure A2.6). Therefore, for

subsequent experiments, an injection of 0.5% SDS buffer was used for surface regeneration each time.

2.3.3 Quantification of S1 protein with S1 aptasensor

Figure 2.4A shows concentration dependent LSPR binding curves of the S1 protein in buffer solution. Increasing the concentration of S1 protein from 0–32 nM (0–2.5 $\mu\text{g mL}^{-1}$), resulted in an increase in the response signals. From the LSPR binding curves, the LSPR signal at 800 s was used to calculate LSPR signal difference and generate the calibration plot (Figure 2.4B). The LSPR signal difference was calculated as the difference between the final LSPR signal (at 800 s, I_f) and the initial signal prior to S1 protein injection (at 100 s, I_i). A linear range was established in 0–16 nM (0–1.25 $\mu\text{g mL}^{-1}$) with a significant linear correlation ($R_2 = 0.99$). Similarly, the LOD and LOQ values for the S1 protein of SARS-CoV-2 were calculated to be 0.26 nM and 1.05 nM, respectively.

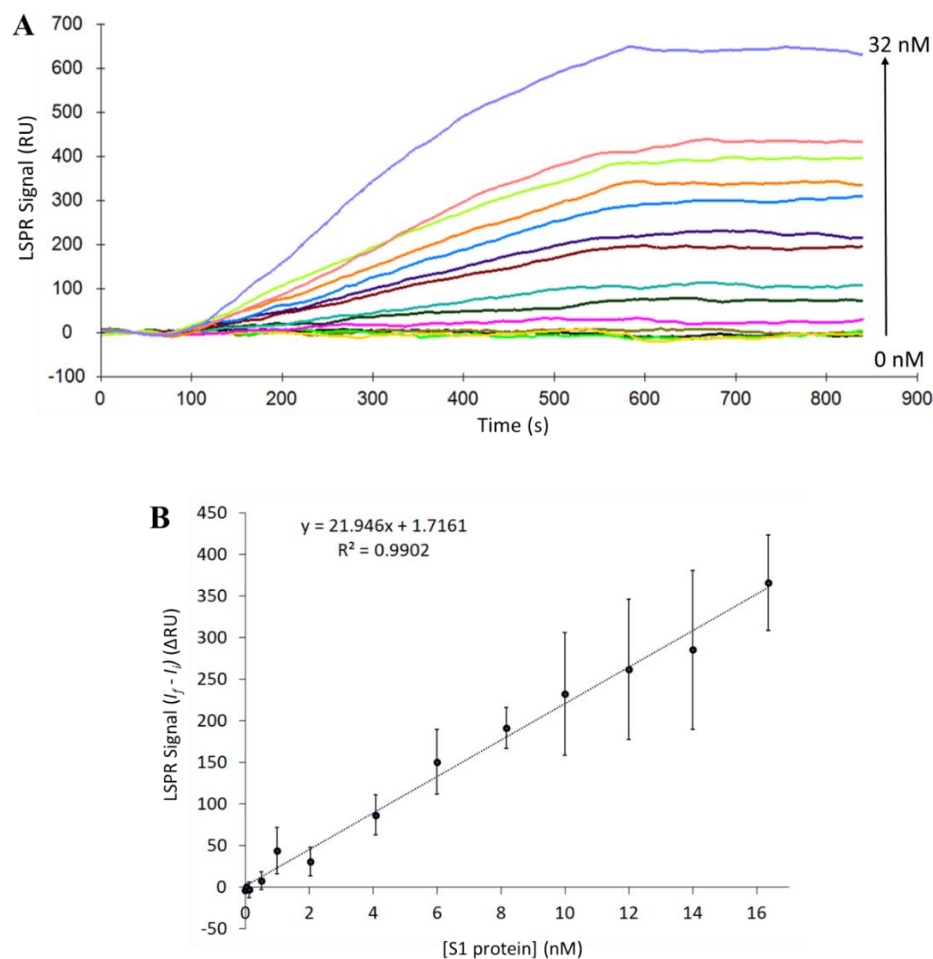


Figure 2.4. (A) Representative LSPR sensorgrams for S1 protein binding to the S1 aptasensor as a function of S1 protein concentrations; (B) Plot of LSPR signal change as a function of S1 protein concentrations derived from sensorgram (A) ([S1 protein] = 0-32 nM (0-2.5 $\mu\text{g mL}^{-1}$); flow rate = 10 $\mu\text{L min}^{-1}$).

2.3.4 Selectivity of aptasensor for S1 protein

To assess the selectivity of the S1 aptasensor, the S2, RBD and BSA proteins were also screened. The S1 aptasensor was capable of differentiating the S1 protein from other SARS-CoV-2 surface proteins and BSA (Figure 2.5A). The S1 protein at 2.5 $\mu\text{g mL}^{-1}$

produced the greatest LSPR signal (663.65 ± 27 RU). The RBD protein resulted in a signal increase by 108.23 ± 5 RU, suggesting some binding to the S1 aptamer (Figure 2.5C). By contrast, BSA (-17.29 ± 4 RU) and S2 (-16.13 ± 10 RU) proteins resulted in a negligible binding to S1 aptamer and some baseline drifting. The LSPR data are comparable to the flow cytometry results wherein the S1 aptamer did not bind to the S2 subunit of the SARS-CoV-2 or BSA.^{88,133} A control aptamer sensor, the N aptamer-T sensor resulted in a small signal change for S1 protein (126.58 ± 41.67 RU) which was only ~20% of the signal obtained with the S1 aptasensor (Figure 2.5B and C). There was also no evidence of significant binding of RBD (13.63 ± 5.64 RU), S2 (4.15 ± 5.81 RU), or BSA (-10.30 ± 3.55 RU) protein to N aptamer-T sensor. In addition to S1 aptamer, the S1 aptamer-T was also tested, and this sensor exhibited similar binding affinity to S1 protein as S1 aptamer, indicating that T residues did not interfere with binding (Figure A2.8). The LSPR curve fitting was performed using the 1:1 binding model to obtain the k_a , k_d and K_D values for all SARS-Cov-2 proteins with S1 aptamer sensor surface (Table A2.1 and Figure A2.9).

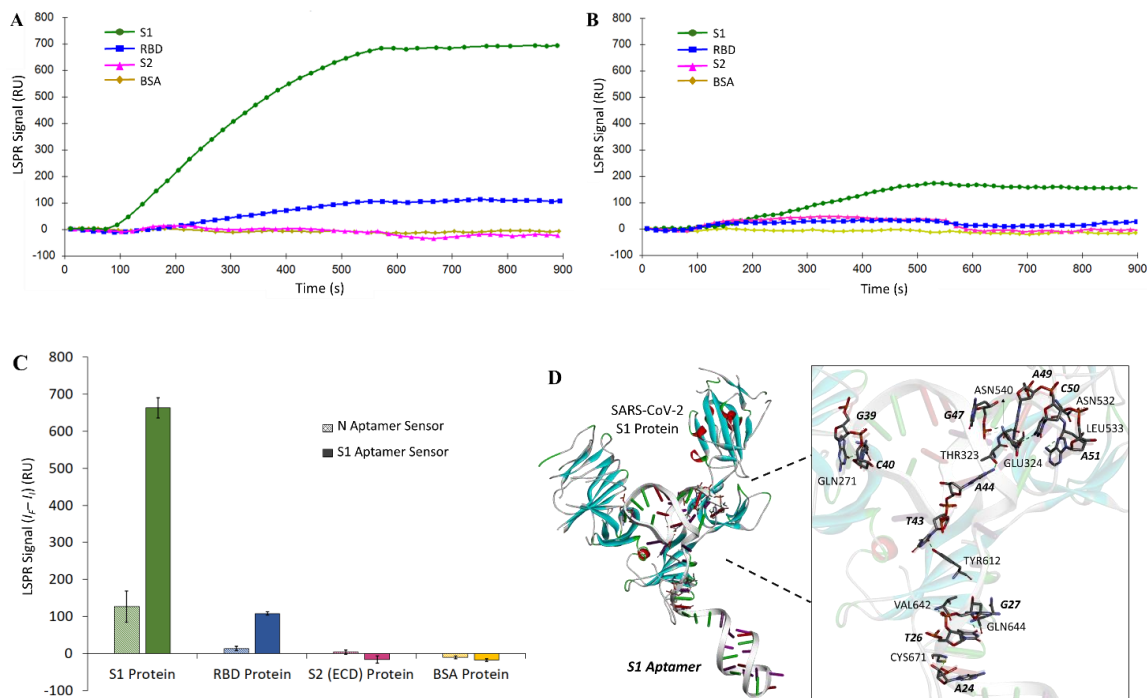


Figure 2.5. Representative LSPR sensorgrams of S1, RBD, S2 and BSA protein binding to (A) S1 aptamer sensor and (B) N aptamer-T sensor. (C) Plot of LSPR signal differences for binding of S1, RBD, S1 and BSA proteins to N aptamer-T sensor or S1 aptamer sensor ($[Proteins] = 2.5 \mu\text{g mL}^{-1}$, (N-T or S1 aptamer) $= 50 \mu\text{g mL}^{-1}$); (D) Molecular docking modelling of S1 protein and S1 aptamer using PatchDock WebServer and visualized with Discovery Studio Visualizer Software.

For S1 protein, the corresponding k_a and k_d values were calculated to be $9.26 \times 10^4 \pm 1.05 \times 10^4 \text{ M}^{-1} \text{ s}^{-1}$ and $3.72 \times 10^{-5} \pm 1.66 \times 10^{-5} \text{ s}^{-1}$, respectively with a K_D value at $0.41 \pm 0.23 \text{ nM}$. The S2 and RBD proteins exhibited higher K_D values, $6.25 \text{ nM} \pm 0.69 \text{ nM}$ and $17.2 \text{ nM} \pm 13.7 \text{ nM}$, respectively. In addition, the SARS-CoV-2 protein binding to the S1-T and N-aptamer was also experimentally evaluated (Tables A2.2–2.3 and Figure A2.10–11). With all aptamers, S1 protein exhibited the lowest K_D values compared to other

proteins tested. In addition, S1 protein binding affinity to aptamers was rank ordered: S1 > S1-T > N aptamers.

The binding affinity between aptamers and proteins of SARS-CoV-2 have been previously determined by using: the Enzyme-Linked Aptamer Binding Assay (ELAA), flow cytometry.^{88,131} The reported K_d values for the aptamer–protein complexes ranged from 2–25 nM, depending on the aptamer and protein tested.

Hence, the LSPR data indicated high selectivity of the S1 aptasensor for the S1 protein, compared to other SARS-CoV-2 spike protein domains and BSA.

In addition, the selectivity studies with S1 protein and S1 aptamer were also performed in the co-presence of various SARS-CoV-2 proteins, to test for potential interference and to mimic more closely the biological setting. When the following protein mixtures were tested: S1 + N, S1 + N + RBD, S1 + N + RBD + S2, the LSPR signal was similar to the S1 only sample (Figure A2.12†). Notably, in the presence of other proteins, significantly longer dissociation step was observed.

To better understand the interactions between S1 aptamer and S1 protein, we performed molecular docking studies. From the nucleotide sequence of S1 aptamer, the 2D structure was generated by Mfold server. Next, the 3D structure of ssRNA was generated using RNAComposer and converted to the ssDNA tertiary structure.^{137,144,145} The MDS was performed to refine the 3D structure of the S1 aptamer (Figure 2.2). The 3D structure of each protein was rendered using the RCSB PDB data bank (ID: 6VSB).¹³² Molecular docking was performed using the PatchDock and visualized with Discovery Studio Visualizer Software to model the structure of aptamer–protein complex.^{138,139,145}

PatchDock is a geometry-based molecular docking algorithm employing shape complementarity principles and local feature matching. The aptamer–target complex was evaluated by a scoring function based on both geometric fit and atomic desolvation energy. The root mean square deviation (RMSD) clustering is applied to determine the top-scoring aptamer–target complex. Following the docking, the geometric score, desolvation energy, interface area size and the actual rigid transformation of the top-scoring aptamer–target complexes were available. From the top docking solution, the resulting S1 aptamer–S1 protein complex (Figure 2.5D) depicted the binding interface near the 3' terminal of the aptamer forming hydrogen bonds with specific amino acid residues from S1 protein. The amino acids which participated in binding included the S1 domain (Tyr612, Val642, Gln644 and Cys671, among others).

Notably, the loop that connects S1 domain with RBD (Thr323, Glu324, Asn532, Leu533, and Asn540) also participated in binding to the aptamer, however, the aptamer did not interact with the RBD domain directly. Hence, it is not expected that S1 aptamer would bind RBD protein significantly, which is in line with the experimental LSPR data.

2.3.5 S1 aptasensor selectivity for S1 protein across related coronaviruses

We have demonstrated that the S1 aptasensor provided high selectivity and sensitivity for the SARS-CoV-2 S1 protein. However, it should be noted that SARS-CoV-2, specifically the S protein shares 76–78% similarity in the amino acid sequence with SARS-CoV.^{9,140} Thus, a comparison of SARS-CoV-2 S1 protein (76.45 kDa) with the S1 protein of SARS-CoV (74.4 kDa) was performed to assess cross-reactivity of the S1 aptasensor (Figure

2.6A). The LSPR binding curves in Figure 2.6A indicated initial strong binding between the S1 protein of SARS-CoV and S1 aptasensor. However, during measurement, the LSPR signal decayed over time during the dissociation phase indicating that the SARS-CoV S1 protein was less strongly bound to the S1 aptamer compared to the SARS-CoV-2 S1 protein. The stark contrast between the two proteins was evident during the dissociation phase (see Figure 2.6A). From the LSPR binding curves, the LSPR signal change was calculated for both proteins (Figure 2.6B) by comparing the LSPR responses at 1600 s (the end of dissociation phase). The S1 aptasensor bound S1 of SARS-CoV-2 (~750 RU) preferentially compared to SARS-CoV (~300 RU). The additional molecular docking studies (Figure A2.13) indicated that the SARS-CoV S1 protein bound to the aptamer in a different manner from SARS-CoV-2 S1 protein. The proposed binding sites of SARS-CoV S1 protein to aptamer include Asn122, Asp166, Arg183, Tyr42, Tyr300, Ile652, Pro651 and Ala654, none of which are shared with SARS-CoV-2 S1 protein binding pocket. Hence, the experimental differences observed in the LSPR are in agreement with the molecular docking studies. The LSPR was conducted for a series of SARS-CoV S1 protein concentrations and the data was fitted by using the 1:1 binding model (Figure A2.14 and Table A2.4) to obtain the k_a , k_d and K_D values. The corresponding k_a and k_d values were calculated to be $3.99 \times 10^5 \pm 2.65 \times 10^4 \text{ M}^{-1} \text{ s}^{-1}$ and $1.17 \times 10^{-3} \pm 2.10 \times 10^{-4} \text{ s}^{-1}$, respectively with a K_D value at $2.9 \pm 0.4 \text{ nM}$. The comparison of on and off rates experimentally determined, clearly shows faster association and faster dissociation by SARS-CoV S1 protein compared to SARS-CoV-2 S1 protein. Additionally, the K_D value of SARS-CoV S1 was ~5 times smaller than that of SARS-CoV-2 S1 protein.

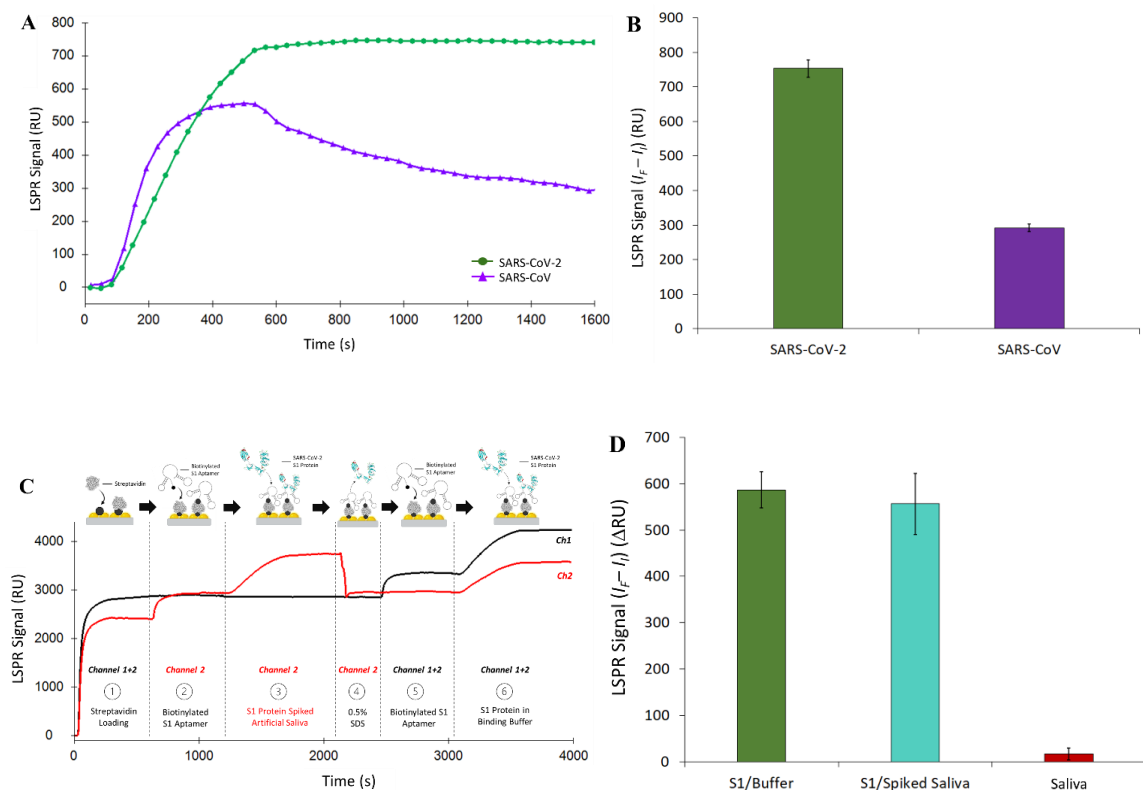


Figure 2.6. (A) LSPR sensorgrams and (B) plot of LSPR signal change for SARS-CoV-2 S1 and SARS-CoV S1 protein binding to S1 aptasensor ($[Protein] = 2.5 \mu\text{g mL}^{-1}$; $[S1 \text{ aptamer}] = 50 \mu\text{g mL}^{-1}$; Flow rate = $10 \mu\text{L min}^{-1}$; dissociation = 15 min; signal change measured at 1600 s). (C) LSPR sensorgrams and (D) plot of LSPR signal change for SARS-CoV-2 S1 protein in spiked buffer solution (channel 1 + 2) compared to 100x diluted spiked artificial saliva solution (channel 2) ($[S1 \text{ protein}] = 2.5 \mu\text{g mL}^{-1}$; signals represent average of triplicate measurements with standard deviation shown as error bars).

2.3.6 S1 protein detection in spiked artificial saliva and serum albumin

The performance of the S1 aptasensor was tested in complex mixtures such as an artificial saliva and serum albumin, to mimic the biological conditions, and compared to the buffer

solution. The 2-channel system allowed for normalization and calibration of the samples in these biological fluids mimics. Figure 2.6C shows the S1 protein in spiked artificial saliva binding to the channel 2 (step 3), and S1 protein in buffer binding to the channel 1 + 2 (step 6). Similar, experiments using 2-channel system were performed for spiked serum albumin samples (Figure A2.15). Hence, the calibration or normalization of the sample may be performed on the same chip by comparing the LSPR signal (RU) of the sample (spiked saliva or serum albumin) versus the signal (RU) of the standard solution (spiked buffer). The 100× diluted artificial saliva resulted in a negligible signal increase of 16.14 RU (Figure 2.6D), indicating minimal non-specific binding from components of the artificial saliva to the sensor. When the diluted artificial saliva was spiked with S1 protein, the SPR signal increased to 556.95 ± 65.98 RU which was similar to the signal achieved for spiked S1 protein in buffer (586.91 ± 38.99 RU) using the same sensor chip for comparison (Figure 2.6D). Thus, a $95 \pm 18\%$ recovery of S1 protein signal was calculated for the diluted artificial saliva sample. Similarly, 1000× diluted serum albumin solution resulted in no signal change, indicating no interference by the complex mixture (Figure A2.16). In addition, the spiked serum albumin samples had similar binding curves and LSPR RU values as the spiked buffer samples, with estimated $92 \pm 9\%$ recovery. Data indicate that the aptasensor is a promising platform for sensing antigens of SARS-CoV-2 in complex solutions, such as those that mimic the biological fluids.

2.3.7 Repeatability and shelf-life

The aptamer sensor was also tested for its repeatability by performing 9 injections (N = 9) of S1 protein with intermittent surface regeneration prior to each injection. On average, the

LSPR signal of 312 ± 41 RU was observed for S1 protein which indicated that the sensor was stable over multiple injections, allowing analysis of 9 samples without any sensor degradation and with the average % error at $\pm 9.1\%$, which is below 10% mark (Figure A2.17).

In order to expand the assay utility towards fabrication of a ready-to-use sensor, the aptasensor was fabricated offline (prepared outside of the instrument). The goal was to fabricate a sensor preloaded with the aptamer for SARS CoV-2 for its immediate use by a non-expert, and to minimize sample preparation, volumes used and reagent requirements by the user. Overall, the projected cost to produce each modified LSPR chip would be approximately 82 CAD (~\$4 for aptamer immobilization and \$78 for the biotin coated chip), if only 1 sample is measured. Considering the excellent reusability of the sensor chips, the anticipated cost would be approximately \$9 per sample (where $N = 9$). On the other hand, PCR tests which are more commonly used, can cost around \$30 per test kit, without the possibility of repeat measurements using the same assay.¹⁴⁶ Thus, in addition to the attractive cost efficiency, the current LSPR aptasensor can be manufactured at room temperature, using minimal reagents and in less than 3 h for each sensor chip, with a 10 min processing time per sample.

Briefly, the offline surface functionalization was similar to the online chip fabrication procedure and identical reagents were used. Each reagent was deposited onto a biotin chip by dropcasting and subsequent rinsing. The series of dropcasting steps were conducted to include: HCl, streptavidin, and S1-aptamer. Following surface modifications, the sensor was immediately mounted into the instrument and used ($t = 0$ days) for

measurements of S1 protein or stored in a buffer solution (running buffer) for 10 or 24 days. The repeatability of the offline sensors was also tested by performing 9 repeat injections of S1 protein, with regeneration steps between measurements. It was determined that each sensor was stable regardless of the shelf-life storage time and exhibited excellent repeatability (Figure A2.17 and A2.18). Small changes in the sensor performance with longer storage periods can be associated with degradation of the streptavidin and biotin protein layers and/or decreased stability of the aptamer due to factors such as hydrolysis of nucleic acids. Importantly, no significant differences were observed in performance between online and offline sensors, and even after over 3 weeks of storage time, indicating that such sensors may be viable diagnostic tools for non-experts in a non-laboratory setting.

2.4 Conclusions

Prior to COVID-19 pandemic in early 2020, the identity of aptamers to SARS-CoV-2 proteins were unknown. Since then, a handful of aptamers to S or N protein of SARS-CoV-2 have been identified using various sensing methods. These recent studies, mid world-wide pandemic, clearly show successful application of aptamers in the development of viral sensors. For example, the indirect detection of a virus was achieved by using the aptamers for binding to the S or N proteins, and by subsequently monitoring the glucose-dependent signal using electrochemical means.¹⁰ The hybridization of aptamers to the complementary viral nucleic acids was also reported using an alternative method to traditional PCR assay.⁶⁰ The direct detection of S protein was achieved using an aptamer with a thin film transistor sensor.¹² Compared to the current sensor (LOD = 0.25 nM), other

aptasensors for SARS-CoV-2 proteins exhibited the LOD values in 1 pM–1 nM range.^{10,12,107,131}

In this work, direct and selective detection of S1 protein was obtained using a dual-channel LSPR sensor for the first time. The LSPR sensors allowed for selective monitoring of the S1 protein over other related analytes, including RBD, S2 and SARS-CoV S1 proteins, which points to the importance of the aptamer selection for a specific target. While other methods may provide lower LOD values for the antigen of SARS-CoV-2, they may not offer other advantages that are associated with the present proof-of-concept LSPR aptasensor. Unlike other methods, the LSPR offers a combination of benefits, such as the real-time feedback, fast detection time (seconds-minutes), excellent reproducibility and repeatability (N = 9), selectivity for the specific antigen of SARS-CoV-2, user friendly sensor preparation, and excellent stability/reusability as a function of shelf-life (up to 24 days). In addition, the LSPR provides critical parameters, such as the binding affinity for aptamer–protein complex, compared to other sensors. Since the proof-of concept prototype sensor presented is based on the synthetic targets to validate the concept, it is only at the Phase 1 of the sensor technology development. At this initial stage, the sensor may not be used to diagnose COVID-19 in clinical samples immediately, but rather further optimization of technology is required for the point-of-care applications in real settings. The further optimization steps of the method may include (a) SELEX procedure for aptamers with higher binding affinity; (b) utilizing different sensor surfaces, such gold or carboxylic acid surface, to improve aptamer coverage, and minimize non-specific binding; (c) development a signal amplification method by using aptamer–antibody platform; (d)

development of ready-to-use kits for sample analysis on site; and (e) sample enrichment by using aptamer-beads, among others.

The sensor exhibited excellent performance in complex mixtures, good repeatability, reusability, and shelf-stability, with equal performance of online and offline-prepared sensors. Given the high affinity of aptamers for their targets, and excellent tunability, versatility and stability of aptamer-based sensors, future sensors for SARS-CoV-2 and its variants are likely. In addition, the real-time binding assay, such as LSPR, will allow for screening of other aptamers to improve assay sensitivity and to extend the assay applicability, as well as screening of potential therapeutics targeting viral infections.

Chapter 3:

Evaluation of amide and gold-thiol covalent coupling methods for studying aptamer-protein interactions

3.1 Introduction

The COVID-19 pandemic introduced unexpected pressure on health care and the personnel responsible for sample testing and diagnosis of health-related issues. With the rapid spread of the virus, and the inherent high demand for testing during the pandemic, rapid and efficient detection methods for viral infections were frantically needed but were not widely available. Thus, it was evident that new, alternative solutions for diagnosis of viral diseases, that did not rely on the use of conventional methods were required. Recently, biosensors for rapid detection of SARS-CoV-2 have been introduced and developed as an alternative to conventional PCR or serological methods.^{38,43,45,51,53,62,147,148}

In Chapter 2, the development and optimization of an aptasensor for the selective detection of the SARS-CoV-2 S1 protein was presented. However, the sensitivity achieved using this method based on streptavidin-biotin coupling of the bioreceptor, still needs improvement in order to move to the next stage of application in testing clinical samples. Generally, the selectivity, sensitivity, and reproducibility of a biosensor can be influenced

by the stability and strength of the bond between the surface coating and the bioreceptor.¹⁴⁹ Thus, one way to improve the performance of the aptasensor would be to modify the surface chemistry to which the bioreceptor is attached.

Surface based biosensing techniques, such as LSPR, provides users the flexibility of choosing the surface chemistry that is the best fit for their assay. The sensor chip is comprised of three layers: (1) the glass substrate, (2) gold nanoparticles (AuNPs) and (3) the functionalized chemical coating to which the ligand (bioreceptor) is attached (Figure 3.1).¹¹³ The choice of sensor surface used depends on the properties of the ligand and its capability for attachment to the particular surface. For example, surfaces coated with biotin and streptavidin layers are used for coupling biotinylated ligands (Chapter 2); carboxylic acid coated surfaces for coupling to ligands with available amine groups, and so on (Figure 3.1).^{113,149} Users may also have the option to customize their own surface chemistry or attach the ligand directly to the AuNPs (i.e., no chemical coating needed), using bare Au surfaces (Figure 3.1).¹⁴⁹

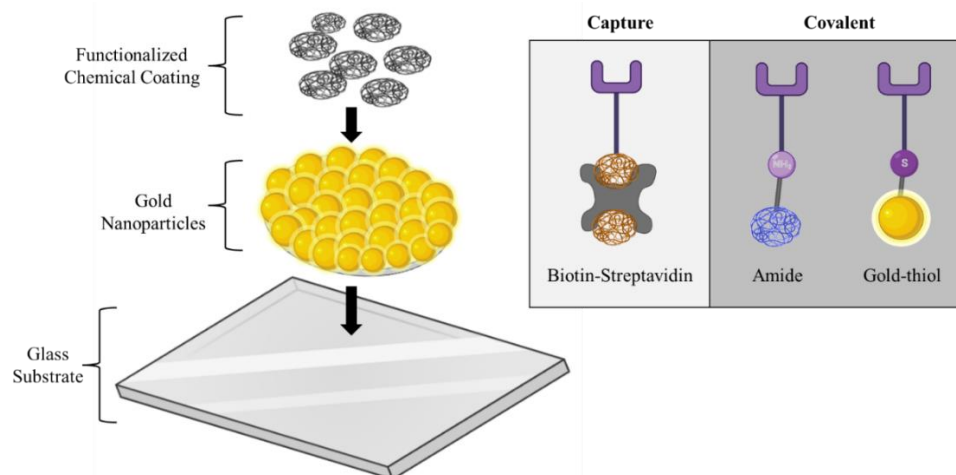


Figure 3.1. Schematic of elements of the LSPR sensor surface and various surface chemistries used for attachment of ligands. Created using biorendor.com.

Capture coupling methods such as those based on biotin-streptavidin, nickel-histidine or antibody-protein binding, generally rely on affinity-based reactions between the functionalized chemical coating (e.g., streptavidin) and the capture molecule (e.g., biotin).^{117,149} The biotin-streptavidin based sensors are one of the most common strategies used for studying molecular interactions.^{149–151} This is because the coupling chemistry creates a strong bond with high binding affinity, which makes for a stable sensor surface comparable to covalently bound surfaces, and a more stable sensor surface able to withstand harsh conditions including high temperatures and regeneration processes.^{149,151} Thus, these sensors can have long lifetimes allowing for multiple sample testing and regeneration cycles, as shown in Chapter 2, that can also help with reducing costs per test. However, other costs can be introduced in relation to the reagents required for biosensors based on capture coupling methods. For example, these methods usually need specifically tagged ligands, which calls for more costly chemical or genetic modifications.¹⁴⁹ On the

other hand, covalent coupling methods like gold-thiol (Au-SH) or amide coupling based biosensors are more versatile, generally more stable, and compatible with most biomolecules, and are the focus of this Chapter.^{149,152}

Bare Au sensors are an attractive option for biosensor development due to their flexibility in a wide range of applications pertaining to the fabrication process. For instance, the bare Au surface can be self-customized to create a unique surface that enhances the performance of the biosensor, or it can be used as is for direct attachment of thiol containing bioreceptors. Figure 3.2A demonstrates the fabrication process of a customized surface with the addition of graphene oxide (GO) on a bare Au surface for attachment of a peptide bioreceptor *via* covalent amide coupling.¹⁵³ The GO sheet was first modified using chloroacetic acid to have carboxylic acid groups available for immobilization of the bioreceptor. The bare Au chip was functionalized *via* covalent attachment of cystamine self-assembled monolayers. Then, the carboxyl GO sheet was attached to the exposed NH₂ end of the cystamine using EDC/NHS chemistry. In the final stage of the fabrication, the peptide was immobilized onto the GO-Cys-Au surface. Electrochemical impedance spectroscopy (EIS) analysis of the peptide-GO-Cys film on a Au electrode demonstrated that the inclusion of the GO increased the conductivity of the surface, thus improving sensor performance.^{153,154} A limit of detection (LOD) of 1.15 pM was achieved in clinical samples which was noted to be well below the detection limit of traditional enzyme-linked immunosorbent assay (ELISA) tests for the target protein. Other modifications involving the creation of protein films or the attachment of bioreceptors and molecules *via* cystamine linkers have been explored.^{155–157} In some cases, a combination of covalent and capture

coupling methods are used for modification of bare Au surfaces to enhance the bioreceptor stability and biosensor sensitivity.^{158,159}

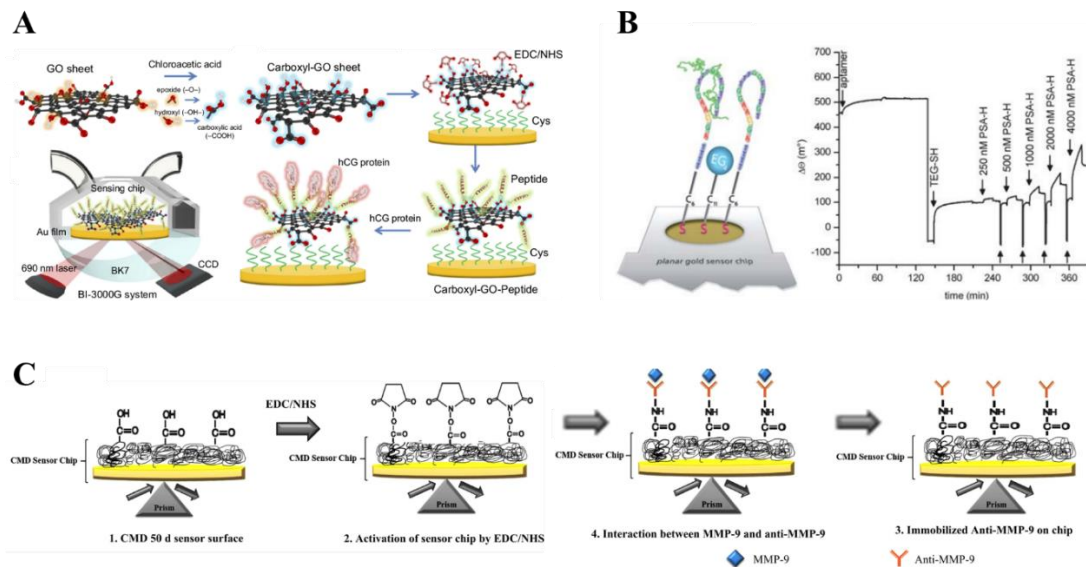


Figure 3.2. Schematic representation of the sensor fabrication procedure (A) of a carboxyl-graphene oxide-peptide based SPR chip from a bare Au sensor for detection of human chorionic gonadotropin protein; Figure reproduced from Chiu et al., (2019).¹⁵³ (B) for direct attachment of a thiolated aptamer for detection of virus coat protein, PSA-H by imaging SPR; Figure reproduced from Lautner et al., (2010) with permission from the Royal Society of Chemistry.¹⁵⁰ (C) of an antibody-antigen based sensor functionalized through amide coupling on a carboxymethyl dextran chip for detection of matrix metalloproteinase-9; Figure reproduced from Mohseni et al., (2016).¹⁶⁰

Less complex fabrication of bare Au sensors may also be done by directly attaching the bioreceptor to the surface through formation of a Au-SH bond.^{150,151,161,162} In this case, the immobilization of the bioreceptor is not dependent on the presence of or interactions with intermediate layers such as carboxyl groups, streptavidin or other chemical coatings.

Therefore, the bioreceptor binding interactions take place closer to the sensor surface, thus influencing sensor stability and sensitivity.^{163–165} As an example, Lautner et al., (2010) fabricated an aptamer based SPR imaging sensor for the detection of a virus coat protein found in plant extracts (Figure 3.2B).¹⁵⁰ Mixed self-assembled monolayers (SAMs) of the SH-aptamers and SH-(1-mercaptopundec-11-yl)tetra(ethylene glycol) (SH-TEG) spacer were attached directly to the Au surface. In a similar approach, Lape et al., (2017) and Piazza et al., (2016), used LSPR and SPR methods to study the interactions between nitric oxide synthases (NOS) proteins and calmodulin (CaM) binding protein.^{151,161} In both cases, for the modification of the bare Au sensor chips cysteine modified NOS peptides were successfully immobilized to the surface *via* Au-SH bonding between the cysteine and the AuNPs.

Another widely employed covalent coupling method relies on amide bond formation for attachment of the bioreceptor to the sensor surface.¹⁴⁹ To do this, sensors are typically fabricated with carboxylic acid which is ideal for binding targets with amine groups. Additionally, compared to other covalent coupling methods, many biomolecules such as proteins and antibodies have a high abundance of amine groups which can be utilized for immobilization to the carboxyl surface by way of EDC/NHS chemistry.^{149,166,167} Chemically derived bioreceptors like aptamers or peptides can be modified during the synthesis process to have available amine groups for amide coupling. Thus, unlike with the use of the native biomolecules, organized orientation of chemically derived bioreceptors immobilized on the surface is possible.^{149,167} The immobilization of proteins and antibodies tend to be more random and uncontrolled. Furthermore, amine modified ligands are generally less costly than its counterparts like thiol or biotin modifications, which is

another advantage of using amide coupling fabrication methods.¹⁶⁸ Mohseni et al., (2016) fabricated an antibody-based sensor for the detection of matric metalloproteinase-9 (MMP-9) (Figure 3.2C).¹⁶⁰ Using EDC/NHS chemistry, the anti-MMP-9 was immobilized onto the carboxyl sensor surface through the primary amine groups. They were able to achieve a LOD of 8 pg/mL and when tested in clinical samples of saliva, the sensor exhibited high binding affinity (0.4 nM) and 94% recovery. Several other SPR based strategies have been developed and tested for studying biomolecular interactions whereby proteins, antibodies or nucleic acids are immobilized on carboxyl sensor surfaces.^{169–172}

Herein, the performance of that optimized S1 aptasensor based on biotin-streptavidin capture coupling (from Chapter 2) was challenged by the development of covalent coupling LSPR sensors using the same bioreceptor (S1 aptamer) and target analyte (S1 protein), but with different surface coupling methods. In this chapter, the fabrication of the S1 aptasensors using (i) bare gold or (ii) carboxyl sensor surfaces were explored, and their performance compared to the streptavidin-biotin aptasensor (Chapter 2) to identify the best performing and most suitable sensor for SARS-CoV-2 detection. As an alternative to conventional laboratory-based tests, the most ideal sensor surface would provide rapid, highly sensitive and selective detection of the SARS-CoV-2 protein along with the benefits of cost effectiveness and ease-of-use.

3.2 Materials and Methods

3.2.1 Chemicals and reagents

SARS-CoV-2 Spike/S1 (cat: 40591-V08B1) His-tagged recombinant protein and SARS-CoV-2 Spike/RBD protein (cat: 40592-VNAH) were purchased from Sino Biological (Beijing, China). Bovine serum albumin (BSA) was acquired from Sigma Aldrich and used as a negative control analyte. Sodium chloride (BioShop), sodium phosphate dibasic (Westlab), potassium chloride (EMD Chemicals), potassium phosphate monobasic (MP Biomedicals), magnesium chloride (Caledon Laboratories), Tween20 (Fisher Bioreagents) were used to prepare the binding/running buffer. The carboxyl coated sensor and amine reagent kit containing carboxyl coated gold nanoparticle (AuNP) sensor chips, activation buffer, blocking solution, 1-Ethyl-3-(3-dimethylaminopropyl)carbodiimide (EDC) and N-Hydroxysuccinimide (NHS) was purchased from Nicoya LifeSciences. For initial surface cleaning of the bare AuNP sensor (Nicoya LifeSciences), ethanol (Fisher Scientific), acetone (Fisher Chemicals), isopropanol (Fisher Chemicals), sulfuric acid, 3% hydrogen peroxide (Delon Laboratories) were used. For aptamer-protein regeneration sodium dodecyl sulfate (SDS) was purchased from BioRad. The blocking molecule used with the bare AuNP sensor was cystamine dihydrochloride purchased from Thermo Scientific. The 5' amine (NH₂-) tagged or thiolated (SS-) ssDNA S1 aptamer (5'-CAGCACCGACCTTGTGCTTTGGGAGTGCTGGTCCAAGGGCGTTAATGGACA-3') and the biotinylated S1-T aptamer (5'-Biotin-TTTTTTCAGCACCGACCTTGTGCTTTGGGAGTGCTGGTCCAAGGGCGTTAATGGACA-3') were purchased from Integrated DNA Technologies.

3.2.2 LSPR measurements

Aptamer-protein interactions were studied using a LSPR instrument (OpenSPR, Nicoya Lifesciences, Canada), equipped with a 2-channel detection system. All experiments were performed at 20 °C and using both channel 1 and 2 simultaneously as active channels. The binding/running buffer used with all experiments consisted of 136.8 mM NaCl, 10.1 mM Na₂HPO₄, 2.7 mM KCl, 1.8 mM KH₂PO₄, 0.55 mM MgCl₂, 0.05% Tween20 (v/v), pH 7.4.⁸⁸ The buffer was filtered with a 0.45 µm nylon syringe filter, non-sterile from Canadian Life Science (cat: SF6054-06N) and used for all dilutions, loop rinsing steps and dissociation phase. All measurements were performed in quadruplicate (N = 4) by acquiring data from both channel 1 and 2. The mean and standard deviation of these measurements were calculated and reported. For analyzing analyte interaction with the immobilized ligand (S1 aptamer or RBD protein), the signal difference ($(I_f - I_i)$ in ΔRU units) from the LSPR binding curves was calculated as the difference between the final LSPR signal (at 800 s, I_f) and the initial signal prior to protein injection.

3.2.3 Fabrication and testing of the S1 aptasensor on a bare Au surface

3.2.3.1 Surface cleaning of the bare Au sensor chip

Before modification of the AuNP sensor surface and testing of aptamer-protein interactions, the AuNP surface was cleaned using a piranha etching treatment and with (“protocol 1”) or without (“protocol 2”) ethanol, acetone and isopropanol washing steps.^{151,161,173} Following protocol 1, the bare AuNP sensor chips were first rinsed thoroughly with ethanol, then acetone and lastly, isopropanol. 50 µL of isopropanol was

spotted over the AuNP surface covered in a petri dish for 5 min, then dried. For further cleaning, the surface was next treated with a 3:1 piranha acid solution (sulfuric acid and 3% hydrogen peroxide), for 5 min. The chip was rinsed using water then ethanol, and dried between each rinse. Prior to subsequent functionalization with the aptamer (for offline preparation protocol) or installation into the OpenSPR (for online preparation protocol), the bare AuNP chip was submerged in an ethanol bath for a minimum of 2 h then thoroughly rinsed with water and dried. When performing the protocol 2, the washing steps were excluded. Cleaning of the bare AuNP chip involved etching with 3:1 piranha acid solution (sulfuric acid and 3% hydrogen peroxide), for 5 min or 120 min (2 h). The chip was then thoroughly rinsed with water and dried before installation into the instrument.

3.2.3.2 Fabrication of the S1 aptasensor on bare Au surface

Following surface cleaning using protocol 1 or 2, the bare AuNP chip was installed into the OpenSPR. The SS-S1 aptamer was prepared as a 100 μM stock solution by dissolving the solid SS-S1 aptamer (16, 115.6 g/mol, 0.53 mg) in 330 μL water. A 5 mM (1 mg/mL) stock of the cystamine blocker was also made by addition of 2 mg of cystamine dihydrochloride to 2 mL water. The immobilization solution was prepared as a 5:1 cystamine:aptamer mixture with a final concentration of 250 $\mu\text{g/mL}$ cystamine and 50 $\mu\text{g/mL}$ aptamer. The solution was prepared by addition of 50 μL of the stock cystamine solution and 6.2 μL of the stock aptamer solution to 143.8 μL of the binding buffer. The immobilization solution was injected over the bare AuNP surface at a flow rate of 20 $\mu\text{L}/\text{min}$ for 5 min. The aptamer surface was then ready to be used for analyte screening.

3.2.3.3 Assessment of S1 protein interactions with the Au S1 aptasensor

Detection of the SARS-CoV-2 S1 protein was tested using the online or offline prepared S1 aptasensor. From a 0.25 mg/mL stock S1 protein solution, 2 μL was added to 198 μL of the binding buffer to prepare a 2.5 $\mu\text{g}/\text{mL}$ S1 protein solution. All analyte screening was performed by injection of the test solution at a flow rate of 10 $\mu\text{L}/\text{min}$ over the S1 aptamer. Following completion of the association phase for each test, a dissociation period of at least 5-min was allowed where the running buffer washed over the sensor surface. The blank buffer solution, free of any analyte, was also tested and compared as a blank control. A 1 mg/mL stock solution of the BSA protein in water was diluted to 100 nM by addition of 0.5 μL of BSA to 199.5 μL binding buffer and tested as a negative control analyte over the modified surface.

3.2.4 Testing aptamer-protein interactions on functionalized carboxyl sensors

3.2.4.1 Activation of carboxyl surface using amide chemistry

To clean the surface prior to activation of the carboxyl coated AuNP sensor chip, surface conditioning was performed online using 10 mM HCl with a flow rate of 150 $\mu\text{L}/\text{min}$ through channels 1 and 2. An injection of 1:1 EDC/NHS mixture was then performed to initiate surface activation using a flow rate of 20 $\mu\text{L}/\text{min}$. The activated surface was then ready for ligand immobilization.

3.2.4.2 Exploring aptamer functionalization on carboxyl sensor surfaces

A 100 μM stock solution of the NH_2 -S1 aptamer was prepared by dissolving the solid NH_2 -S1 aptamer (15,966.4 g/mol, 1.47 mg) in 922 μL water. For ligand immobilization, the aptamer was diluted to 50 $\mu\text{g}/\text{mL}$ by addition of 6.3 μL of the stock solution to 193.7 μL of the provided activation buffer. Immediately following surface activation, it was injected at a flow rate of 20 $\mu\text{L}/\text{min}$ for a 5-min interaction time.

3.2.4.3 Protein attachment to activated carboxyl surface

0.25 mg/mL stock solutions of the proteins were prepared by addition of 400 μL of water to 0.1 mg of protein solid. After activation of the carboxyl surface, the RBD protein was diluted to the appropriate concentration and injected at a flow rate of 10 $\mu\text{L}/\text{min}$ for a 5-min interaction time. For optimization of the ligand immobilization step, concentrations of 1, 5, 10, 25 and 50 $\mu\text{g}/\text{mL}$ RBD protein diluted in the provided sodium acetate (pH 4.5) activation buffer were tested under all the same conditions. Following immobilization, any free activated carboxyl sites were blocked using a single injection of the provided blocking solution with an amine linked molecule at a flow rate of 20 $\mu\text{L}/\text{min}$.

3.2.4.4 Screening aptamer-protein interactions using the functionalized carboxyl sensor

Following surface modification with the RBD protein, 100 nM S1 aptamer was prepared in the binding buffer and introduced at a flow rate of 10 $\mu\text{L}/\text{min}$ for 10 min. Under similar conditions, a blank buffer and 100 nM of the BSA protein were also tested using the

functionalized RBD sensor. Following each analyte injection, a dissociation period of at least 5 min. was allowed with the running buffer washing over the sensor surface.

3.3 Results and Discussion

3.3.1 Au-thiol coupling using aptamer functionalized AuNP sensor surface

3.3.1.1 Fabrication of the S1 aptasensor on a bare Au surface

Unlike other surfaces such as the streptavidin-biotin or carboxyl, use of non-functionalized (i.e. bare) Au surfaces allows the user either the freedom to customize the surface chemistry for a more unique sensor design or for direct attachment of a thiolated ligand to the surface.^{116,150,155,158} In the development of this S1 aptasensor, direct coupling of a 5'-disulfide modification was explored, allowing for the formation of the covalent Au-thiol (Au-SH) bond (Figure 3.3).^{151,163} The disulfide group was attached to the nucleic acid sequence *via* the 5'-end of the aptamer with a standard 6 carbon spacer (Figure A3.1).

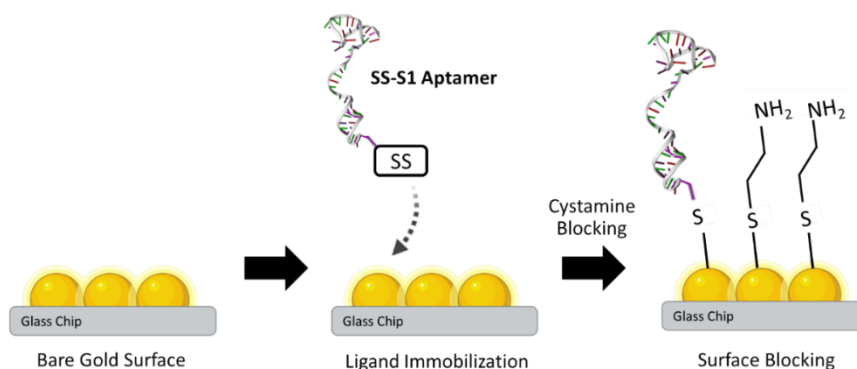


Figure 3.3. Design of the S1 aptasensor fabricated on a bare Au surface using a SS-S1 aptamer, and cystamine surface blocker.

For fabrication of the sensor, surface cleaning, functionalization and blocking were incorporated. Effective loading of a ligand onto Au surfaces, is highly dependent on the efficiency of the cleaning procedure. Thus, the first step in the fabrication of the aptasensor involved offline (outside the instrument) cleaning of the sensor chip. Then, the immobilization solution comprising of a 1:5 ratio of the aptamer (50 $\mu\text{g}/\text{mL}$):cystamine (250 $\mu\text{g}/\text{mL}$) was introduced for functionalization of the sensor with the S1 aptamer.^{151,161} The cystamine was included in the immobilization solution as a blocking agent, to prevent any non-specific binding and to allow sufficient spacing of the immobilized aptamers on the surface as to prevent surface crowding.^{151,156}

3.3.1.1.1 Surface cleaning and functionalization of the bare Au surface

To ensure proper attachment of the bioreceptor for the development of a high performing biosensor, it is therefore important that the surface is clear of any debris that could interfere with the analytical measurements or binding of the bioreceptor and its analyte. Hence, as a part of the biosensor fabrication process, it is important to determine the most effective procedure for surface cleaning.¹⁷³

Figure 3.4 illustrates the steps used in protocol 1 and 2 surface cleaning procedures. In both cases, the bare Au chip underwent a vigorous cleaning procedure to remove any unwanted debris from the sensor surface. Typically, with Au surfaces an acidic solution referred to as a piranha solution comprised of sulfuric acid (H_2SO_4) and hydrogen peroxide (H_2O_2) is used to clean the surface.^{10,70,174} To clean our bare Au surfaces, a 3:1 (H_2SO_4 : H_2O_2) piranha solution was prepared, spotted over the surface and allowed to react.^{151,161,174} Protocol 1 (Figure 3.4A) included several washing steps with ethanol, acetone and

isopropanol prior to the piranha treatment of the Au chip.^{151,175} The washing steps play a role in the improvement of the sensor fabrication process. This has been demonstrated by Park et al. (2004), where they show that when the pre-treatment processes were excluded from the cleaning procedure, the immobilization levels of GO to a Au surface were reduced, compared to when the washing steps were included. Therefore, the pre-treatment of the Au surface with the alcohols and acetone are important for maximizing the effect of the piranha etching process, subsequently creating greater opportunity for increased ligand coverage.^{151,173} Following the washing steps, the surface was treated with the piranha acid solution for 5 min, then rinsed thoroughly with water.¹⁵¹ Finally, an ethanol rinse and soak were done to remove any excess residue from the surface. After installation of the sensor chip to the aptamer immobilization process and protein binding were monitored by LSPR. However, the inclusion of the acetone and alcohol washing steps caused the glass surface to adhere to the flow cell when the chip was installed in the instrument. The sticking of the chip to the flow cell led to breakage of the glass during the extraction of the sensor chip after each experiment was complete. In light of these challenges, protocol 1 was modified to avoid any damages to the instrument or the chip surface, which could in turn lead to leaking and poor sensor performance.

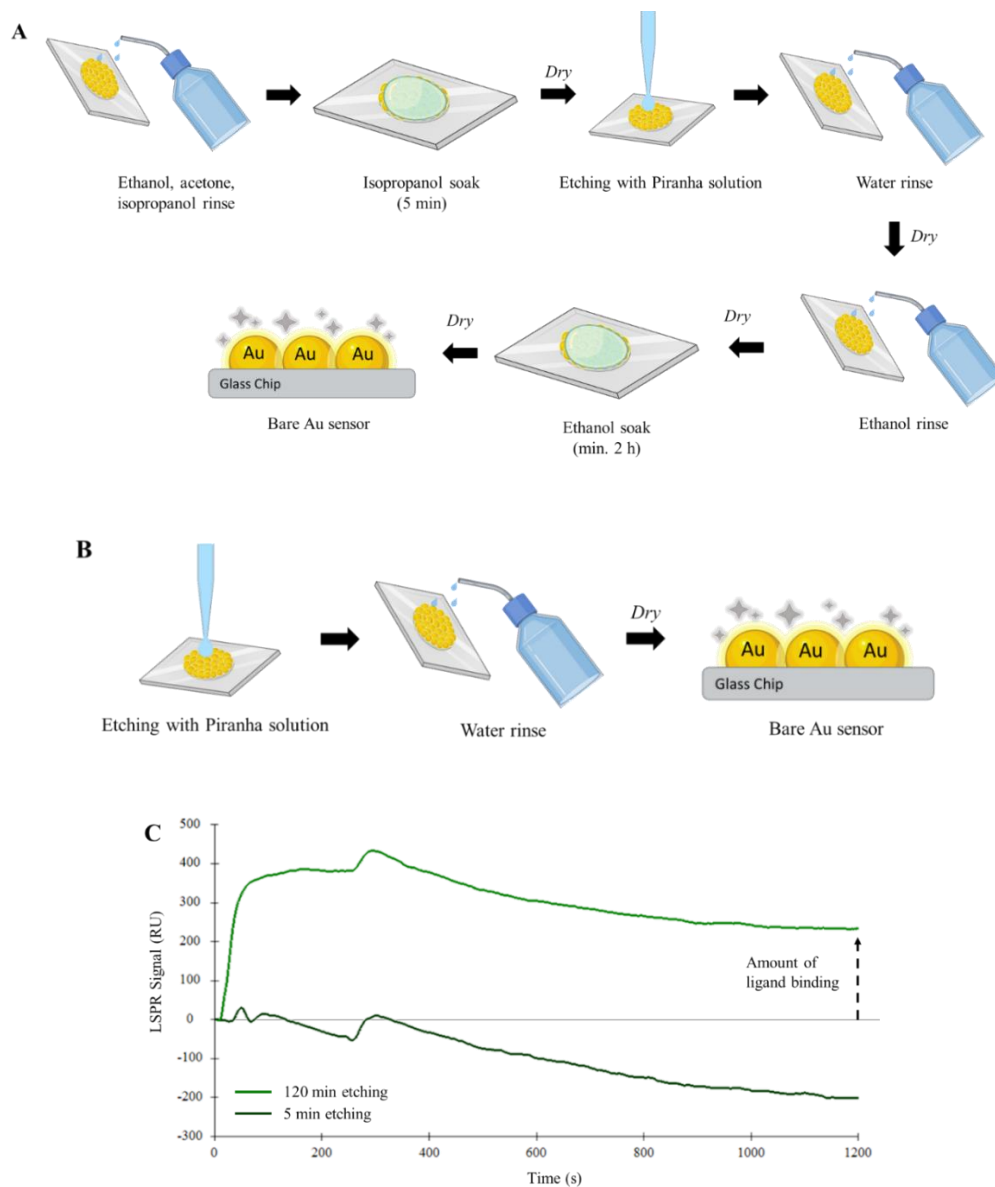


Figure 3.4. Illustration of bare Au sensor chip cleaning process for (A) protocol 1 or (B) protocol 2 to achieve a cleaned bare Au sensor surface; Created using Biorender.com. (C) Representative LSPR sensorgram of surface fabrication with the immobilization solution, following a 5- or 120- min. piranha solution etching. Immobilization solution = [aptamer] = 50 $\mu\text{g}/\text{mL}$ and [cystamine] = 250 $\mu\text{g}/\text{mL}$; Flow rate = 20 $\mu\text{L}/\text{min}$; Dissociation time = 15 min.

The modified cleaning procedure named protocol 2 is illustrated in Figure 3.4B. For protocol 2, all acetone, ethanol and isopropanol washing, and soaking steps were excluded. Instead, the bare Au chip was first treated with the piranha solution, then rinsed with water and dried before continuing with monitoring attachment of the aptamer. However, since the pre-treatment steps were excluded from this protocol, the cleaning procedure was further enhanced by allowing longer etching times (>5 min) for the piranha solution before immobilizing the aptamer.

After completion of the protocol 2 procedure with 5 and 120 min of piranha etching, the immobilization solution was introduced and the LSPR signals representing the aptamer immobilization levels of the bioreceptor were compared (Figure 3.4C). When the immobilization solution was injected after etching for just 5-min, no aptamer attachment was observed, as evidenced by the lack of signal change during the association phase (~10 s – 300 s). This suggested that any non-specific reagents may still be present on the surface and prevent aptamer attachment. Hence, the 5-min etching period allowed was determined to be an insufficient time for the cleaning procedure. Consequently, the time allowed for the piranha treatment was then increased to 120-min. When the immobilization solution was injected after etching for 120-min, an immobilization level of 269.79 ± 35.3 RU was achieved for the S1 aptamer. The increase in the signal and stabilization during the dissociation phase indicated successful S1 aptamer attachment to the Au surface. The aptamer functionalized surface was then ready to be used for the detection of the SARS-CoV-2 S1 protein.

3.3.1.2 Detection of SARS-CoV-2 S1 protein using Au S1 aptasensor

Chapter 2 demonstrated that the S1 aptamer selectively binds the SARS-CoV-2 S1 protein, hence using this S1 aptasensor fabricated on the Au surface, the detection of the S1 protein was also tested. Firstly, the blank buffer (no analyte) and negative control protein (BSA) were tested to ensure that there were no background signals being generated or non-specific binding of non-target compounds. When 2.5 $\mu\text{g/mL}$ of the S1 protein was introduced, the LSPR signal increased by 358.57 ± 48.2 RU signifying successful detection of the S1 protein by the S1 aptasensor. On the other hand, the blank buffer (-43.63 ± 23.8 ΔRU) and BSA (-45.20 ± 14.5 ΔRU) samples generated similar LSPR signals observed as a negative drift, indicating that the signal increase in the presence of the S1 protein was solely due to the formation of the protein-aptamer complex (Figure 3.5A-B).

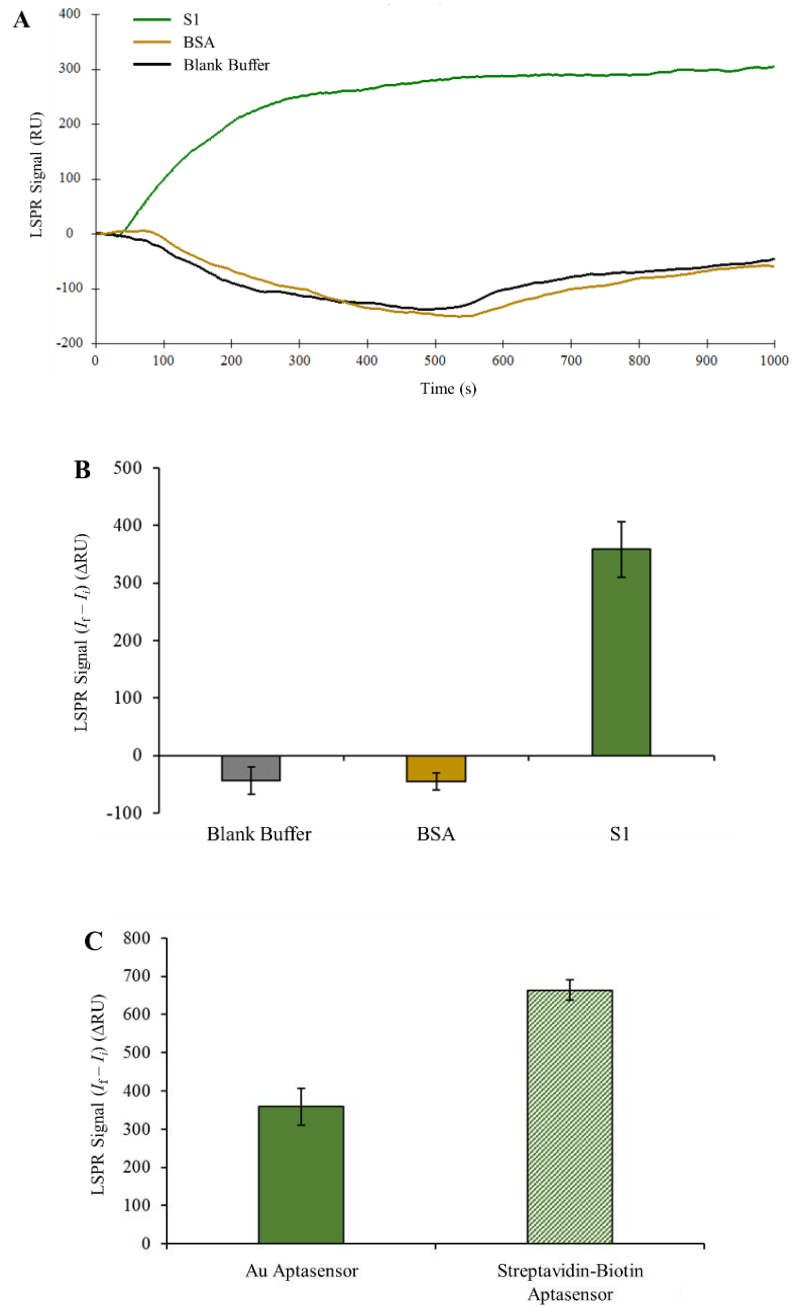


Figure 3.5. (A) Representative LSPR sensorgram and (B) plots of LSPR signals for the blank buffer, BSA and S1 protein screening following the ligand immobilization procedure; (C) Comparison of LSPR signals generated using the S1 aptasensor fabricated

on the bare Au surface or the streptavidin-biotin surface; [Proteins] = 2.5 $\mu\text{g/mL}$; Flow rate = 10 $\mu\text{L/min}$.

The performance of the aptasensors developed on the bare Au surface and the biotin-streptavidin surface can also be compared based on their sensitivity for the determination of the S1 protein. Overall, the streptavidin-biotin aptasensor (Chapter 2) was able to achieve a LSPR signal that was around 2x more than what was achieved using the current Au aptasensor (Figure 3.5C). This means that higher sensitivity is attained using the streptavidin-biotin aptasensor. However, it is important to note that further optimization of the Au aptasensor is possible and should be considered in order to improve the performance of the sensor. For example factors such as, (i) the ratio of the aptamer:cystamine content in the immobilization solution and (ii) the optimal time required for etching with the piranha solution during the cleaning process can have an effect on the amount of the bioreceptor available on the surface. Therefore, with further exploration of the immobilization solution content and the time needed for the cleaning process, the quality of the Au aptasensor can significantly be improved.

3.3.2 Amide coupling using carboxyl sensors

3.3.2.1 Surface activation and fabrication of carboxyl sensors

Carboxylate surfaces are also widely used in the design of biosensors. The carboxyl sensor chips are ideal for the attachment of targets with amine groups. The surface of the sensor chips is coated with carboxylic acid which makes them suitable for amide coupling.

Prior to surface functionalization, activation of the carboxyl sensor is necessary. To achieve this, a standard approach using EDC/NHS for amide coupling was performed as demonstrated in Figure 3.6. The fundamental principle of this coupling reaction relies on the formation of an ester intermediate to activate the carboxylated surface, which is then used for the covalent binding of primary amine ($-NH_2$) groups of the desired ligand (Figure 3.6).^{160,167,168,174,176,177}

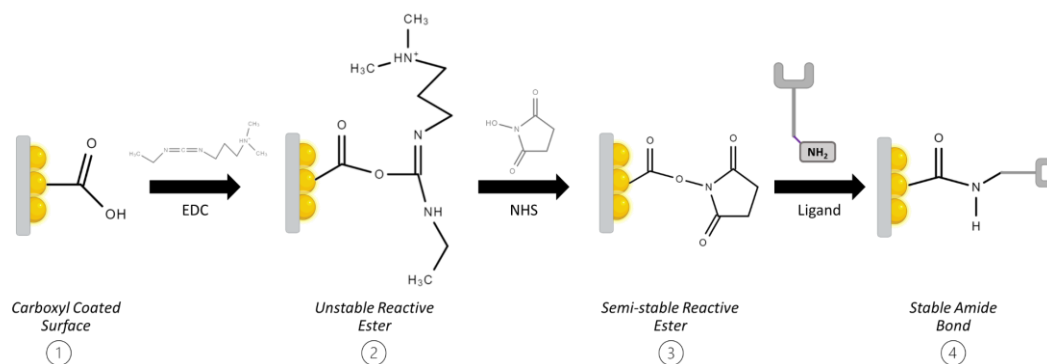


Figure 3.6. (A) Scheme of the activation process for carboxyl coated surface using EDC/NHS chemistry for attachment of an aminated ligand. (B) Representative sensorgram demonstrating the sensor fabrication process.

In this process, the EDC reacts with carboxylic acids on the sensor surface to form an *o*-acylisourea intermediate (see step 2, Figure 3.6).^{168,176,177} Primary amines of the ligand may then act as a nucleophile (i.e., donates electrons) to complex with the *o*-acylisourea and create the amide bond. However, other molecules, such as oxygen atoms in polar environments may also have nucleophilic activity. Hence, using EDC on its own for surface activation is not generally used, as it introduces higher chances of inactivated EDC and lower coupling yields due to the unstable nature of the *o*-acylisourea intermediate.^{174,177} Therefore, the introduction of the NHS is more often done in the presence of the EDC to

improve the efficiency of the reaction.^{174,176} This creates a more stable, hydrophilic NHS-ester that then allows for coupling of desired ligand *via* amide bond formation (see step 3, Figure 3.6). Prior to ligand immobilization, EDC and NHS solutions provided in the NicoyaLife amine couple kit were mixed in a 1:1 molar ratio and used for surface activation. The half-life of the ester formed is on average 4 – 5 h at pH 7.0 and its stability decreases in more basic environments.^{174,177} Therefore, to maximize performance, the attachment of the ligand must be performed in a timely manner as to avoid hydrolyzation of the ester before the amide coupling can occur. To evaluate aptamer-protein interactions using the carboxyl surface, aptamer and protein functionalization were explored using a NH₂-S1 aptamer or the RBD protein, respectively. Both molecules have primary amine groups available for attachment to the activated surface, hence, immediately after the EDC/NHS injection was completed and the LSPR signal was stabilized, the ligand was injected. After the ligand immobilization, a blocking solution provided with the amine coupling kit was used to deactivate any unreactive carboxyl groups on the sensor surface and prevent non-specific binding during analyte screening steps.

3.3.2.1.1 Aptamer functionalization on carboxyl sensor surfaces

For comparison to the performance of other surface chemistries, an aptasensor based on amide coupling chemistry was designed (Figure 3.7A). The S1 aptamer was modified with an NH₂ group at its 5'-end with a 6-carbon spacer (Figure A3.2). To achieve binding of the NH₂-S1 aptamer to the activated carboxyl surface, the aptamer must be prepared in such a way that nucleophilic activity can occur to form the desired amide bond. Thus, following surface activation, a 50 µg/mL solution of the aminated S1 aptamer in a

sodium acetate activation buffer (pH 4.5) was introduced to promote its attachment to the activated surface. With the introduction of the aptamer prepared in the activation buffer, a signal increase during the association phase was observed, but quickly returned to the point of the baseline during the dissociation phase, suggesting unsuccessful immobilization of the aptamer (Figure A3.3).

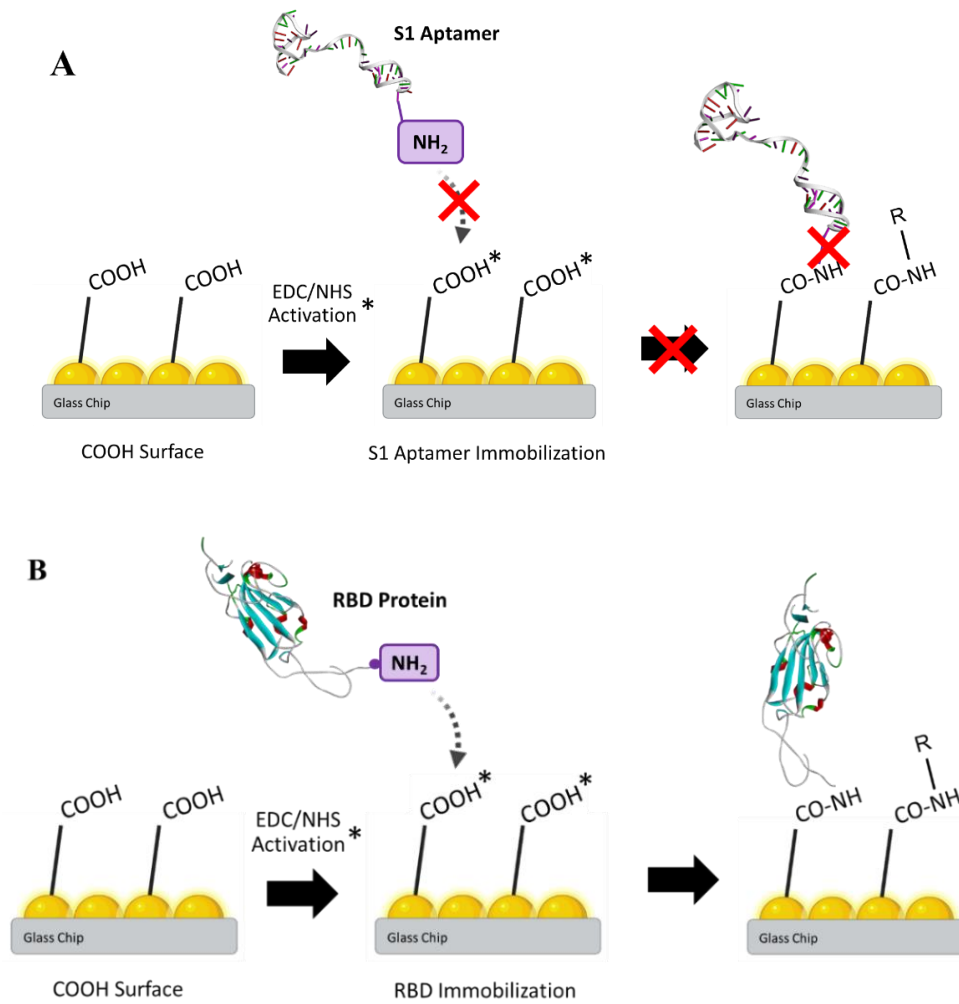


Figure 3.7. Illustration of sensor fabrication protocol for preparation of the (A) aptamer or (B) protein functionalized carboxyl sensor chips. Created using Biorender.com.

The use of the activation buffer is vital for creating an environment that enhances the efficiency of the immobilization step. Generally, the choice of activation buffer conditions depends on the properties of the ligand. Specifically, the pH of the buffer should be at least 80% lower (i.e. 0.5 pH units) than the ligand's isoelectric point (pI).^{167,178,179} The more common buffer formulations used are sodium formate (pH 3.0 – 4.5), acetate (pH 4.0 – 5.5), maleate (pH 5.5 – 7.0), or borate (pH 8.0+) buffer.¹⁶⁷ For this research, a sodium acetate buffer at pH 4.5 which was supplied in the OpenSPR amine coupling kit was used as the activation buffer. The activation buffer was optimized by the manufacturer, specifically for covalent coupling of protein or antibodies to the surface and has been previously used for such purposes.^{169,180–182} Therefore, much of the understanding of the relationship between the activation buffer conditions and the pI of the ligand only supports the covalent coupling of proteins or antibodies to the activated carboxyl surface.¹⁶⁷ Furthermore, there is no published evidence demonstrating that this concept also applies to the attachment of aptamers or other chemically derived ligands. Since no other amine coupling kits were commercially available specifically for nucleic acid coupling, in an effort to keep the use of reagents for sensor development mainstream and to limit cost of production, the commercially available amine coupling kit was used. Thus, under the conditions tested, the unsuccessful aptamer attachment may be due to the incompatibility of the immobilization procedure employed. Since the pI of the S1 aptamer was not known, further efforts towards the determination of an optimal activation buffer should be explored. For example, pre-concentration studies can be executed using activation buffers at various pH values to determine the conditions under which the best immobilization efficiency is achieved.^{152,166,167} Alternatively, other sensor designs such as antibody or

protein functionalization which have been more widely explored can be considered for surface fabrication.

3.3.2.1.2 Fabrication of protein functionalized carboxyl surfaces

Given that the aptamer functionalization could not be achieved, protein functionalized carboxyl surfaces were then prepared as another option for the evaluation of aptamer-protein interactions (Figure 3.7B). By changing the orientation of the assay, the protein becomes the ligand attached to the activated carboxyl surface, and its interaction with binding partners such as antibodies, peptides, proteins, or aptamers can be evaluated.

For attachment to the activated surface, the RBD protein relies on covalent coupling *via* the primary amine groups at the N-terminal and lysine residues throughout the protein. The theoretical *pI* for the SARS-CoV-2 RBD protein is 8.91.^{183,184} Based on conventional amide coupling theory, since the pH of the activation buffer (4.5) was below the *pI* of the ligand, protein immobilization could be achieved. Hence, a protein functionalized carboxyl sensor was optimized for attachment of the RBD protein and further screening of the S1, and S1-T aptamers, which have been shown to bind the RBD protein (Chapter 2) to assess aptamer-protein interactions.

3.3.2.1.2.1 Optimization of immobilization parameters

For optimal performance of the sensor, parameters such as the injection flow rate should be considered to ensure that sufficient interaction time is allowed for the completion of the reaction of interest. The OpenSPR instrument is equipped with a sample loop that holds volumes of up to 100 μL at a time. Therefore, the introduction of samples initiated at a

flow rate of 20 $\mu\text{L}/\text{min}$ would allow for a 5-min interaction time, and a flow rate of 10 $\mu\text{L}/\text{min}$ would allow for a 10-min interaction time and so forth. Standard LSPR protocols recommend ligand immobilization steps be completed using lower flow rates to ensure adequate time for the ligand to complete its attachment to the surface.^{118,167} To determine the flow rate that would allow for greatest surface coverage and the best performing sensor, various periods of ligand interaction times were tested.

Using a 10 $\mu\text{L}/\text{min}$ flow rate, three sequential injections of the RBD were introduced to the activated carboxyl surface (Figure 3.8A). Notably, the first of three sequential RBD injections produced the greatest immobilization level (554.15 ± 155.9 ΔRU), indicating RBD immobilization to the surface (Figure 3.8B). With additional injections of RBD introduced at the same concentration and under the same conditions, smaller signal changes were observed. This suggests that after the first RBD injection, most of the surface coverage is achieved, hence there are fewer active sites for remaining RBD protein to attach to. Thus, with subsequent protein additions, lower signal changes were observed, likely due to less binding events occurring, and indication that the surface is nearing its point of complete saturation. After a total of three injections, the final signal change was 966.99 ± 243.7 ΔRU .

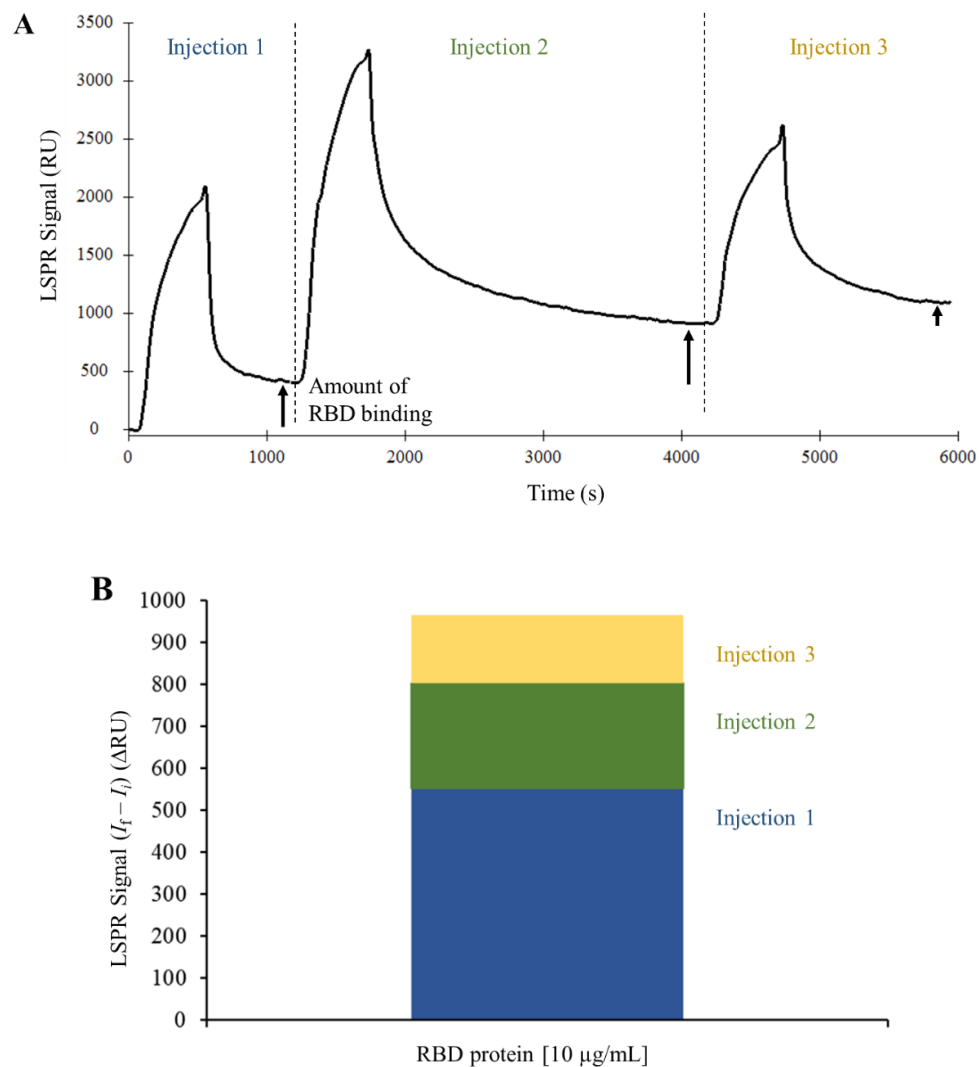


Figure 3.8. (A) Representative sensorgram and (B) average LSPR signal change with sequential addition of RBD protein; for each injection [RBD] = $10 \mu\text{g/mL}$; flow rate = $10 \mu\text{L/min}$.

A higher flow rate ($20 \mu\text{L/min}$) was also considered for the immobilization step (Figure A3.4). The shorter interaction time could be beneficial for minimizing the time required to complete the sensor fabrication process. However, when the interaction time was decreased, lower immobilization levels were achieved ($639.78 \pm 112.3 \Delta\text{RU}$).

Additionally, from the sensorgram it was apparent that the point of equilibrium following association had not been reached, suggesting that the 5-min interaction time was not sufficient to complete the reaction. Since 5 min was too short for the association to be complete, higher flow rates beyond 20 $\mu\text{L}/\text{min}$ were not tested. Overall, greater surface coverage was achieved with a 10 $\mu\text{L}/\text{min}$ flow rate, hence, these parameters were chosen as optimal immobilization conditions and used for all subsequent experiments.

3.3.2.1.2.2 Optimization of ligand concentrations

To further enhance the efficiency of the ligand immobilization step, the protein concentration that would provide the greatest surface coverage *via* a single 150 μL injection was determined. For this evaluation, one injection of 1, 5, 10, 25 and 50 $\mu\text{g}/\text{mL}$ RBD protein was introduced to the activated carboxyl coated AuNP surface (Figure 3.9).¹⁶⁷ Notably, a similar trend in the association and dissociation patterns were observed for all concentrations tested. As demonstrated in Figure 3.9A, a drastic signal increase during the association phase and a slow, continuous signal decrease following the rapid dissociation (>700 s) was observed. This corresponds to >60 % dissociation of the weakly associated protein by ~ 1400 s. It is important to acknowledge the slow protein dissociation as it can indicate potential depletion on the sensor performance over time, thus affecting sensor reproducibility with fewer available binding sites for analyte binding.

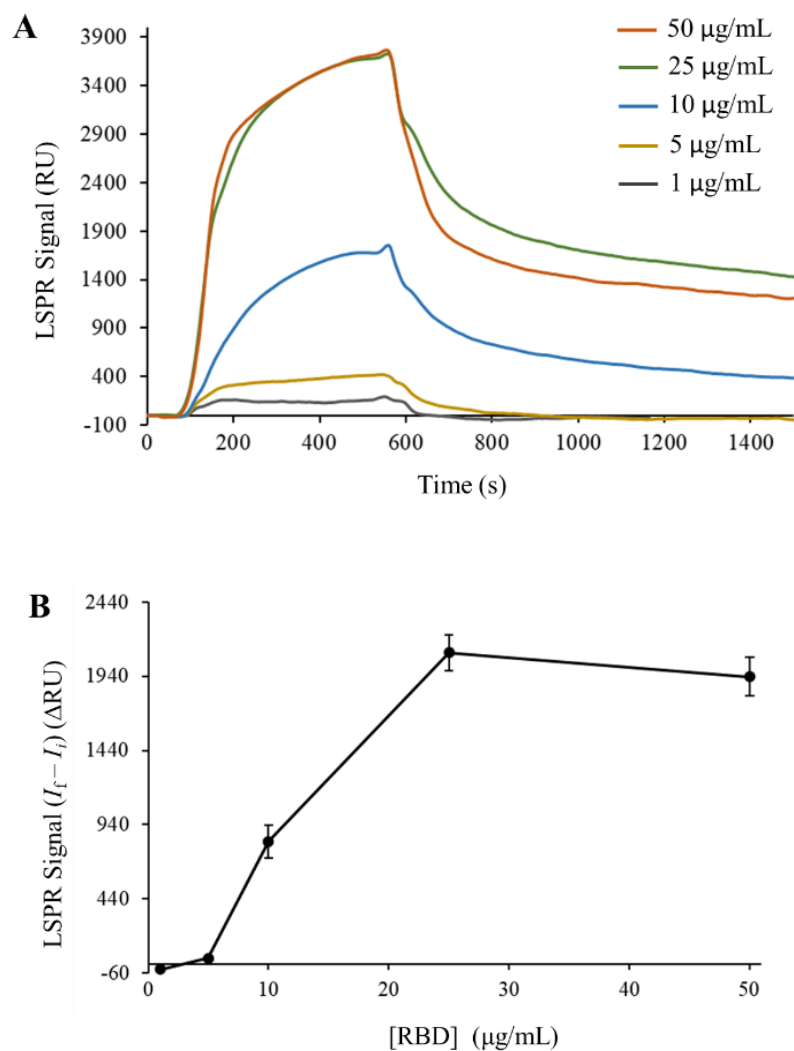


Figure 3.9. (A) Representative LSPR signals and (B) plot of LSPR signal differences showing RBD protein attachment at concentration of 1, 5, 10, 25 or 50 µg/mL to the activated carboxyl coated AuNP surface; flow rate = 10 µL/min; $I_f \approx 740$ s.

Figure 3.9B represents the final LSPR signal change measured at approximately 740 s. Negligible signal change was observed at lower concentrations (1–5 µg/mL) suggesting that no protein bound to the surface, and higher ligand concentrations are needed. When the protein concentration was increased to 10 µg/mL, the final

immobilization level was $825.23 \pm 111.9 \Delta\text{RU}$, demonstrating some ligand attachment to the activated surface. Higher concentrations of RBD were then tested to establish the point at which complete saturation of the surface is attained. Following the introduction of $25 \mu\text{g/mL}$, the ligand immobilization level increased by $2098.53 \pm 120.5 \Delta\text{RU}$. However, increasing the concentration to $50 \mu\text{g/mL}$ had no significant effect on the final immobilization level achieved ($1936.0 \pm 130.9 \Delta\text{RU}$) (Figure 3.9B). Notably, though complete saturation of the surface was apparent, some coverage was lost during the subsequent washing step following the dissociation. The reason for the slight additional loss in the RBD LSPR signal at a higher concentration could be resulting from the presence of excess weakly bound RBD molecules being removed as the buffer washed over the sensor surface. Therefore, with a single injection of $25 \mu\text{g/mL}$, complete coverage of the sensor surface was achieved, and this concentration of the RBD was used for subsequent analyses.

3.3.2.2 Monitoring aptamer interaction with RBD functionalized sensor

With the now optimized RBD functionalized sensor, the aptamers were screened to evaluate their interactions over the sensor surface. Using the streptavidin-biotin functionalized aptasensors (Chapter 2), kinetic evaluation of the RBD-aptamer interactions demonstrated higher binding affinity with the S1-T aptamer ($K_D = 5.94 \pm 9.7 \text{ nM}$) compared to the S1 aptamer ($K_D = 17.28 \pm 13.75 \text{ nM}$). Therefore, the S1 and S1-T aptamers were identified as suitable binding partners with the RBD protein and tested in this setup. Despite data from Chapter 2 suggesting RBD-aptamer binding on the surface, when this interaction was tested on the carboxyl surface, no binding was observed (Figure A3.5).

Similar to the blank buffer ($-26.20 \pm 7.0 \Delta\text{RU}$), the introduction of 100 nM S1 aptamer to the immobilized RBD exhibited a small negative shift in the baseline of $-47.50 \pm 10.9 \Delta\text{RU}$, indicating no protein-aptamer interactions. Furthermore, to test whether the binding was dependent on aptamer concentration, the aptamer was also introduced at 10x higher concentration (1 μM). However, no change in the LSPR signal was observed following the introduction of the S1 aptamer ($-39.80 \pm 4.1 \Delta\text{RU}$) (Figure A3.5). Since previous reports showed that the S1-T aptamer demonstrated higher affinity binding to the RBD, the S1-T aptamer was also screened at a higher concentration against the RBD functionalized carboxyl sensor. However, a negative signal drift ($-40.74 \pm 10.2 \Delta\text{RU}$) similar to the S1 aptamer signal was observed, suggesting no aptamer-protein binding. Overall, neither the S1 or S1-T aptamers exhibited binding to the RBD functionalized carboxyl surface likely due to inaccessibility of the binding sites in this configuration.^{164,185,186}

On the carboxyl sensor surface, the ligand was immobilized using covalent amide coupling chemistry. Though the use of the native ligand would be beneficial to reduce costs endured by chemical or genetic modifications, biosensors dependent on covalent immobilization of an unmodified ligand is then limited by the uncontrollable orientation of the ligand on the surface.^{5,149,151,167,187} Proteins generally have several primary amine groups at the N-terminal or on lysine residues.¹⁶⁸ When immobilizing proteins *via* amide coupling through their native primary amine groups, ensuring proper orientation of the ligand can be challenging. Therefore, depending on the conformation of the ligand on the surface, some binding sites required for analyte interaction may become inaccessible. Thus, despite the fact that the protein-aptamer complex is formed in other assays, reasons for the lack of binding on the protein functionalized carboxyl surface could be related to the

undesired random orientation of the ligands on the surface. For further evaluation of the RBD (Figure 3.10A) and aptamer binding interactions, molecular docking studies were performed (Figure 3.10). Using the MFold Software, the 2-dimensional (2D) structures of the S1 and S1-T aptamers were generated.¹⁸⁸ Then, RNAComposer was used to generate a 3D structure of the ssRNA sequence, which was then converted to the ssDNA tertiary structure of the S1 and S1-T aptamers (Figure 3.10B-C).^{144,145} Using the PatchDock Webservice, the RBD-aptamer complexes were generated, and the top docking solution was visualized using Discovery Studio Visualizer Software.^{138,139,144}

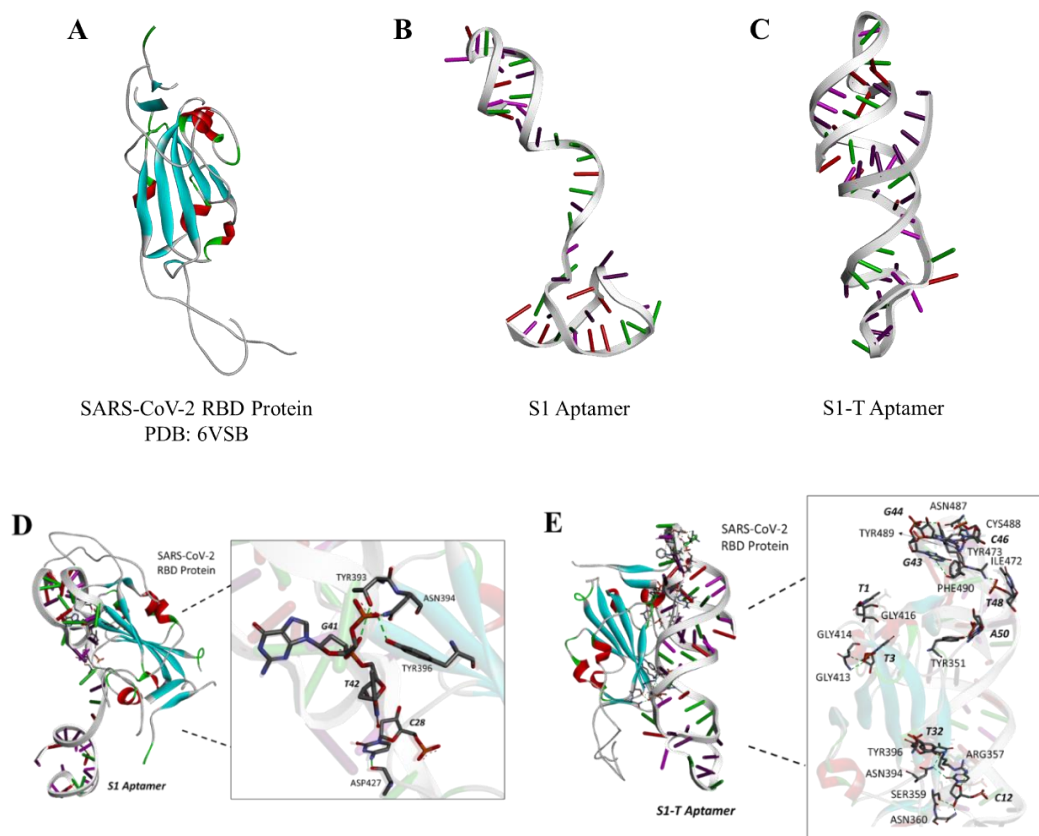


Figure 3.10. (A) Structure of the SARS-CoV-2 RBD protein (PDB ID: 6VSB); structure of protein subunits obtained using Discovery Studio Visualizer Software. Tertiary structures of the (B) S1 and (C) S1-T aptamers generated using RNAComposer.^{144,145} Molecular docking modelling of SARS-CoV-2 RBD protein and (D) S1 and (E) S1-T aptamer using PatchDock WebServer and visualized with Discovery Studio Visualizer Software.^{138,139,144}

The RBD (25.1 kDa) consists of 223 amino acids (Arg319-Phe541), with the predicted N-terminal located at Arg319.^{4,183} The predicted binding sites identified in Figures 3.10D-E represent hydrogen bonds formed between the amino acid residues of the RBD and the nucleotides of the S1 and S1-T aptamers. Based on the molecular docking

results, the amino acid residues participating in the RBD/S1 aptamer binding were Tyr393, Asn394, Tyr396 and Asp427 (Figure 3.10D). Similarly, for the RBD/S1-T aptamer interaction the Asn394 and Tyr396 also participate as binding sites, along with Tyr351, Arg357, Gly413, Ile472, Cys488, amongst others (Figure 3.10E). Therefore, in addition to the randomized orientation of the immobilized protein, it is possible that depending on the proximity of the N-terminal NH₂ group to the active protein-aptamer binding sites, the challenges with inaccessibility may also be related to the closeness of the sites to the NH₂ group bound to the sensor surface.

3.4 Conclusions

By exploiting different surface chemistries, an alternative LSPR aptasensor was developed as a model application for the rapid detection of the SARS-CoV-2. Using Au-thiol chemistry the fabrication of the S1 aptamer onto bare Au and carboxyl sensor surfaces for measurement by LSPR was explored. While aptamer attachment to the carboxyl surface was challenging, an Au-based aptasensor was developed and compared to the performance of the streptavidin-biotin based aptasensor (Chapter 2). The sensitivity of the optimized streptavidin-biotin aptasensor was superior to the current Au aptasensor. Additionally, the time required just for sensor fabrication is shorter and simpler for the streptavidin-biotin aptasensor (20-30 min) compared to the current Au aptasensor (>2 h). Though the sensitivity and fabrication time make the streptavidin-biotin aptasensor more attractive, it is important to recognize that the current Au aptasensor can be further optimized. Unexpectedly, aptamer-protein interactions were not observed using the optimized protein functionalized carboxyl sensor, despite previous evidence that there is strong binding even

in assays where one molecule is bound to the surface (Chapter 2). However, in Chapter 2, the sensor was functionalized with the aptamer, opposed to having a protein immobilized surface. This suggests that the order of the ligand and aptamer matters when studying binding interactions in surface dependent assays. Though aptamer interactions on the protein functionalized carboxyl surface could not be achieved, we were able to use the optimized RBD surface for other applications such as exploring protein-protein interactions, which is discussed in Chapter 4.

Chapter 4:

Assessing SARS-CoV-2 RBD-ACE2 interactions using a LSPR protein functionalized carboxyl sensor

4.1 Introduction

The knowledge gained from research conducted following the 2003 SARS outbreak has contributed tremendously to the understanding of the SARS-CoV-2. Though the last reported case of SARS-CoV was 2004, the continued research on the virus has been particularly useful in providing the insight needed to improve detection and treatment strategies against the novel SARS-CoV-2, and its variants.^{2,4,5,9,18,56,189-191}

The angiotensin converting enzyme 2 (ACE2) is expressed by almost all organs within the human body namely, the lungs, kidneys, intestines, skin, colon, amongst others.^{35,129,191} The ACE2 has been well studied and was identified as the host cell receptor responsible for SARS-CoV viral entry, thus facilitating human-to-human transmission.^{2,129,190-192} Specifically, the primary pathway of entry involved the direct attachment of the ACE2 with coronavirus receptor binding domain (RBD) located within the Spike (S) protein.^{5,9,30,191} Wu et al. (2020) reported that SARS-CoV strains with deletions at the positions 433-437 and 460-472 did not bind to the host cell receptor.²

Modeling of the RBD and ACE2 interactions then confirmed that these regions were important for direct interactions between the ACE2 and the coronavirus RBD. When comparing the nucleotide sequences of the SARS-CoV-2 genome to the SARS-CoV, the most conserved sequences across the coronaviruses were identified in the protein encoded by the S gene. Notably, similarities of approximately 76–78% is observed between the S proteins and 73–76% between the coronaviruses' RBD.^{2,4,9} Thus, the high similarities in amino acid sequences found with SARS-CoV made it an ideal model for understanding the properties and activity of the novel coronavirus. Specifically, since the ACE2 was known to facilitate the entry of the SARS-CoV and considering the highly conserved nature of the S protein, it was predicted that this host cell receptor may also participate in the infection mechanism of the SARS-CoV-2 – which has been confirmed.^{4,5,9,16,30} The SARS-CoV-2 RBD-ACE2 binding complex has been identified and the crystal structure is illustrated in Figure 4.1A.^{4,9} Additionally, several amino acid residues within the SARS-CoV-2 RBD have been associated with successful ACE2 binding. Some of the residues vital in ensuring strong ACE2-RBD binding include Gln493, Asn501, Leu455, Phe486, and Ser494.^{9,16} Compared to SARS-CoV ($K_D = 31$ nM), the binding affinity of SARS-CoV-2 RBD ($K_D = 4.7$ nM) with ACE2 is remarkably stronger as reported by surface plasmon resonance (SPR) measurements (Figure 4.1B).⁵

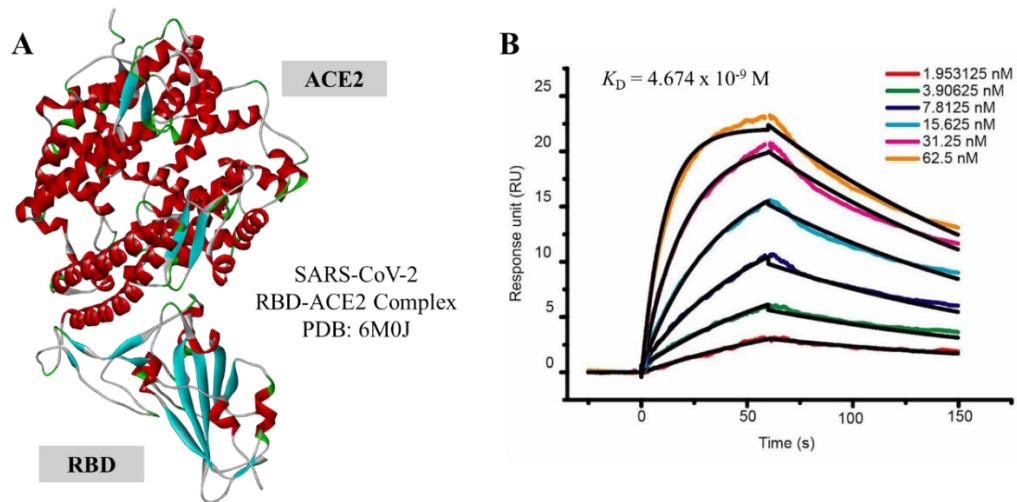


Figure 4.1. (A) Structure of the SARS-CoV-2 RBD bound to ACE2 (PDB: 6M0J). Fitted SPR sensorgrams representing (B) SARS-CoV-2 RBD binding to ACE2 surface and respective binding affinities; Figure (B) reproduced from Lan et al., (2020).⁴

Since ACE2 interactions play a key role in the virus' pathway into the body, understanding its interaction mechanisms is important – particularly for developing treatments, vaccines and potential cures for SARS-CoV-2 and other viruses that may later emerge. Besides the development of rapid detection methods for SARS-CoV-2, another strategy that has been explored for mitigating the impact of the virus is with the development of antiviral treatments. Learning from the SARS-CoV epidemic, treatment methods used at that time were also implemented for treatment of COVID-19. When demonstrating the participation of ACE2 as a point of entry for the SARS-CoV, Li et al., (2003) also proposed the use of small molecules, antibodies, and peptides for inhibition of the S-ACE2 interactions. For example, recently monoclonal antibodies Bamlanivimab plus etesevimab, bebtelovimab, casirivimab plus imdevimab, and sotrovimab were approved by the Food and Drug Administration (FDA) for use in the treatment of COVID-19.¹⁹³ The

active ingredients in prescribed medicine has also been identified as effective inhibitors of the S-ACE2 interactions, highlighting the great potential for the small molecules to be incorporated into drug therapies.^{169,194–196} Additionally therapeutic remedies involving peptides have been studied for their involvement in antiviral strategies.^{20,81,171} Another promising strategy involves the use of aptamers.^{83,87,89,95,197} Their small size, tunability and stability makes them ideal for application as drug targets.⁷⁶ For targeting other coronavirus related interactions, the inhibition of the RNA binding activity with the nucleocapsid (N) protein as the drug target, has also been proposed.¹⁹⁸

SPR techniques are ideal for label-free analysis of biomolecular interactions and have a long record of use in such applications.^{115,119,149} Particularly, for studying inhibitory interactions, covalent coupling methods are ideal to avoid rapid surface deterioration, leading to the underestimation of binding kinetics and affinity evaluations.^{5,167} When studying the potency of inhibitory reagents, such as peptides, antibodies or aptamers, the analysis of bio-affinity interactions is important. Therefore, for the best outcome, covalent coupling methods are more suitable.⁵

Herein, the protein functionalized surface optimized in Chapter 3 was used for further analysis of the ACE2 and RBD interactions. By monitoring the LSPR signals, an assay for the protein-protein interaction was developed on the carboxyl surface and regeneration conditions were optimized following successful RBD-ACE2 binding to allow for repetitive sample testing on the same surface. The RBD-ACE2 assay also demonstrated high binding affinity which is useful to ensure the high sensitivity of the sensor. The optimized protein-protein assay will be useful for future applications in the assessment of drug targets for the

treatment of COVID-19. Specifically, aptamers discussed in previous chapters, known to bind the RBD protein may be of value for assessing their inhibitory effects against the ACE2-RBD interaction.

4.2 Materials and Methods

4.2.1 Chemicals and reagents

Human ACE2 protein (cat: 10108-H08H) His-tagged recombinant protein and the SARS-CoV-2 Spike/RBD protein (cat: 40592-VNAH) were purchased from Sino Biological (Beijing, China). Bovine serum albumin (BSA) was acquired from Sigma Aldrich and used as a negative control analyte. Sodium chloride (BioShop), sodium phosphate dibasic (Westlab), potassium chloride (EMD Chemicals), potassium phosphate monobasic (MP Biomedicals), magnesium chloride (Caledon Laboratories), Tween20 (Fisher Bioreagents) were used to prepare the binding/running buffer. For testing regeneration conditions, glycine from Bio-Rad laboratories and hydrochloric acid (ACS grade, 36.5-38%) from VWR Chemicals were used. The carboxyl coated sensor and amine reagent kit containing carboxyl coated gold nanoparticle (AuNP) sensor chips, activation buffer, blocking solution, 1-Ethyl-3-(3-dimethylaminopropyl)carbodiimide (EDC) and N-Hydroxysuccinimide (NHS) was purchased from Nicoya LifeSciences.

4.2.2 LSPR measurements

Protein-protein interactions using the carboxyl chips were investigated using a LSPR instrument (OpenSPR, Nicoya Lifesciences, Canada), equipped with a 2-channel detection

system. All experiments were performed at 20 °C and using both channel 1 and 2 simultaneously as active channels. The binding/running buffer used with all experiments consisted of 136.8 mM NaCl, 10.1 mM Na₂HPO₄, 2.7 mM KCl, 1.8 mM KH₂PO₄, 0.55 mM MgCl₂, and 0.05% Tween20 (v/v).⁸⁸ The buffer was filtered with a 0.45 µm nylon syringe filter used for all dilutions, loop rinsing steps and dissociation phase. All measurements were performed in quadruplicate (N = 4) by acquiring data from both channel 1 and 2. The mean and standard deviation of these measurements were calculated and reported. For analyzing analyte interaction with the immobilized S1 aptamer, the signal difference (($I_f - I_i$) in ΔRU units) from the LSPR binding curves was calculated as the difference between the final LSPR signal (at 800 s, I_f) and the initial signal measured prior to protein injection.

4.2.3 Screening ACE2 interactions with a RBD functionalized carboxyl surface

From the stock 0.25 mg/mL ACE2 solution, 5.1 µL was added to 144.9 µL of the binding buffer to prepare a 100 nM ACE2 solution. After successful attachment of the RBD protein to the surface (chapter 3), an injection of 100 nM ACE2 protein (analyte) in the binding buffer was performed at a flow rate of 10 µL/min for a 10 min. interaction time. A dissociation time was allowed where the running buffer passed over the sensor surface for a minimum of 5-min following the completion of each injection. Following ACE2 binding, regeneration of the RBD functionalized surface was done using 5 mM HCl at a flow rate of 150 µL/min. The binding buffer free of any analyte was tested as a blank control. As the negative control analyte, a 1 mg/mL stock solution of the BSA protein in water was diluted

to 100 nM by addition of 1 μL of BSA to 149 μL binding buffer for measurement against the immobilized.

4.3 Results and discussion

4.3.1 Optimization of protein-protein regeneration conditions

To maximize the use of the sensor, the regeneration step was optimized following RBD-ACE2 binding to allow for multiple reuses of the sensor chip whilst maintaining the activity of the immobilized ligand. As illustrated in Figure 4.2A, the purpose of the regeneration step is to allow for complete removal of the bound ACE2 from the immobilized RBD, thus providing a fresh surface for subsequent sample injection to be performed.

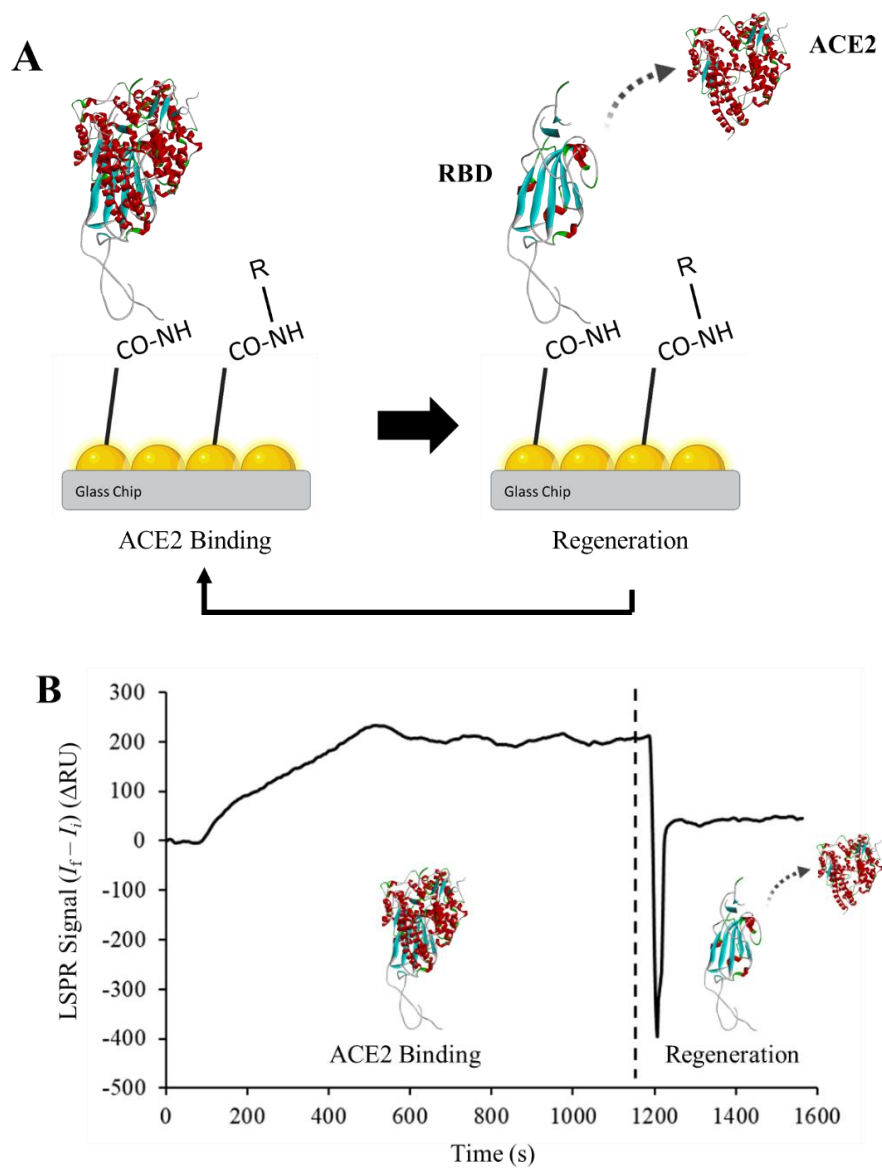


Figure 4.2. (A) Schematic illustration and (B) representative LSPR sensorgram demonstrating binding of the ACE2 protein to RBD functionalized sensor and (2) regeneration of the functionalized surface; [RBD] = 10 $\mu\text{g/mL}$; [ACE2] = 100 nM; [HCl] = 5 mM; flow rate for RBD immobilization (10 $\mu\text{L/min}$), ACE2 binding (10 $\mu\text{L/min}$), HCl regeneration (150 $\mu\text{L/min}$).

Optimal regeneration conditions were determined by testing various regeneration solutions and concentrations following RBD-ACE2 binding. The most appropriate regeneration agent would effectively provide complete dissociation of the analyte without damaging the immobilized ligand, however this is typically dependent on the type of surface and the stability of the ligand.^{134,167} For the regeneration step, solutions of glycine-HCl or HCl were injected at a flow rate of 150 $\mu\text{L}/\text{min}$.¹⁶⁷ A high flow rate was chosen as this allows for shorter interaction time with the surface and less opportunity for the regeneration molecule to cause damage or inactivation of the immobilized ligand. Additionally, based on reports where biomolecular interactions were studied on carboxyl-based surfaces, 10 mM glycine-HCl is a commonly used composition demonstrated to be an effective regeneration agent.^{167,199–203} Hence, it was tested as a potential solution for regeneration of the RBD-ACE2 assay. When the glycine-HCl solution was introduced, a significant and rapid decrease in the signal following regeneration, back to the original level (i.e., baseline) and decrease in binding with subsequent ACE2 injections were observed (Figure A4.1A-B). These trends suggested that the glycine-HCl solution was too harsh for regeneration of the RBD-ACE2 interaction and the glycine-HCl solution may have inactivated the sensor surface, thus resulting in irreproducible RBD-ACE2 binding events.²⁰² Therefore, further attempts at regeneration, using HCl, which is another commonly used reagent, were performed to identify whether it would effectively remove the bound protein from the surface without affecting the integrity of the sensor. Thus, the effects of various concentrations of HCl were tested and compared following successful ACE2 binding to immobilized RBD (Table 4.1).

Table 4.1. Results of regeneration using 1-10 mM HCl solutions after ACE2 binding to the immobilized RBD on the activated carboxyl surface.

HCl Concentration (mM)	%Regeneration Achieved		
	1st Injection	2nd Injection	3rd Injection
1	66.28 ± 13.1	99.44 ± 23.0	125.33 ± 23.0
2	55.51 ± 0.9	97.97 ± 3.0	139.69 ± 6.7
5	105.23 ± 11.5	N/A	N/A
10	241.38 ± 28.7	N/A	N/A

The recommended lower limit for the HCl regeneration solution has been reported as 10 mM.^{167,204} However, when 10 mM HCl was tested following RBD-ACE2 binding in this system, there was a significant decrease in the LSPR signal response of ~241%. The drastic decrease in the signal suggested an undesired loss of the ligand (RBD) activity and likely additional removal of non-specifically bound molecules. Consequently, following the initial regeneration step with 10 mM HCl, subsequent injections of ACE2 under similar conditions then produced lower binding with each regeneration performed. This decrease in ACE2 signals with increased use of the sensor further confirmed the loss of ligand activity and deterioration of the sensor performance with completion of each regeneration step. Compared to using the glycine-HCl composition, regeneration with HCl on its own did not completely deactivate the surface, as RBD-ACE2 binding was still achieved following the introduction of the regeneration solution. Therefore, though slow

deactivation of the immobilized RBD surface was observed with the high HCl concentration, it was still able to remove the bound ACE2 without fully disabling the sensor. Thus, lower concentrations (1, 2 and 5 mM HCl) were tested to determine the more ideal conditions to be used as the regeneration agent. When 1 and 2 mM HCl were used, sufficient (>90%) surface regeneration was achieved after two sequential injections. In both cases, following with a third injection of HCl depleted the signal >120% indicating analyte removal and potential loss of some ligand activity. Sufficient regeneration was achieved with two injections of 1 or 2 mM HCl, however, to simplify the regeneration protocol using a single injection of the reagent, the solution concentration was increased to 5 mM. When 5 mM HCl was tested, ~105% decrease in the LSPR signal was observed after just one injection. Notably, reproducible ACE2 signals were also achieved when 5 mM HCl injections were performed for regeneration. Therefore, 5 mM HCl was used for regeneration of the RBD-ACE2 interaction for subsequent experiments.

4.3.2 Evaluation of ACE2 protein with RBD functionalized surface

Using the optimized protein functionalized carboxyl sensor (Chapter 3), and regeneration protocols, RBD-ACE2 binding was evaluated. When the ACE2 was introduced to the optimized RBD sensor, the final change in the LSPR signal produced was $161.48 \pm 14.2 \Delta\text{RU}$ (Figure 4.3). Screening of negative control analytes and the blank buffer were also evaluated to discern and differentiate any non-specific binding or background interferences. The BSA (negative control analyte) and the blank buffer were introduced to the immobilized RBD under the same conditions as tested with ACE2. BSA showed no interactions with the immobilized RBD, as there was just a small negative drift

in the LSPR signal ($-33.93 \pm 25.9 \Delta\text{RU}$), similar to what is achieved when no analyte ($-26.20 \pm 7.0 \Delta\text{RU}$) is present (Figure 4.3B). Therefore, an RBD-ACE2 assay was successfully developed based on ACE2 interactions with immobilized RBD on an activated carboxyl surface.

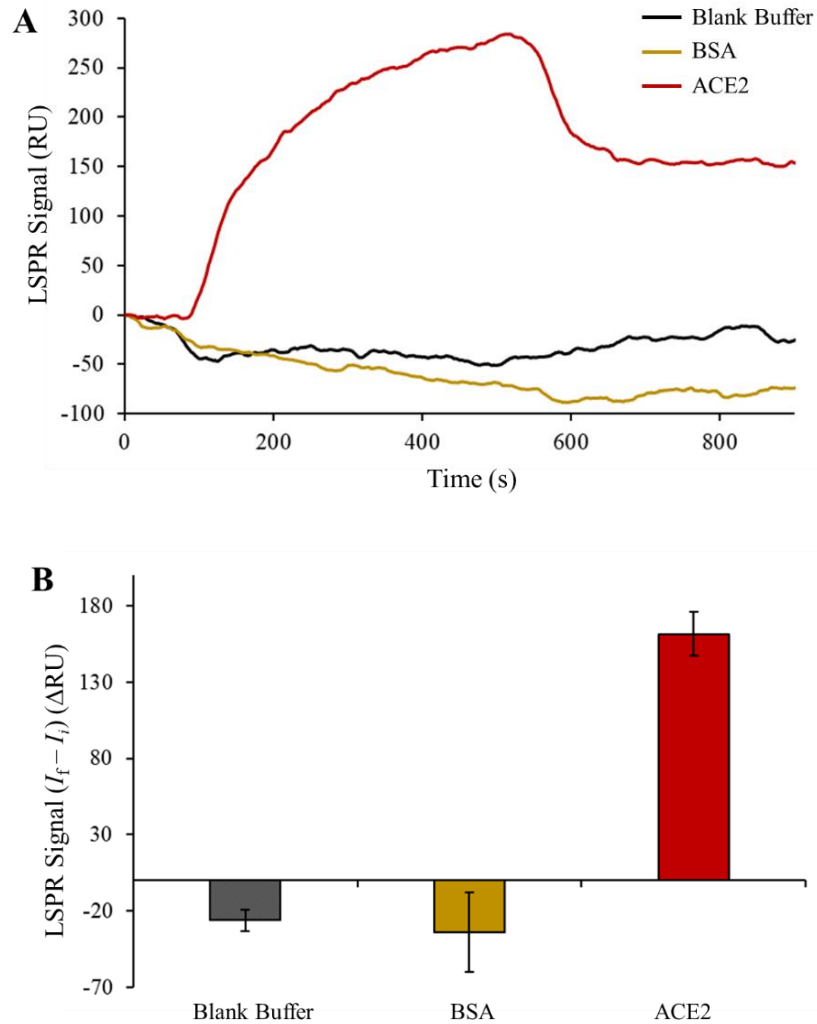


Figure 4.3. (A) Representative LSPR signals and (B) plot of LSPR signal comparison with blank buffer, BSA and ACE2 using the RBD functionalized carboxyl/AuNP surface; immobilized [RBD] = 25 $\mu\text{g/mL}$; [BSA and ACE2] = 100 nM; flow rate = 10 $\mu\text{L/min}$; regeneration of RBD-ACE2 interaction with 10 mM HCl, flow rate = 150 $\mu\text{L/min}$.

The binding kinetics of the RBD-ACE2 interaction was further investigated and determined using a 1:1 binding model with the TraceDrawer software (Figure A4.2). The on-rate (k_a) corresponding to the RBD-ACE2 interaction was $3.12 \times 10^4 \text{ M}^{-1} \text{ s}^{-1}$, and the off-rate (k_d) was $5.12 \times 10^{-4} \text{ s}^{-1}$. The calculated K_D was 16.4 nM which is comparable to the previously reported K_D value by Laffeber et al., (2021) for the RBD-ACE2 interaction (17 nM).²⁰⁵ K_D values of 74 nM, 3 nM, 20 nM and 44 nM have also been reported by Barton et al., (2021), Nguyen et al., (2020), Mei et al., (2021) and Shang et al., (2020), respectively.^{5,16,195,206} Based on the wide range of binding affinities reported, it is evident that the reported binding kinetics can vary. The values obtained differ primarily because they depend greatly on the experimental approaches used. For example, when a His-tagged, biotinylated RBD was immobilized on the streptavidin surface, the K_D value was 20 nM, however when a His-tagged RBD was attached to a carboxyl surface through amide coupling, the K_D was 44 nM.^{5,195} Factors that can influence results include (i) the type of protein(s) used – whether expressed from human cells or recombinant protein, it was chemically tagged, or it is a particular domain of or the full target molecule (e.g., S vs. RBD); (ii) which protein is attached to the surface measured; and (iii) the analytical technique used.^{4,5,16} In a comparison to other approaches, Shang et al., (2020) highlighted that covalent immobilization *via* amide coupling yields better affinities since the dissociation of the ligand is less likely than non-covalent methods.⁵ On the other hand, due to disorientation of the surface which is commonly observed with covalent attached proteins, the affinity can be underestimated when the target analyte fails to bind as a result of inaccessible binding sites. Additionally, other reports have demonstrated that SARS-CoV RBD functionalization achieved stronger ACE2-RBD binding compared to surfaces

functionalized with ACE2.^{5,190} Therefore, using our RBD-ACE2 assay design on the activated carboxyl surface provides several advantages over other approaches including higher binding affinity.

4.3.3 Effects of surface coverage on ACE2 binding to the RBD functionalized surface

The importance of the ligand immobilization level on analyte binding was also evaluated using the RBD functionalized carboxyl/AuNP sensor. Fundamentally, the amount of analyte binding observed is directly related to the amount of ligand present for the interaction to occur. When the coverage is low (i.e., low ligand immobilization level), there is not enough of the ligand available for binding of the analyte, thus the signal change is not observed or is minimal.^{84,142,173,207} Analyte binding is more likely with a higher surface coverage and limited steric hindrance. For this reason, the fabrication of biosensors should be optimized to achieve the greatest surface coverage by the ligand possible without affecting analyte binding.^{25,84,207}

In Chapter 3, the immobilization levels, which represented the surface coverage attained using RBD concentrations 1–50 $\mu\text{g/mL}$ was discussed. ACE2 binding to the RBD surface was then assessed as a function of RBD concentration (i.e., surface coverage) (Figure 4.4). Using 1 $\mu\text{g/mL}$ RBD for fabrication yielded a low immobilization level that signified no protein binding to the surface. Subsequently, the inherent lack of RBD immobilization resulted in unsuccessful ACE2 binding. The introduction of RBD at a concentration of 10 $\mu\text{g/mL}$ produced an immobilization level of $825.23 \pm 111.9 \Delta\text{RU}$, suggesting that some surface coverage was achieved. However, when the ACE2 was

introduced, no binding was achieved ($1.31 \pm 0.6 \Delta\text{RU}$). Therefore, though some RBD was attached to the surface, it was evident that the immobilization level achieved was not sufficient for ACE2 binding to occur and greater RBD coverage was needed to monitor the binding.

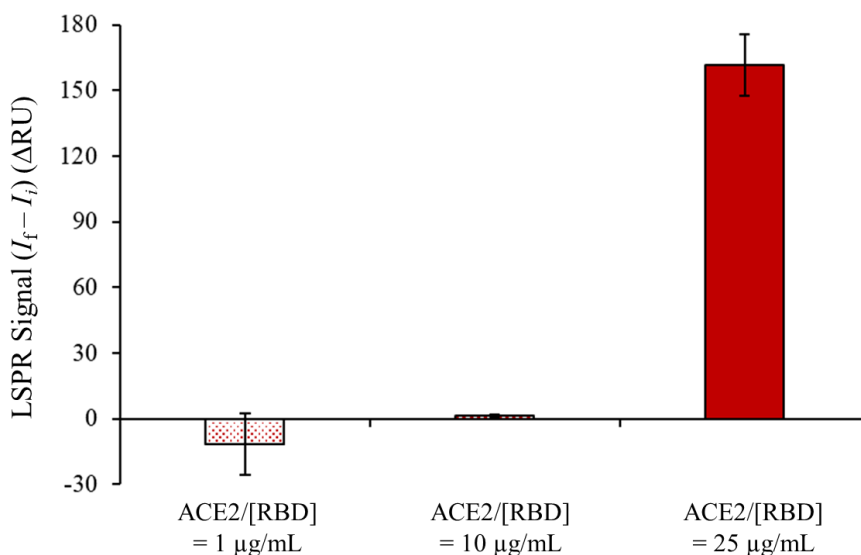


Figure 4.4. Comparison of LSPR signals of ACE2 binding as a function of RBD loading during the immobilization step; [RBD] = 1, 10, or 25 $\mu\text{g/mL}$, [ACE2] = 100 nM; flow rate = 10 $\mu\text{L/min}$; regeneration with 10 mM HCl, flow rate = 150 $\mu\text{L/min}$.

The greatest ACE2 signal was observed when the RBD immobilization level was increased to $2098.53 \pm 120.5 \Delta\text{RU}$ (25 $\mu\text{g/mL}$), which was under the conditions that also gave the best surface coverage. The notable and significant increase in the LSPR signal suggested optimal RBD coverage capable of detecting RBD–ACE2 binding. Increasing the RBD concentration to 50 $\mu\text{g/mL}$ did not improve the surface coverage achieved (Chapter 3), therefore its effect on surface coverage was not compared. Overall, the data emphasized the importance of appropriate surface coverage for determining ligand-analyte interactions

by LSPR. Though some ligand attachment can be achieved at suboptimal concentrations, measurable analyte interactions may not be achieved until complete saturation of the surface is reached, which further improves the sensitivity of the sensor.

4.4 Significance and future applications

Understanding the ACE2-RBD interaction is important for improving the knowledge on SARS-CoV-2 infections and corresponding treatment methods. The establishment of a protein-protein assay such as this RBD-ACE2 LSPR assay is a viable approach toward the next step for analysis of antiviral treatments. For example, by monitoring how inhibitory reagents, such as small molecules, peptides, or aptamers interact as blockers of the RBD-ACE2 interaction, effective therapeutic strategies against COVID-19 can be created (Figure 4.5).

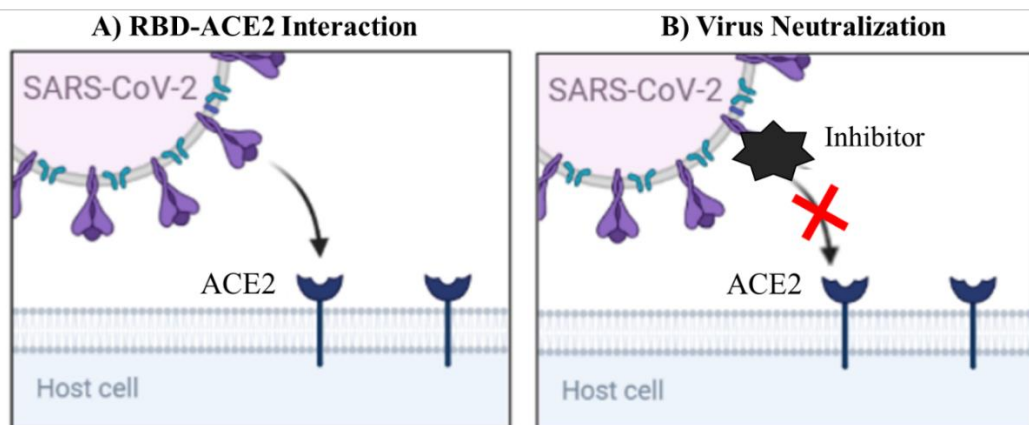


Figure 4.5. Illustration of protein-protein interaction system showing the mechanism of virus neutralization. Created using Biorender.com.

Recently, some active ingredients from traditional Chinese medicine have been explored as possible targets to be incorporated in treatment strategies for COVID-19 and

to understand their interaction mechanisms.^{169,195} For example, *Ephedra sinica*, primarily used for treating respiratory related illnesses such as asthma, bronchitis, and others, was tested as a promising inhibitor of the S-ACE2 interactions.¹⁹⁵ Mei et al., (2021) found that quinoline-2-carboxylic acids were the active ingredients in *Ephedra sinica* extracts that induced the inhibition of RBD-ACE2 interactions. In this pathway, the amidogen and carboxyl group of the quinoline-2-carboxylic acids bind directly to the SARS-CoV-2 RBD, primarily with Tyr449 and Gln498. These sites also play a role in the RBD-ACE2 interactions.⁴ The inhibitory effects of other small molecules such as quercetin, puerarin, corilagin, geraniin, glycyrrhizic acid, amongst other active compounds found in Chinese herbal medicines have been studied as well.^{169,196,208}

Aptamers can also play a role as inhibitors of the S-ACE2 interaction. The small size of aptamers (2-3 nm) also serves as an advantage over traditional treatments that utilize antibodies (>10 nm).⁸⁹ Specifically, considering the respiratory nature of the virus, the size of aptamers make them more suitable for use in treatments that require passage through intranasal or pulmonary pathways. In light of the growing need for effective treatment against viral infections, recent studies have demonstrated the use of aptamers as specific and selective strategies for neutralization of the coronavirus. The potency of various aptamers designed specifically to target the SARS-CoV-2 S or RBD protein have been tested.^{83,89,91,209} Therefore, with the knowledge that the aptamers explored in Chapters 2 and 3, binds to the SARS-CoV-2 S1 and RBD proteins, they can likely act as an inhibitor of the S-ACE2 interaction which would be useful for the development of treatments. However, further experimental studies are needed to confirm their potency.

4.5 Conclusion

Binding of the RBD and ACE2 proteins is a key step in initiating the entry of the coronavirus into the host cell. Thus, in addition to the development of biosensing techniques for the SARS-CoV-2, further understanding of coronavirus related interactions within the body is important.

Using the optimized protein functionalized surface, a protein-protein assay was developed. The RBD immobilized through amide coupling on a carboxyl LSPR sensor demonstrated high affinity association with the ACE2, that was comparable to other K_D values reported. Overall, a wide range of K_D values for the RBD-ACE2 interaction have been reported. However, some key experimental factors can affect the outcomes of the calculated values and lead to contradicting results. Additionally, the effect of the ligand surface coverage on analyte binding was also discussed. Suboptimal RBD immobilization levels, though showing evidence of ligand attachment, were not sufficient for proper ACE2 binding. Thus, in this work we demonstrated the importance of surface optimization, showing that optimal surface coverage is required for appropriate assessment of the protein-protein interaction. Aside from the analysis of RBD-ACE2 interactions, the application of this LSPR sensor can be extended to experimental analysis of therapeutic strategies for COVID-19. The current sensor has been developed for future applications whereby the inhibitory effect of small molecules, peptides, and aptamers can be screened to evaluate their ability to act as antiviral targets against the SARS-CoV-2 or other viral targets.

Chapter 5:

Summary and Future Work

5.1 Summary

The sudden emergence of the coronavirus 2019 (COVID-19) pandemic created many challenges within the health care system. Timely mitigation of the coronavirus was a priority but was challenging to achieve considering the rapid global spread of the disease within a short time. As a solution, researchers have sought to develop rapid detection and treatment strategies for the severe acute respiratory syndrome beta-coronavirus 2 (SARS-CoV-2). During the pandemic, conventional diagnostic methods such as nucleic acid-based tests using polymerase chain reaction (PCR) based methods or serological immunoassays were heavily relied upon for the confirmed diagnosis of COVID-19. However, these methods tend to be time consuming, expensive and/or exhibit low reliability with high false negative rates. Thus, as an alternative to these methods, biosensors were developed as they are generally cost effective, rapid, and sensitive.

In this thesis, we demonstrated the development of biosensors capable of selective and sensitive detection of the SARS-CoV-2 Spike (S) protein. Our biosensor used a S1 aptamer as the bioreceptor for determination of the S1 protein target with an optical transducer based on localized surface plasmon resonance (LSPR) technology. The main advantages of using LSPR, such as low sample consumption, simplified sample preparation and sensor fabrication, rapid acquisition of results, high sensitivity, ease-of-

use, and good reusability, have all been exhibited by the aptasensor. Notably, some features of the OpenSPR detection system used, including the ability to only run one sample at a time and its high maintenance, limits its utilization in point-of-care (POC) diagnostics. However, in this case, the OpenSPR instrument used was suitable for the purpose of completing the first phase in the development of the LSPR sensing mechanism. Other available automated, high throughput LSPR instrumentation capable of multi-sample testing such as OpenSPR-XT (NicoyaLife Sciences) also operates using the same technology as the OpenSPR but may be better suited for POC testing and bedside monitoring of in-patient care.

The first phase of biosensor development toward its application in POC diagnostics and commercialization, involved demonstrating the excellent performance of the aptamer-protein interactions. As a proof-of-concept of this sensing mechanism using LSPR, the aptasensors were fabricated on streptavidin-biotin (Chapter 2) or bare gold (Au) (Chapter 3) sensor surfaces. The capture and covalent coupling methods of fabrication were compared to determine which would produce the best performance. With the current aptamer functionalized systems, the sensitivity of the sensor was greatest using the surface based on biotin-streptavidin capture coupling. However, with further optimization of the Au-thiol covalent coupling method, there is still potential for it to be improved and equally become a highly sensitive biosensor. Using the streptavidin-biotin aptasensor, further assessment of the aptamer-protein interactions was studied, including kinetic and affinity parameters, which revealed strong binding affinity between the S1 aptamer and S1 protein. Additionally, ready-to-use aptasensors were fabricated offline and their performance was compared to the aptasensors fabricated *via* online methods. The ready-to-use aptasensor

demonstrated excellent stability and shelf-life up to at least 24 days post fabrication and storage in 4-8 °C. The regeneration procedure was also optimized for the streptavidin-biotin aptasensor, to allow for multiple samples to be tested using a single sensor chip. Appropriate regeneration of the aptasensor is valuable to ensure that the integrity of the surface remains with continued use of the biosensor. The streptavidin-biotin aptasensor exhibited good repeatability with a minimum of 9 sample injections. Furthermore, when the S1 aptasensor was tested with spiked artificial saliva and serum albumin samples, >90% recovery was achieved, which is promising for the future application of the LSPR aptasensor with real, clinical samples. Moreover, the S1 aptasensor was able to distinguish the SARS-CoV-2 S1 protein apart from the SARS-CoV S1 protein, which demonstrated lower binding affinity.

Utilization of covalent amide coupling methods for aptamer functionalized carboxyl coated sensors was not achieved. However, in an alternative attempt to test protein-aptamer interactions, protein functionalized surfaces were fabricated on the carboxyl surface. However, when the aptamers were screened over the protein surface, the expected binding of the two molecules was not observed. These results highlighted the importance of choosing the most optimal designs when studying biomolecular interactions, as different configurations of the sensor design may yield different results. The protein functionalized surface was also used to test the important protein-protein interactions between the SARS-CoV-2 receptor binding domain (RBD) and the angiotensin converting enzyme 2 (ACE2) which play a role in the coronavirus' entry into the human cell. The assay was optimized to test RBD-ACE2 interactions, which can then be utilized as a

platform for studying the effects of therapeutic remedies, including aptamers that can function as inhibitors of the protein-protein interaction.

Overall, in this thesis, the three main objectives were addressed with the aim of developing alternative detection strategies toward the mitigation of COVID-19. Two aptasensors were developed based on different fabrication methods/surface chemistries. We have also developed an optimized platform for studying protein-protein interactions that can be used further for assessing the effects of potential drug therapies for COVID-19 and other viruses that may emerge. However, in order to achieve the next phase of biosensor development, better sensitivity of the current sensors should be considered.

5.2 Future Work

Considering the great promise demonstrated by the streptavidin-biotin and bare Au aptasensors, further optimization of the sensors would be beneficial toward the advancement of the LSPR biosensor. We have demonstrated that the streptavidin-biotin aptasensor can be fabricated offline as ready-to-use sensors, while maintaining excellent shelf life, reusability, and stability. However, to get to the stage of commercialization of the sensor, they should be able to detect physiologically relevant amounts of the virus, which the current sensor cannot achieve. Thus, further optimization of the biotin-streptavidin sensor would be required. One way of improving the sensitivity of the sensor would be to develop a sandwich assay using signal amplifiers such as SARS-CoV-2 anti-S1 peptide, antibody, or secondary aptamer. The sensitivity of the bare Au sensors can also be improved with further optimization of the fabrication procedure. For example, testing various cystamine:aptamer ratios and longer cleaning times can help to improve the

sensor's performance. Also, taking advantage of the excellent performance displayed by the streptavidin-biotin sensors and considering the well-known stability and high sensitivity of covalent based sensors, another surface chemistry using a Au-carboxyl-biotin-streptavidin surface can also be compared.

Furthermore, with the rapid evolution of the SARS-CoV-2 into several highly transmissible and lethal variants, sensitive detection strategies capable of detecting the parent virus and its variants should also be available. In this case, the ideal biosensor would be able to simultaneously detect all variants of the SARS-CoV-2 and its wildtype while maintaining good sensitivity. Thus, using the best optimized S1 aptasensor, it would be worth assessing its ability to detect other coronavirus variants of concern (VOCs), such as the Alpha, Beta, Gamma, Delta, and Omicron. Though not being able to differentiate the specific variant using LSPR, being able to detect the SARS-CoV-2 wildtype as well as the VOCs in one sensor, would add significant value to the technique. However, to account for the limitation in lack of structural data attained by LSPR methods, future improvements to the detection system can include the addition of techniques such as mass spectrometry to work in tandem with LSPR. This would create a unique approach for users to have real-time qualitative and quantitative information provided.

The optimized RBD functionalized carboxyl sensor has demonstrated high binding affinity and detection of the ACE2 protein. In future studies, the protein surface can also be used for studying the effects of inhibitory molecules that target the RBD-ACE2 interaction. For example, the S1 or S1-T aptamers, which have been shown to bind the RBD protein (Chapter 2), can be used as an inhibitor for application in therapeutics. With

the RBD immobilized on the surface, blocking of its interaction with the ACE2 can be studied with the introduction of an aptamer. Specifically, since the binding affinity of the RBD-S1-T aptamer (5.94 nM) interaction is stronger than the RBD-ACE2 (16.4 nM) interaction, it is expected that the aptamer will outcompete RBD-ACE2 binding. However, considering the data revealed in Chapter 3, the aptamer does not interact with the immobilized surface. Therefore, in order to continue with testing on the carboxyl surface, further amendments to the sensor design may be required. For instance, to eliminate inaccessibility issues, anti-RBD peptide or antibody functionalized surfaces can be developed, to extend the proximity of the RBD protein from the sensor surface. In this way, the stability and high sensitivity known to be exhibited by carboxyl sensors can still be taken advantage of. Another approach may be to use an alternative sensor surface, such as streptavidin-biotin for the immobilization of biotinylated RBD proteins. The use of this strategy would promote organized orientation of the ligand on the sensor surface, thus avoiding challenges of inaccessible binding sites derived from the random orientation of the immobilized ligand as seen when using the carboxyl surfaces (Chapter 3). The RBD sensor can also be used to examine the potency of other inhibitors such as small molecules, peptides, or antibodies.

References

- (1) Ravi, N.; Cortade, D. L.; Ng, E.; Wang, S. X. Diagnostics for SARS-CoV-2 Detection: A Comprehensive Review of the FDA-EUA COVID-19 Testing Landscape. *Biosens. Bioelectron.* **2020**, *165*, 112454. <https://doi.org/10.1016/j.bios.2020.112454>.
- (2) Wu, F.; Zhao, S.; Yu, B.; Chen, Y. M.; Wang, W.; Song, Z. G.; Hu, Y.; Tao, Z. W.; Tian, J. H.; Pei, Y. Y.; Yuan, M. L.; Zhang, Y. L.; Dai, F. H.; Liu, Y.; Wang, Q. M.; Zheng, J. J.; Xu, L.; Holmes, E. C.; Zhang, Y. Z. A New Coronavirus Associated with Human Respiratory Disease in China. *Nature* **2020**, *579* (7798), 265–269. <https://doi.org/10.1038/s41586-020-2008-3>.
- (3) Rabaan, A. A.; Al-ahmed, S. H.; Haque, S.; Sah, R.; Tiwari, R. SARS-CoV-2, SARS-CoV, and MERS-CoV: A Comparative Overview. *Le Infez. Med.* **2020**, *2*, 174–184.
- (4) Lan, J.; Ge, J.; Yu, J.; Shan, S.; Zhou, H.; Fan, S.; Zhang, Q.; Shi, X.; Wang, Q.; Zhang, L.; Wang, X. Structure of the SARS-CoV-2 Spike Receptor-Binding Domain Bound to the ACE2 Receptor. *Nature* **2020**, *581* (7807), 215–220. <https://doi.org/10.1038/s41586-020-2180-5>.
- (5) Shang, J.; Ye, G.; Shi, K.; Wan, Y.; Luo, C.; Aihara, H.; Geng, Q.; Auerbach, A.; Li, F. Structural Basis of Receptor Recognition by SARS-CoV-2. *Nature* **2020**, *581* (7807), 221–224. <https://doi.org/10.1038/s41586-020-2179-y>.
- (6) Taylor, D. B. A Timeline of the Coronavirus Pandemic <https://www.nytimes.com/article/coronavirus-timeline.html> (accessed Jun 8, 2022).
- (7) Elflein, J. New cases of COVID-19 worldwide from January 23, 2020 to May 31, 2022, by day <https://www.statista.com/statistics/1103040/cumulative-coronavirus-covid19-cases-number-worldwide-by-day/> (accessed Jun 1, 2022).
- (8) COVID-19 Coronavirus Pandemic <https://www.worldometers.info/coronavirus/> (accessed Jun 1, 2022).
- (9) Wan, Y.; Shang, J.; Graham, R.; Baric, R. S.; Li, F. Receptor Recognition by the Novel Coronavirus from Wuhan: An Analysis Based on Decade-Long Structural Studies of SARS Coronavirus. *J. Virol.* **2020**, *94* (7). <https://doi.org/10.1128/jvi.00127-20>.
- (10) Singh, N. K.; Ray, P.; Carlin, A. F.; Magallanes, C.; Morgan, S. C.; Laurent, L. C.; Aronoff-Spencer, E. S.; Hall, D. A. Hitting the Diagnostic Sweet Spot: Point-of-Care SARS-CoV-2 Salivary Antigen Testing with an off-the-Shelf Glucometer. *Biosens. Bioelectron.* **2021**, *180*, 113111. <https://doi.org/10.1016/j.bios.2021.113111>.

- (11) Chen, Z.; Wu, Q.; Chen, J.; Ni, X.; Dai, J. A DNA Aptamer Based Method for Detection of SARS-CoV-2 Nucleocapsid Protein. *Viol. Sin.* **2020**, *35* (3), 351–354. <https://doi.org/10.1007/s12250-020-00236-z>.
- (12) Farrow, T.; Laumier, S.; Hall, S.; Sandall, I.; Zalinge, H. Van. Feasibility of a Silicon Thin Film Transistor-Based Aptamer Sensor for COVID-19 Detection. *IEEE Sens. J.* 1–5.
- (13) Grifoni, A.; Sidney, J.; Zhang, Y.; Scheuermann, R. H.; Peters, B.; Sette, A. A Sequence Homology and Bioinformatic Approach Can Predict Candidate Targets for Immune Responses to SARS-CoV-2. *Cell Host Microbe* **2020**, *27* (4), 671–680.e2. <https://doi.org/10.1016/j.chom.2020.03.002>.
- (14) Lee, C. Y. P.; Lin, R. T. P.; Renia, L.; Ng, L. F. P. Serological Approaches for COVID-19: Epidemiologic Perspective on Surveillance and Control. *Front. Immunol.* **2020**, *11*, 1–7. <https://doi.org/10.3389/fimmu.2020.00879>.
- (15) Fani, M.; Zandi, M.; Soltani, S.; Abbasi, S. Future Developments in Biosensors for Field-Ready SARS-CoV-2 Virus Diagnostics. *Biotechnol. Appl. Biochem.* **2021**, *68* (4), 695–699. <https://doi.org/10.1002/bab.2033>.
- (16) Nguyen, H.; Lan, P. D.; Thai, N. Q.; Nissley, D. A.; O'Brien, E. P.; Li, M. S. Does SARS-CoV-2 Bind to Human ACE2 More Strongly Than Does SARS-CoV? *J. Phys. Chem. B* **2020**, *124* (34), 7336–7347. <https://doi.org/10.1021/acs.jpcc.0c04511>.
- (17) Wang, Q.; Zhang, Y.; Wu, L.; Niu, S.; Song, C.; Zhang, Z.; Lu, G.; Qiao, C.; Hu, Y.; Yuen, K. Y.; Wang, Q.; Zhou, H.; Yan, J.; Qi, J. Structural and Functional Basis of SARS-CoV-2 Entry by Using Human ACE2. *Cell* **2020**, *181* (4), 894–904.e9. <https://doi.org/10.1016/j.cell.2020.03.045>.
- (18) Glowacka, I.; Bertram, S.; Müller, M. A.; Allen, P.; Soilleux, E.; Pfefferle, S.; Steffen, I.; Tsegaye, T. S.; He, Y.; Gnirss, K.; Niemeyer, D.; Schneider, H.; Drosten, C.; Pöhlmann, S. Evidence That TMPRSS2 Activates the Severe Acute Respiratory Syndrome Coronavirus Spike Protein for Membrane Fusion and Reduces Viral Control by the Humoral Immune Response. *J. Virol.* **2011**, *85* (9), 4122–4134. <https://doi.org/10.1128/jvi.02232-10>.
- (19) Tai, W.; He, L.; Zhang, X.; Pu, J.; Voronin, D.; Jiang, S.; Zhou, Y.; Du, L. Characterization of the Receptor-Binding Domain (RBD) of 2019 Novel Coronavirus: Implication for Development of RBD Protein as a Viral Attachment Inhibitor and Vaccine. *Cell. Mol. Immunol.* **2020**, *17* (6), 613–620. <https://doi.org/10.1038/s41423-020-0400-4>.
- (20) Yan, J.; Petitjean, S. J. L.; Koehler, M.; Zhang, Q.; Dumitru, A. C.; Chen, W.; Derclaye, S.; Vincent, S. P.; Soumillion, P.; Alsteens, D. Molecular Interaction and Inhibition of SARS-CoV-2 Binding to the ACE2 Receptor. *Nat. Commun.* **2020**, *11*.
- (21) Arya, R.; Kumari, S.; Pandey, B.; Mistry, H.; Bihani, S. C.; Das, A.; Prasher, V.;

- Gupta, G. D.; Panicker, L.; Kumar, M. Structural Insights into SARS-CoV-2 Protein. *J. Mol. Biol.* **2021**, *433* (January), 166725. <https://doi.org/10.1016/j.jmb.2020.11.024>.
- (22) Han, P.; Li, L.; Liu, S.; Wang, Q.; Zhang, D.; Xu, Z.; Han, P.; Li, X.; Peng, Q.; Su, C.; Huang, B.; Li, D.; Zhang, R.; Tian, M.; Fu, L.; Gao, Y.; Zhao, X.; Liu, K.; Qi, J.; Gao, G. F.; Wang, P. Receptor Binding and Complex Structures of Human ACE2 to Spike RBD from Omicron and Delta SARS-CoV-2. *Cell* **2022**, *185* (4), 630-640.e10. <https://doi.org/10.1016/j.cell.2022.01.001>.
- (23) Valero, J.; Civit, L.; Dupont, D. M.; Selnihhin, D.; Reinert, L. S.; Idorn, M.; Israels, B. A.; Bednarz, A. M.; Bus, C.; Asbach, B.; Peterhoff, D.; Pedersen, F. S.; Birkedal, V.; Wagner, R.; Paludan, S. R.; Kjems, J. A Serum-Stable RNA Aptamer Specific for SARS-CoV-2 Neutralizes Viral Entry. *Proc. Natl. Acad. Sci. U. S. A.* **2021**, *118* (50), 1–10. <https://doi.org/10.1073/pnas.2112942118>.
- (24) Park, S.; Kim, H.; Woo, K.; Kim, J. M.; Jo, H. J.; Jeong, Y.; Lee, K. H. SARS-CoV-2 Variant Screening Using a Virus-Receptor-Based Electrical Biosensor. *Nano Lett.* **2022**, *22* (1), 50–57. <https://doi.org/10.1021/acs.nanolett.1c03108>.
- (25) Fathi Karkan, S.; Maleki Baladi, R.; Shahgolzari, M.; Gholizadeh, M.; Shayegh, F.; Arashkia, A. The Evolving Direct and Indirect Platforms for the Detection of SARS-CoV-2. *J. Virol. Methods* **2022**, *300*, 114381. <https://doi.org/10.1016/j.jviromet.2021.114381>.
- (26) Lisboa Bastos, M.; Tavaziva, G.; Abidi, S. K.; Campbell, J. R.; Haraoui, L. P.; Johnston, J. C.; Lan, Z.; Law, S.; MacLean, E.; Trajman, A.; Menzies, D.; Benedetti, A.; Khan, F. A. Diagnostic Accuracy of Serological Tests for Covid-19: Systematic Review and Meta-Analysis. *BMJ* **2020**, *370*. <https://doi.org/10.1136/bmj.m2516>.
- (27) Benameur, N.; Mahmoudi, R.; Zaid, S.; Arous, Y.; Hmida, B.; Bedoui, M. H. SARS-CoV-2 Diagnosis Using Medical Imaging Techniques and Artificial Intelligence: A Review. *Clin. Imaging* **2021**, *76*, 6–14. <https://doi.org/10.1016/j.clinimag.2021.01.019>.
- (28) Oishee, M. J.; Ali, T.; Jahan, N.; Khandker, S. S.; Haq, M. A.; Khondoker, M. U.; Sil, B. K.; Lugova, H.; Krishnapillai, A.; Abubakar, A. R.; Kumar, S.; Haque, M.; Jamiruddin, M. R.; Adnan, N. Covid-19 Pandemic: Review of Contemporary and Forthcoming Detection Tools. *Infect. Drug Resist.* **2021**, *14*, 1049–1082. <https://doi.org/10.2147/IDR.S289629>.
- (29) Hodinka, R. L.; Kaiser, L. Is the Era of Viral Culture over in the Clinical Microbiology Laboratory? *J. Clin. Microbiol.* **2013**, *51* (1), 2–8. <https://doi.org/10.1128/JCM.02593-12>.
- (30) Safiabadi Tali, S. H.; LeBlanc, J. J.; Sadiq, Z.; Oyewunmi, O. D.; Camargo, C.; Nikpour, B.; Armanfard, N.; Sagan, S. M.; Jahanshahi-Anbuhi, S. Tools and Techniques for Severe Acute Respiratory Syndrome. *Clin. Microbiol. Rev.* **2021**, *34* (3). <https://doi.org/https://doi.org/10.1128/CMR.00228-20>.

- (31) Kilic, T.; Weissleder, R.; Lee, H. Molecular and Immunological Diagnostic Tests of COVID-19: Current Status and Challenges. *iScience* **2020**, *23* (8), 101406. <https://doi.org/10.1016/j.isci.2020.101406>.
- (32) Tian, B.; Gao, F.; Fock, J.; Dufva, M.; Hansen, M. F. Homogeneous Circle-to-Circle Amplification for Real-Time Optomagnetic Detection of SARS-CoV-2 RdRp Coding Sequence. *Biosens. Bioelectron.* **2020**, *165*, 112356. <https://doi.org/10.1016/j.bios.2020.112356>.
- (33) Kumar, V.; Mishra, S.; Sharma, R.; Agarwal, J.; Ghoshal, U.; Khanna, T.; Sharma, L. K.; Verma, S. K.; Tiwari, S.; Medicine, M.; Pgims, S. G.; Road, R.; Sciences, M.; Pgims, S. G.; Road, R.; Council, I.; Bhawan, R.; Delhi, N.; Tiwari, S.; Medicine, M.; Science, M. Development of RNA-Based Assay for Rapid Detection of SARS-CoV-2 in Clinical Samples. *bioRxiv* **2020**. <https://doi.org/doi.org/10.1101/2020.06.30.172833>.
- (34) Tan, S. Y. H.; Kwek, S. Y. M.; Low, H.; Pang, Y. L. J. Absolute Quantification of SARS-CoV-2 with Clarity PlusTM Digital PCR. *Methods* **2022**, *201*, 26–33. <https://doi.org/10.1016/j.ymeth.2021.07.005>.
- (35) Hosseini, A.; Pandey, R.; Osman, E.; Victorious, A.; Li, F.; Didar, T.; Soleymani, L. Roadmap to the Bioanalytical Testing of COVID-19: From Sample Collection to Disease Surveillance. *ACS Sensors* **2020**. <https://doi.org/10.1021/acssensors.0c01377>.
- (36) Ravi, N.; Cortade, D. L.; Ng, E.; Wang, S. X. Diagnostics for SARS-CoV-2 Detection Review of the FDA-EUA Testing Landscape. *Biosens. Bioelectron.* **2020**, *165*, 112454. <https://doi.org/10.1016/j.bios.2020.112454>.
- (37) Chen, X.; Kang, Y.; Luo, J.; Pang, K.; Xu, X.; Wu, J.; Li, X. Next-Generation Sequencing Reveals the Progression of COVID-19. *Front. Cell. Infect. Microbiol.* **2021**, *11*. <https://doi.org/10.3389/fcimb.2021.632490>.
- (38) Chow, F. W. N.; Chan, T. T. Y.; Tam, A. R.; Zhao, S.; Yao, W.; Fung, J.; Cheng, F. K. K.; Lo, G. C. S.; Chu, S.; Aw-Yong, K. L.; Tang, J. Y. M.; Tsang, C. C.; Luk, H. K. H.; Wong, A. C. P.; Li, K. S. M.; Zhu, L.; He, Z.; Tam, E. W. T.; Chung, T. W. H.; Wong, S. C. Y.; Que, T. L.; Fung, K. S. C.; Lung, D. C.; Wu, A. K. L.; Hung, I. F. N.; Woo, P. C. Y.; Lau, S. K. P. A Rapid, Simple, Inexpensive, and Mobile Colorimetric Assay Covid-19-Lamp for Mass on-Site Screening of Covid-19. *Int. J. Mol. Sci.* **2020**, *21* (15), 1–10. <https://doi.org/10.3390/ijms21155380>.
- (39) Dao Thi, V. L.; Herbst, K.; Boerner, K.; Meurer, M.; Kremer, L. P. M.; Kirrmaier, D.; Freistaedter, A.; Papagiannidis, D.; Galmozzi, C.; Stanifer, M. L.; Boulant, S.; Klein, S.; Chlanda, P.; Khalid, D.; Miranda, I. B.; Schnitzler, P.; Kräusslich, H. G.; Knop, M.; Anders, S. A Colorimetric RT-LAMP Assay and LAMP-Sequencing for Detecting SARS-CoV-2 RNA in Clinical Samples. *Sci. Transl. Med.* **2020**, *12* (556). <https://doi.org/10.1126/SCITRANSLMED.ABC7075>.
- (40) Perna, F.; Bruzzaniti, S.; Piemonte, E.; Maddaloni, V.; Atripaldi, L.; Sale, S.;

- Sanduzzi, A.; Nicastro, C.; Pepe, N.; Bifulco, M.; Matarese, G.; Galgani, M.; Atripaldi, L. Serum Levels of SARS-CoV-2 Nucleocapsid Antigen Associate with Inflammatory Status and Disease Severity in COVID-19 Patients. *Clin. Immunol.* **2021**, 226 (January). <https://doi.org/10.1016/j.clim.2021.108720>.
- (41) Chen, Z.; Zhang, Z.; Zhai, X.; Li, Y.; Lin, L.; Zhao, H.; Bian, L.; Li, P.; Yu, L.; Wu, Y.; Lin, G. Rapid and Sensitive Detection of Anti-SARS-CoV-2 IgG, Using Lanthanide-Doped Nanoparticles-Based Lateral Flow Immunoassay. *Anal. Chem.* **2020**, 92 (10), 7226–7231. <https://doi.org/10.1021/acs.analchem.0c00784>.
- (42) Elledge, S. K.; Zhou, X. X.; Byrnes, J. R.; Martinko, A. J.; Lui, I.; Pance, K.; Lim, S. A.; Glasgow, J. E.; Glasgow, A. A.; Turcios, K.; Iyer, N. S.; Torres, L.; Peluso, M. J.; Henrich, T. J.; Wang, T. T.; Tato, C. M.; Leung, K. K.; Greenhouse, B.; Wells, J. A. Engineering Luminescent Biosensors for Point-of-Care SARS-CoV-2 Antibody Detection. *Nat. Biotechnol.* **2021**, 39 (8), 928–935. <https://doi.org/10.1038/s41587-021-00878-8>.
- (43) Li, Z.; Yi, Y.; Luo, X.; Xiong, N.; Liu, Y.; Li, S.; Sun, R.; Wang, Y.; Hu, B.; Chen, W.; Zhang, Y.; Wang, J.; Huang, B.; Lin, Y.; Yang, J.; Cai, W.; Wang, X.; Cheng, J.; Chen, Z.; Sun, K.; Pan, W.; Zhan, Z.; Chen, L.; Ye, F. Development and Clinical Application of a Rapid IgM-IgG Combined Antibody Test for SARS-CoV-2 Infection Diagnosis. *J. Med. Virol.* **2020**, 92, 1518–1524.
- (44) Djaileb, A.; Charron, B.; Jodaylami, M. H.; Thibault, V.; Coutu, J.; Stevenson, K.; Forest, S.; Live, L. S.; Boudreau, D.; Pelletier, J. N.; Masson, J. F. A Rapid and Quantitative Serum Test for SARS-CoV-2 Antibodies with Portable Surface Plasmon Resonance Sensing. *ChemRxiv* **2020**, 1–12.
- (45) Zhang, Y. Electrochemical Biosensors for the Detection of SARS-CoV-2 Pathogen and Protein Biomarkers. *Int. J. Electrochem. Sci.* **2022**, 17, ArticleID:220541. <https://doi.org/10.20964/2022.05.13>.
- (46) Ventura, B. Della; Cennamo, M.; Minopoli, A.; Campanile, R.; Censi, S. B.; Terracciano, D.; Portella, G.; Velotta, R. Colorimetric Test for Fast Detection of SARS-COV-2 in Nasal and Throat Swabs. *ACS Sensors* **2020**, 5 (10), 3043–3048. <https://doi.org/10.1021/acssensors.0c01742>.
- (47) Whitman, J. D.; Hiatt, J.; Mowery, C. T.; Shy, B. R.; Yu, R.; Yamamoto, T. N.; Rathore, U.; Goldgof, G. M.; Whitty, C.; Woo, J. M.; Gallman, A. E.; Miller, T. E.; Levine, A. G.; Nguyen, D. N.; Bapat, S. P.; Balcerek, J.; Bylsma, S. A.; Lyons, A. M.; Li, S.; Wong, A. W.; Gills-Buck, E. M.; Steinhart, Z. B.; Lee, Y.; Apathy, R.; Lipke, M. J.; Smith, J. A.; Zheng, T.; Boothby, I. C.; Isaza, E.; Chan, J.; Acenas, D. D.; Lee, J.; Macrae, T. A.; Kyaw, T. S.; Wu, D.; Ng, D. L.; Gu, W.; York, V. A.; Eskandarian, H. A.; Callaway, P. C.; Warriar, L.; Moreno, M. E.; Levan, J.; Torres, L.; Farrington, L. A.; Loudermilk, R.; Koshal, K.; Zorn, K. C.; Garcia-Beltran, W. F.; Yang, D.; Astudillo, M. G.; Berstein, B. E.; Gelfand, J. A.; Ryan, E. T.; Charles, R. C.; Iafate, A. J.; Lennerz, J. K.; Miller, S.; Chiu, C. Y.; Stramer, S. L.; Wilson, M. R.; Manglik, A.; Ye, C. J.; Krogan, N. J.; Anderson, M. S.; Cyster, J. G.; Ernst,

- J. D.; Wu, A. H. B.; Lynch, K. L.; Bern, C.; Hsu, P. D.; Marson, A. Test Performance Evaluation of SARS-CoV-2 Serological Assays. *medRxiv* **2020**. <https://doi.org/10.1101/2020.04.25.20074856>.
- (48) Samson, R.; Navale, G. R.; Dharne, M. S. Biosensors: Frontiers in Rapid Detection of COVID - 19. *3 Biotech* **2020**, *10* (385).
- (49) Ghaffari, A.; Meurant, R.; Ardakani, A. COVID-19 Serological Tests: How Well Do They Actually Perform? *Diagnostics* **2020**, *10* (7), 1–14. <https://doi.org/10.3390/diagnostics10070453>.
- (50) Zhang, W.; Du, R. H.; Li, B.; Zheng, X. S.; Yang, X. Lou; Hu, B.; Wang, Y. Y.; Xiao, G. F.; Yan, B.; Shi, Z. L.; Zhou, P. Molecular and Serological Investigation of 2019-NCoV Infected Patients: Implication of Multiple Shedding Routes. *Emerg. Microbes Infect.* **2020**, *9* (1), 386–389. <https://doi.org/10.1080/22221751.2020.1729071>.
- (51) Li, H.; Liu, Z.; He, Y.; Qi, Y.; Chen, J.; Ma, Y.; Liu, F.; Lai, K.; Zhang, Y.; Jiang, L.; Wang, X.; Ge, J. A New and Rapid Approach for Detecting COVID-19 Based on S1 Protein Fragments. *Clin. Transl. Med.* **2020**, *10* (2), 6–11. <https://doi.org/10.1002/ctm2.90>.
- (52) Zeng, W.; Liu, G.; Ma, H.; Zhao, D.; Yang, Y.; Liu, M.; Mohammed, A.; Zhao, C.; Yang, Y.; Xie, J.; Ding, C.; Ma, X.; Weng, J.; Gao, Y.; He, H.; Jin, T. Biochemical Characterization of SARS-CoV-2 Nucleocapsid Protein. *Biochem. Biophys. Res. Commun.* **2020**, *527* (3), 618–623. <https://doi.org/10.1016/j.bbrc.2020.04.136>.
- (53) Stanborough, T.; Given, F. M.; Koch, B.; Sheen, C. R.; Stowers-Hull, A. B.; Waterland, M. R.; Crittenden, D. L. Optical Detection of CoV-SARS-2 Viral Proteins to Sub-Picomolar Concentrations. *ACS Omega* **2021**, *6* (9), 6404–6413. <https://doi.org/acsomega.1c00008>.
- (54) Wang, J.; Jiang, F.; Xiao, Z.; Wang, T.; Wang, J.; Bie, L.; Saleh, L.; Frey, K.; Zhang, L. Rapid and Sensitive Multiplex Detection of COVID-19 Antigens and Antibody Using Electrochemical Immunosensor-/Aptasensor-Enabled Biochips. *Chem. Commun.* **2022**. <https://doi.org/10.1039/d2cc01598f>.
- (55) Masterson, A. N.; Sardar, R. Selective Detection and Ultrasensitive Quantification of SARS-CoV - 2 IgG Antibodies in Clinical Plasma Samples Using Epitope-Modified Nanoplasmonic Biosensing Platforms. *Appl. Mater. Interfaces* **2022**. <https://doi.org/10.1021/acsami.2c06599>.
- (56) Li, Y. H.; Li, J.; Liu, X. E.; Wang, L.; Li, T.; Zhou, Y. H.; Zhuang, H. Detection of the Nucleocapsid Protein of Severe Acute Respiratory Syndrome Coronavirus in Serum: Comparison with Results of Other Viral Markers. *J. Virol. Methods* **2005**, *130* (1–2), 45–50. <https://doi.org/10.1016/j.jviromet.2005.06.001>.
- (57) Aziz, A.; Asif, M.; Ashraf, G.; Farooq, U.; Yang, Q.; Wang, S. Trends in Biosensing Platforms for SARS-CoV-2 Detection: A Critical Appraisal against Standard

- Detection Tools. *Curr. Opin. Colloid Interface Sci.* **2021**, *52*, 101418. <https://doi.org/10.1016/j.cocis.2021.101418>.
- (58) Lim, W. Y.; Lan, B. L.; Ramakrishnan, N. Emerging Biosensors to Detect Severe Acute Respiratory Syndrome Coronavirus 2 (SARS-CoV-2): A Review. *Biosensors* **2021**, *2* (11), 434. <https://doi.org/10.3390/bios11110434>.
- (59) Xu, L.; Li, D.; Ramadan, S.; Li, Y.; Klein, N. Facile Biosensors for Rapid Detection of COVID-19. *Biosens. Bioelectron.* **2020**, *170*, 112673. <https://doi.org/10.1016/j.bios.2020.112673>.
- (60) Qiu, G.; Gai, Z.; Tao, Y.; Schmitt, J.; Kullak-Ublick, G. A.; Wang, J. Dual-Functional Plasmonic Photothermal Biosensors for Highly Accurate Severe Acute Respiratory Syndrome Coronavirus 2 Detection. *ACS Nano* **2020**, *14* (5), 5268–5277. <https://doi.org/10.1021/acsnano.0c02439>.
- (61) Seo, G.; Lee, G.; Kim, M. J.; Baek, S. H.; Choi, M.; Ku, K. B.; Lee, C. S.; Jun, S.; Park, D.; Kim, H. G.; Kim, S. J.; Lee, J. O.; Kim, B. T.; Park, E. C.; Kim, S. II. Rapid Detection of COVID-19 Causative Virus (SARS-CoV-2) in Human Nasopharyngeal Swab Specimens Using Field-Effect Transistor-Based Biosensor. *ACS Nano* **2020**, *14* (4), 5135–5142. <https://doi.org/10.1021/acsnano.0c02823>.
- (62) Yakoh, A.; Pimpitak, U.; Rengpipat, S.; Hirankarn, N.; Chailapakul, O.; Chaiyo, S. Paper-Based Electrochemical Biosensor for Diagnosing COVID-19: Detection of SARS-CoV-2 Antibodies and Antigen. *Biosens. Bioelectron.* **2021**, *176* (December 2020), 112912. <https://doi.org/10.1016/j.bios.2020.112912>.
- (63) Funari, R.; Chu, K. Y.; Shen, A. Q. Detection of Antibodies against SARS-CoV-2 Spike Protein by Gold Nanospikes in an Opto-Microfluidic Chip. *Biosens. Bioelectron.* **2020**, *169* (August), 112578. <https://doi.org/10.1016/j.bios.2020.112578>.
- (64) Yadav, S.; Sadique, M. A.; Ranjan, P.; Kumar, N.; Singhal, A.; Srivastava, A. K.; Khan, R. Sers Based Lateral Flow Immunoassay for Point-of-Care Detection of SARS-CoV-2 in Clinical Samples. *ACS Appl. Bio Mater.* **2021**, *4* (4), 2974–2995. <https://doi.org/10.1021/acsbm.1c00102>.
- (65) Ma, X.; Lepoitevin, M.; Serre, C. Metal-Organic Frameworks towards Bio-Medical Applications. *Mater. Chem. Front.* **2021**, *5* (15), 5573–5594. <https://doi.org/10.1039/d1qm00784j>.
- (66) Jiang, Z. W.; Zhao, T. T.; Li, C. M.; Li, Y. F.; Huang, C. Z. 2D MOF-Based Photoelectrochemical Aptasensor for SARS-CoV-2 Spike Glycoprotein Detection. *ACS Appl. Mater. Interfaces* **2021**, *13* (42), 49754–49761. <https://doi.org/10.1021/acsaami.1c17574>.
- (67) Srivastava, M.; Srivastava, N.; Mishra, P. K.; Malhotra, B. D. Prospects of Nanomaterials-Enabled Biosensors for COVID-19 Detection. *Sci. Total Environ.* **2021**, *754*, 142363. <https://doi.org/10.1016/j.scitotenv.2020.142363>.

- (68) Mehmandoust, M.; Gumus, Z. P.; Soylak, M.; Erk, N. Electrochemical Immunosensor for Rapid and Highly Sensitive Detection of SARS-CoV-2 Antigen in the Nasal Sample. *Talanta* **2022**, *240*, 123211. <https://doi.org/10.1016/j.talanta.2022.123211>.
- (69) Rabiee, N.; Fatahi, Y.; Ahmadi, S.; Abbariki, N.; Ojaghi, A.; Rabiee, M.; Radmanesh, F.; Dinarvand, R.; Bagherzadeh, M.; Mostafavi, E.; Ashrafizadeh, M.; Makvandi, P.; Lima, E. C.; Saeb, M. R. Bioactive Hybrid Metal-Organic Framework (MOF)-Based Nanosensors for Optical Detection of Recombinant SARS-CoV-2 Spike Antigen. *Sci. Total Environ.* **2022**, *825*, 153902. <https://doi.org/10.1016/j.scitotenv.2022.153902>.
- (70) Raziq, A.; Kidakova, A.; Boroznjak, R.; Reut, J.; Öpik, A.; Syritski, V. Development of a Portable MIP-Based Electrochemical Sensor for Detection of SARS-CoV-2 Antigen. *Biosens. Bioelectron.* **2021**, *178* (January). <https://doi.org/10.1016/j.bios.2021.113029>.
- (71) EL Sharif, H. F.; Dennison, S. R.; Tully, M.; Crossley, S.; Mwangi, W.; Bailey, D.; Graham, S. P.; Reddy, S. M. Evaluation of Electropolymerized Molecularly Imprinted Polymers (E-MIPs) on Disposable Electrodes for Detection of SARS-CoV-2 in Saliva. *Anal. Chim. Acta* **2022**, *1206*, 339777. <https://doi.org/10.1016/j.aca.2022.339777>.
- (72) Haghayegh, F.; Salahandish, R.; Hassani, M.; Sanati-Nezhad, A. Highly Stable Buffer-Based Zinc Oxide/Reduced Graphene Oxide Nanosurface Chemistry for Rapid Immunosensing of SARS-CoV-2 Antigens. *ACS Appl. Mater. Interfaces* **2022**, *14* (8), 10844–10855. <https://doi.org/10.1021/acsami.1c24475>.
- (73) Sadique, M. A.; Yadav, S.; Ranjan, P.; Khan, R.; Khan, F.; Kumar, A.; Biswas, D. Highly Sensitive Electrochemical Immunosensor Platforms for Dual Detection of SARS-CoV-2 Antigen and Antibody Based on Gold Nanoparticle Functionalized Graphene Oxide Nanocomposites. *ACS Appl. Bio Mater.* **2022**, *5* (5), 2421–2430. <https://doi.org/10.1021/acsabm.2c00301>.
- (74) Gremmels, H.; Winkel, B. M. F.; Schuurman, R.; Rosingh, A.; Rigter, N. A. M.; Rodriguez, O.; Ubijaan, J.; Wensing, A. M. J.; Bonten, M. J. M.; Hofstra, L. M. Real-Life Validation of the Panbio™ COVID-19 Antigen Rapid Test (Abbott) in Community-Dwelling Subjects with Symptoms of Potential SARS-CoV-2 Infection. *EClinicalMedicine* **2021**, *31*, 100677. <https://doi.org/10.1016/j.eclinm.2020.100677>.
- (75) Lee, J. H.; Choi, M.; Jung, Y.; Lee, S. K.; Lee, C. S.; Kim, J.; Kim, J.; Kim, N. H.; Kim, B. T.; Kim, H. G. A Novel Rapid Detection for SARS-CoV-2 Spike 1 Antigens Using Human Angiotensin Converting Enzyme 2 (ACE2). *Biosens. Bioelectron.* **2021**, *171*, 112715. <https://doi.org/10.1016/j.bios.2020.112715>.
- (76) Suh, J. S.; Kim, H. S.; Kim, T. J. Development of a SARS-CoV-2-Derived Receptor-Binding Domain-Based ACE2 Biosensor. *Sensors Actuators, B Chem.* **2021**, *334*,

129663. <https://doi.org/10.1016/j.snb.2021.129663>.

- (77) Torres, M. D. T.; de Araujo, W. R.; de Lima, L. F.; Ferreira, A. L.; de la Fuente-Nunez, C. Low-Cost Biosensor for Rapid Detection of SARS-CoV-2 at the Point of Care. *Matter* **2021**, *4* (7), 2403–2416. <https://doi.org/10.1016/j.matt.2021.05.003>.
- (78) Gao, B.; Rojas Chavez, A. A.; Malkawi, W. I.; Keefe, D. W.; Smith, R.; Haim, H.; Salem, A. K.; Toor, F. Sensitive Detection of SARS-CoV-2 Spike Protein Using Vertically-Oriented Silicon Nanowire Array-Based Biosensor. *Sens. Bio-Sensing Res.* **2022**, *36*, 100487. <https://doi.org/10.1016/j.sbsr.2022.100487>.
- (79) Vezza, V. J.; Butterworth, A.; Lasserre, P.; Blair, E. O.; MacDonald, A.; Hannah, S.; Rinaldi, C.; Hoskisson, P. A.; Ward, A. C.; Longmuir, A.; Setford, S.; Farmer, E. C. W.; Murphy, M. E.; Corrigan, D. K. An Electrochemical SARS-CoV-2 Biosensor Inspired by Glucose Test Strip Manufacturing Processes. *Chem. Commun.* **2021**, *57* (30), 3704–3707. <https://doi.org/10.1039/d1cc00936b>.
- (80) Soto, D.; Orozco, J. Peptide-Based Simple Detection of SARS-CoV-2 with Electrochemical Readout. *Anal. Chim. Acta* **2022**, *1205*, 339739. <https://doi.org/10.1016/j.aca.2022.339739>.
- (81) Chowdhury, S. M.; Talukder, S. A.; Khan, A. M.; Afrin, N.; Ali, M. A.; Islam, R.; Parves, R.; Al Mamun, A.; Sufian, M. A.; Hossain, M. N.; Hossain, M. A.; Halim, M. A. Antiviral Peptides as Promising Therapeutics against SARS-CoV-2. *J. Phys. Chem. B* **2020**, *124* (44), 9785–9792. <https://doi.org/10.1021/acs.jpccb.0c05621>.
- (82) Fu, Z.; Xiang, J. Aptamers, the Nucleic Acid Antibodies, in Cancer Therapy. *Int. J. Mol. Sci.* **2020**, *21* (8). <https://doi.org/10.3390/ijms21082793>.
- (83) Chakraborty, B.; Das, S.; Gupta, A.; Xiong, Y.; T-V, V.; Kizer, M. E.; Duan, J.; Chandrasekaran, A. R.; Wang, X. Aptamers for Viral Detection and Inhibition. *ACS Infect. Dis.* **2021**. <https://doi.org/10.1021/acsinfecdis.1c00546>.
- (84) Szunerits, S.; Pagneux, Q.; Swaidan, A.; Mishyn, V.; Roussel, A.; Cambillau, C.; Devos, D.; Engelmann, I.; Alidjinou, E. K.; Happy, H.; Boukherroub, R. The Role of the Surface Ligand on the Performance of Electrochemical SARS-CoV-2 Antigen Biosensors. *Anal. Bioanal. Chem.* **2022**, *414* (1), 103–113. <https://doi.org/10.1007/s00216-020-03137-y>.
- (85) Li, J.; Zhang, Z.; Gu, J.; Stacey, H. D.; Ang, J. C.; Capretta, A.; Filipe, C. D. M.; Mossman, K. L.; Balion, C.; Salena, B. J.; Yamamura, D.; Soleymani, L.; Miller, M. S.; Brennan, J. D.; Li, Y. Diverse High-Affinity DNA Aptamers for Wild-Type and B.1.1.7 SARS-CoV-2 Spike Proteins from a Pre-Structured DNA Library. *Nucleic Acids Res.* **2021**, *49* (13), 7267–7279. <https://doi.org/10.1093/nar/gkab574>.
- (86) Kacherovsky, N.; Yang, L. F.; Dang, H. V.; Cheng, E. L.; Cardle, I. I.; Walls, A. C.; McCallum, M.; Sellers, D. L.; DiMaio, F.; Salipante, S. J.; Corti, D.; Veesler, D.; Pun, S. H. Discovery and Characterization of Spike N-Terminal Domain- Binding Aptamers for Rapid SARS-CoV-2 Detection. *Angew. Chemie - Int. Ed.* **2021**, *133*

- (39), 21381–21385. <https://doi.org/10.1002/ange.202107730>.
- (87) Schmitz, A.; Weber, A.; Bayin, M.; Breuers, S.; Fieberg, V.; Famulok, M.; Mayer, G. A SARS-CoV-2 Spike Binding DNA Aptamer That Inhibits Pseudovirus Infection by an RBD-Independent Mechanism. *Angew. Chem. Int. Ed.* **2021**, *60*, 10279–10285. <https://doi.org/10.1002/anie.202100316>.
- (88) Song, Y.; Song, J.; Wei, X.; Huang, M.; Sun, M.; Zhu, L.; Lin, B.; Shen, H.; Zhu, Z.; Yang, C. Discovery of Aptamers Targeting the Receptor-Binding Domain of the SARS-CoV-2 Spike Glycoprotein. *Anal. Chem.* **2020**, *92* (14), 9895–9900. <https://doi.org/10.1021/acs.analchem.0c01394>.
- (89) Sun, M.; Liu, S.; Wei, X.; Wan, S.; Huang, M.; Song, T.; Lu, Y.; Weng, X.; Lin, Z.; Chen, H.; Song, Y.; Yang, C. Aptamer Blocking Strategy Inhibits SARS-CoV-2 Virus Infection. *Angew. Chemie* **2021**. <https://doi.org/10.1002/ange.202100225>.
- (90) Yang, G.; Li, Z.; Mohammed, I.; Zhao, L.; Wei, W.; Xiao, H.; Guo, W.; Zhao, Y.; Qu, F.; Huang, Y. Identification of SARS-CoV-2-against Aptamer with High Neutralization Activity by Blocking the RBD Domain of Spike Protein 1. *Signal Transduct. Target. Ther.* **2021**, *6* (1). <https://doi.org/10.1038/s41392-021-00649-6>.
- (91) Zhang, Z.; Li, J.; Gu, J.; Amini, R.; Stacey, H. D.; Ang, J. C.; White, D.; Filipe, C. D. M.; Mossman, K.; Miller, M. S.; Salena, B. J.; Yamamura, D.; Sen, P.; Soleymani, L.; Brennan, J. D.; Li, Y. A Universal DNA Aptamer That Recognizes Spike Proteins of Diverse SARS-CoV-2 Variants of Concern. *Chem. - A Eur. J.* **2022**, *28* (15). <https://doi.org/10.1002/chem.202200078>.
- (92) Li, J.; Zhang, Z.; Amini, R.; Li, Y. One Solution for All : Searching for Universal Aptamers for Constantly Mutating Spike Proteins of SARS-CoV-2. **2022**, *202200166*, 1–7.
- (93) Keefe, A. D.; Pai, S.; Ellington, A. Aptamers as Therapeutics. *Nat. Rev. Drug Discov.* **2010**, *9* (7), 537–550. <https://doi.org/10.1038/nrd3141>.
- (94) Wandtke, T.; Ewelina, W. Aptamers — Diagnostic and Therapeutic Solution in SARS-CoV-2. *Int. J. Mol. Sci.* **2022**, *23*. <https://doi.org/10.3390/ijms23031412> Academic.
- (95) Sun, M.; Liu, S.; Song, T.; Chen, F.; Zhang, J.; Huang, J. A.; Wan, S.; Lu, Y.; Chen, H.; Tan, W.; Song, Y.; Yang, C. Spherical Neutralizing Aptamer Inhibits SARS-CoV-2 Infection and Suppresses Mutational Escape. *J. Am. Chem. Soc.* **2021**, *143* (51), 21541–21548. <https://doi.org/10.1021/jacs.1c08226>.
- (96) Zamzami, M. A.; Rabbani, G.; Ahmad, A.; Basalah, A. A.; Al-Sabban, W. H.; Nate Ahn, S.; Choudhry, H. Carbon Nanotube Field-Effect Transistor (CNT-FET)-Based Biosensor for Rapid Detection of SARS-CoV-2 (COVID-19) Surface Spike Protein S1. *Bioelectrochemistry* **2022**, *143*, 107982. <https://doi.org/10.1016/j.bioelechem.2021.107982>.
- (97) Shao, W.; Shurin, M. R.; Wheeler, S. E.; He, X.; Star, A. Rapid Detection of SARS-

- CoV - 2 Antigens Using High-Purity Semiconducting Single-Walled Carbon Nanotube-Based Field-Effect Transistors. *ACS Appl. Mater. Interfaces* **2021**, *13*, 10321–10327. <https://doi.org/https://dx.doi.org/10.1021/acsami.0c22589>.
- (98) Curti, F.; Fortunati, S.; Knoll, W.; Giannetto, M.; Corradini, R.; Bertucci, A.; Careri, M. A Folding-Based Electrochemical Aptasensor for the Single-Step Detection of the SARS-CoV-2 Spike Protein. *ACS Appl. Mater. Interfaces* **2022**, *14*, 19204–19211. <https://doi.org/10.1021/acsami.2c02405>.
- (99) Rahmati, Z.; Roushani, M.; Hosseini, H.; Choobin, H. Label-Free Electrochemical Aptasensor for Rapid Detection of SARS-CoV-2 Spike Glycoprotein Based on the Composite of Cu(OH)₂ Nanorods Arrays as a High-Performance Surface Substrate. *Bioelectrochemistry* **2022**, *146* (March), 108106. <https://doi.org/10.1016/j.bioelechem.2022.108106>.
- (100) Sari, A. K.; Hartati, Y. W.; Gaffar, S.; Anshori, I.; Hidayat, D.; Wiraswati, H. L. The Optimization of an Electrochemical Aptasensor to Detect RBD Protein S SARS-CoV-2 as a Biomarker Using Screen-Printed Carbon Electrode/AuNP. *J. Electrochem. Sci. Eng.* **2022**, *21* (1), 219–235. <https://doi.org/http://dx.doi.org/10.5599/jese.1206>.
- (101) de Lima, L. F.; Ferreira, A. L.; Torres, M. D. T.; de Araujo, W. R.; de la Fuente-Nunez, C. Minute-Scale Detection of SARS-CoV-2 Using a Low-Cost Biosensor Composed of Pencil Graphite Electrodes. *Proc. Natl. Acad. Sci. U. S. A.* **2021**, *118* (30), 1–9. <https://doi.org/10.1073/pnas.2106724118>.
- (102) Karakuş, E.; Erdemir, E.; Demirbilek, N.; Liv, L. Colorimetric and Electrochemical Detection of SARS-CoV-2 Spike Antigen with a Gold Nanoparticle-Based Biosensor. *Anal. Chim. Acta* **2021**, *1182*. <https://doi.org/10.1016/j.aca.2021.338939>.
- (103) Mahari, S.; Roberts, A.; Shahdeo, D.; Gandhi, S. ECovSens-Ultrasensitive Novel In-House Built Printed Circuit Board Based Electrochemical Device for Rapid Detection of NCovid-19 Antigen, a Spike Protein Domain 1 of SARS-CoV-2. *bioRxiv* **2020**. <https://doi.org/10.1101/2020.04.24.059204>.
- (104) Amouzadeh Tabrizi, M.; Acedo, P. An Electrochemical Membrane-Based Aptasensor for Detection of Severe Acute Respiratory Syndrome Coronavirus-2 Receptor-Binding Domain. *Appl. Surf. Sci.* **2022**, *598*, 153867. <https://doi.org/10.1016/j.apsusc.2022.153867>.
- (105) Rashed, M. Z.; Kopechek, J. A.; Priddy, M. C.; Hamorsky, K. T.; Palmer, K. E.; Mittal, N.; Valdez, J.; Flynn, J.; Williams, S. J. Rapid Detection of SARS-CoV-2 Antibodies Using Electrochemical Impedance-Based Detector. *Biosens. Bioelectron.* **2021**, *171*, 112709. <https://doi.org/10.1016/j.bios.2020.112709>.
- (106) Yano, T.; Kajisa, T.; Ono, M.; Miyasaka, Y.; Hasegawa, Y. Ultrasensitive Detection of SARS - CoV - 2 Nucleocapsid Protein Using Large Gold Nanoparticle - Enhanced Surface Plasmon Resonance. *Scienti* **2022**, *12*, 1–8.

- (107) Cennamo, N.; Pasquardini, L.; Arcadio, F.; Lunelli, L.; Vanzetti, L.; Carafa, V.; Altucci, L.; Zeni, L. SARS-CoV-2 Spike Protein Detection through a Plasmonic D-Shaped Plastic Optical Fiber Aptasensor. *Talanta* **2021**, *233*, 122532. <https://doi.org/10.1016/j.talanta.2021.122532>.
- (108) Djaileb, A.; Hojjat Jodaylami, M.; Coutu, J.; Ricard, P.; Lamarre, M.; Rochet, L.; Cellier-Goetghebeur, S.; MacAulay, D.; Charron, B.; Lavallée, É.; Thibault, V.; Stevenson, K.; Forest, S.; Live, L. S.; Abonnenc, N.; Guedon, A.; Quessy, P.; Lemay, J. F.; Farnós, O.; Kamen, A.; Stuible, M.; Gervais, C.; Durocher, Y.; Cholette, F.; Mesa, C.; Kim, J.; Cayer, M. P.; De Grandmont, M. J.; Brouard, D.; Trottier, S.; Boudreau, D.; Pelletier, J. N.; Masson, J. F. Cross-Validation of ELISA and a Portable Surface Plasmon Resonance Instrument for IgG Antibody Serology with SARS-CoV-2 Positive Individuals. *Analyst* **2021**, *146* (15), 4905–4917. <https://doi.org/10.1039/d1an00893e>.
- (109) Ahmadvand, A.; Gerislioglu, B.; Ramezani, Z.; Kaushik, A.; Manickam, P.; Ghoreishi, S. A. Functionalized Terahertz Plasmonic Metasensors: Femtomolar-Level Detection of SARS-CoV-2 Spike Proteins. *Biosens. Bioelectron.* **2021**, *177*, 1–21. <https://doi.org/10.1016/j.bios.2021.112971>.
- (110) Zavyalova, E.; Ambartsumyan, O.; Zhdanov, G.; Gribanyov, D.; Gushchin, V.; Tkachuk, A.; Rudakova, E.; Nikiforova, M.; Kuznetsova, N.; Popova, L.; Verdiev, B.; Alatyrev, A.; Burtseva, E.; Ignatieva, A.; Iliukhina, A.; Dolzhikova, I.; Arutyunyan, A.; Gambaryan, A.; Kukushkin, V. Sers-Based Aptasensor for Rapid Quantitative Detection of Sars-Cov-2. *Nanomaterials* **2021**, *11* (6), 1–13. <https://doi.org/10.3390/nano11061394>.
- (111) Behrouzi, K.; Lin, L. Gold Nanoparticle Based Plasmonic Sensing for the Detection of SARS-CoV-2 Nucleocapsid Proteins. *Biosens. Bioelectron.* **2022**, *195* (September 2021), 113669. <https://doi.org/10.1016/j.bios.2021.113669>.
- (112) Yi, C.; Li, G.; Ivanov, D. N.; Wang, Z.; Velasco, M. X.; Hernández, G.; Kaundal, S.; Villarreal, J.; Gupta, Y. K.; Qiao, M.; Hubert, C. G.; Hart, M. J.; Penalva, L. O. F. Luteolin Inhibits Musashi1 Binding to RNA and Disrupts Cancer Phenotypes in Glioblastoma Cells. *RNA Biol.* **2018**, *15* (11), 1420–1432. <https://doi.org/10.1080/15476286.2018.1539607>.
- (113) Pattnaik, P. Surface Plasmon Resonance: Application in Understanding Receptor-Ligand Interaction. *Appl. Biochem. Biotechnol.* **2005**, *126*, 79–92. https://doi.org/10.1007/978-981-10-2021-6_2.
- (114) Nguyen, H. H.; Park, J.; Kang, S.; Kim, M. Surface Plasmon Resonance: A Versatile Technique for Biosensor Applications. *Sensors* **2015**, *15* (5), 10481–10510. <https://doi.org/10.3390/s150510481>.
- (115) Takemura, K. Surface Plasmon Resonance (SPR)-and Localized Spr (LSPR)-Based Virus Sensing Systems: Optical Vibration of Nano-and Micro-Metallic Materials for the Development of next-Generation Virus Detection Technology. *Biosensors*

2021, 11 (8). <https://doi.org/10.3390/bios11080250>.

- (116) Mayer, K. M.; Hafner, J. H. Localized Surface Plasmon Resonance Sensors. *Chem. Rev.* **2011**, *111*, 3828–3857. <https://doi.org/10.1021/cr100313v>.
- (117) Kimple, A. J.; Muller, R. E.; Siderovski, D. P.; Willard, F. S. A Capture Coupling Method for the Covalent Immobilization of Hexahistidine Tagged Proteins for Surface Plasmon Resonance. *Methods Mol. Biol.* **2010**, *627*, 91–100. https://doi.org/10.1007/978-1-60761-670-2_5.
- (118) Hutter, E.; Fendler, J. H. Exploitation of Localized Surface Plasmon Resonance. *Adv. Mater.* **2004**, *16* (19), 1685–1706. <https://doi.org/10.1002/adma.200400271>.
- (119) Zhao, J.; Zhang, X.; Yonzon, C. R.; Haes, A. J.; Duyne, R. P. Van. Localized Surface Plasmon Resonance Sensors. *Nanomedicine* **2006**, *1* (2), 219–228. <https://doi.org/10.2217/17435889.1.2.219>.
- (120) Bousiakou, L. G.; Gebavi, H.; Mikac, L.; Karapetis, S.; Ivanda, M. Surface Enhanced Raman Spectroscopy for Molecular Identification- A Review on Surface Plasmon Resonance (SPR) and Localised Surface Plasmon Resonance (LSPR) in Optical Nanobiosensing. *Croat. Chem. Acta* **2019**, *92* (4), 479–494. <https://doi.org/10.5562/cca3558>.
- (121) Moitra, P.; Alafeef, M.; Alafeef, M.; Alafeef, M.; Dighe, K.; Frieman, M. B.; Pan, D.; Pan, D.; Pan, D. Selective Naked-Eye Detection of SARS-CoV-2 Mediated by N Gene Targeted Antisense Oligonucleotide Capped Plasmonic Nanoparticles. *ACS Nano* **2020**, *14* (6), 7617–7627. <https://doi.org/10.1021/acsnano.0c03822>.
- (122) Zhang, Y.; Chen, M.; Liu, C.; Chen, J.; Luo, X.; Xue, Y.; Liang, Q.; Zhou, L.; Tao, Y.; Li, M.; Wang, D.; Zhou, J.; Wang, J. Sensitive and Rapid On-Site Detection of SARS-CoV-2 Using a Gold Nanoparticle-Based High-Throughput Platform Coupled with CRISPR/Cas12-Assisted RT-LAMP. *Sensors Actuators, B Chem.* **2021**, *345*, 130411. <https://doi.org/10.1016/j.snb.2021.130411>.
- (123) Zhao, Z.; Cui, H.; Song, W.; Ru, X.; Zhou, W.; Yu, X. A Simple Magnetic Nanoparticles-Based Viral RNA Extraction Method for Efficient Detection of SARS-CoV-2. *bioRxiv* **2020**. <https://doi.org/10.1101/2020.02.22.961268>.
- (124) Kim, S.; Hao, Y.; Miller, E. A.; Tay, D. M.; Yee, E.; Kongsuphol, P.; Jia, H.; McBee, M.; Preiser, P. R.; Sikes, H. D. Vertical Flow Cellulose-Based Assays for SARS-CoV-2 Antibody Detection in Human Serum. *ACS Sensors* **2021**. <https://doi.org/10.1021/acssensors.1c00235>.
- (125) EUA Authorized Serology Test Performance <https://www.fda.gov/medical-devices/coronavirus-disease-2019-covid-19-emergency-use-authorizations-medical-devices/eua-authorized-serology-test-performance> (accessed Sep 30, 2020).
- (126) Burbelo, P. D.; Riedo, F. X.; C, M.; Rawlings, S.; Smith, D.; Das, S.; Strich, J. R.; Chertow, D. S.; Davey, R. T.; Cohen, J. I. Detection of Nucleocapsid Antibody to

SARS-CoV-2 Is More Sensitive than Antibody to Spike Protein in COVID-19 Patients. *J. Chem. Inf. Model.* **2020**. <https://doi.org/DOI:10.1101/2020.04.20.20071423>.

- (127) Xu, X.; Sun, J.; Nie, S.; Li, H.; Kong, Y.; Liang, M.; Hou, J.; Huang, X.; Li, D.; Ma, T.; Peng, J.; Gao, S.; Shao, Y.; Zhu, H.; Lau, J. Y. N.; Wang, G.; Xie, C.; Jiang, L.; Huang, A.; Yang, Z.; Zhang, K.; Hou, F. F. Seroprevalence of Immunoglobulin M and G Antibodies against SARS-CoV-2 in China. *Nat. Med.* **2020**, *26* (8), 1193–1195. <https://doi.org/10.1038/s41591-020-0949-6>.
- (128) Zhou, L.; Hao, P.; Li, H.; Zhang, Z. Electrochemical Resonance of Molecular Motion Enabling Label-Antibody-, and Enzyme-Free Detection of SARS-CoV-2. *ACS Sensors* **2021**, *6*, 1613–1620. <https://doi.org/doi.org/10.1021/acssensors.1c00022>.
- (129) Udugama, B.; Kadhiresan, P.; Kozlowski, H. N.; Malekjahani, A.; Osborne, M.; Li, V. Y. C.; Chen, H.; Mubareka, S.; Gubbay, J. B.; Chan, W. C. W. Diagnosing COVID-19: The Disease and Tools for Detection. *ACS Nano* **2020**, *14* (4), 3822–3835. <https://doi.org/10.1021/acsnano.0c02624>.
- (130) Huang, L.; Ding, L.; Zhou, J.; Chen, S.; Chen, F.; Zhao, C.; Xu, J.; Hu, W.; Ji, J.; Xu, H.; Liu, G. L. One-Step Rapid Quantification of SARS-CoV-2 Virus Particles via Low-Cost Nanoplasmonic Sensors in Generic Microplate Reader and Point-of-Care Device. *Biosens. Bioelectron.* **2021**, *171*, 112685. <https://doi.org/10.1016/j.bios.2020.112685>.
- (131) Chen, Z.; Wu, Q.; Chen, J.; Ni, X.; Dai, J. A DNA Aptamer Based Method for Detection of SARS-CoV-2 Nucleocapsid Protein. *Virol. Sin.* **2020**, *35* (3), 351–354. <https://doi.org/10.1007/s12250-020-00236-z>.
- (132) Wrapp, D.; Wang, N.; Corbett, K. S.; Goldsmith, J. A.; Hsieh, C.-L.; Abiona, O.; Graham, B. S.; McLellan, J. S. Cryo-EM Structure of the 2019-NCoV Spike in the Prefusion Conformation. *Science* (80-.). **2020**, *367*, 1260–1263. <https://doi.org/DOI:10.1126/science.abb2507>.
- (133) Mariani, S.; Minunni, M. Surface Plasmon Resonance Applications in Clinical Analysis. *Anal. Bioanal. Chem.* **2014**, *406* (9–10), 2303–2323. <https://doi.org/10.1007/s00216-014-7647-5>.
- (134) Schasfoort, R. B. M. *Handbook of Surface Plasmon Resonance*; Royal Society of Chemistry, 2017.
- (135) Mocak, J.; Bond, A. M.; Mitchell, S.; Scollary, G.; Bond, A. M. A Statistical Overview of Standard (IUPAC and ACS) and New Procedures for Determining the Limits of Detection and Quantification: Application to Voltammetric and Stripping Techniques. *Pure Appl. Chem.* **1997**, *69* (2), 297–328. <https://doi.org/10.1351/pac199769020297>.
- (136) Zuker, M. Mfold Web Server for Nucleic Acid Folding and Hybridization

- Prediction. *Nucleic Acids Res.* **2003**, *31* (13), 3406–3415. <https://doi.org/10.1093/nar/gkg595>.
- (137) Antczak, M.; Popena, M.; Zok, T.; Sarzynska, J.; Ratajczak, T.; Tomczyk, K.; Adamiak, R. W.; Szachniuk, M. New Functionality of RNAComposer: An Application to Shape the Axis of MiR160 Precursor Structure. *Acta Biochim. Pol.* **2016**, *63* (4), 737–744. https://doi.org/10.18388/abp.2016_1329.
- (138) Schneidman-Duhovny, D.; Inbar, Y.; Nussinov, R.; Wolfson, H. J. PatchDock and SymmDock: Servers for Rigid and Symmetric Docking. *Nucleic Acids Res.* **2005**, *33*, W363–W367. <https://doi.org/10.1093/nar/gki481>.
- (139) Duhovny, D.; Nussinov, R.; Wolfson, H. J. Efficient Unbound Docking of Rigid Molecules. In *Proceedings of the 2'nd Workshop on Algorithms in Bioinformatics(WABI) Rome, Italy, Lecture Notes in Computer Science 2452*; Guigo', R., Gusfield, D., Eds.; Springer Verlag: Rome, Italy, 2002; pp 185–200.
- (140) Ogata, A. F.; Maley, A. M.; Wu, C.; Gilboa, T.; Norman, M.; Lazarovits, R.; Mao, C. P.; Newton, G.; Chang, M.; Nguyen, K.; Kamkaew, M.; Zhu, Q.; Gibson, T. E.; Ryan, E. T.; Charles, R. C.; Marasco, W. A.; Walt, D. R. Ultra-Sensitive Serial Profiling of SARS-CoV-2 Antigens and Antibodies in Plasma to Understand Disease Progression in COVID-19 Patients with Severe Disease. *Clin. Chem.* **2020**, *66* (12), 1562–1572. <https://doi.org/10.1093/clinchem/hvaa213>.
- (141) Tan, L. Van; Ngoc, N. M.; That, B. T. T.; Uyen, L. T. T.; Hong, N. T. T.; Dung, N. T. P.; Nhu, L. N. T.; Thanh, T. T.; Man, D. N. H.; Phong, N. T.; Hien, T. T.; Truong, N. T.; Thwaites, G.; Chau, N. V. V. Duration of Viral Detection in Throat and Rectum of a Patient with COVID-19. *medRxiv* **2020**, 2020.03.07.20032052.
- (142) Teh, H. F.; Peh, W. Y. X.; Su, X.; Thomsen, J. S. Characterization of Protein-DNA Interactions Using Surface Plasmon Resonance Spectroscopy with Various Assay Schemes. *Biochemistry* **2007**, *46* (8), 2127–2135. <https://doi.org/10.1021/bi061903t>.
- (143) Ahmed, F. E.; Wiley, J. E.; Weidner, D. A.; Bonnerup, C.; Mota, H. Surface Plasmon Resonance (SPR) Spectrometry as a Tool to Analyze Nucleic Acid-Protein Interactions in Crude Cellular Extracts. *Cancer Genomics and Proteomics* **2010**, *7* (6), 303–310.
- (144) Heiat, M.; Najafi, A.; Ranjbar, R.; Latifi, A. M.; Rasaei, M. J. Computational Approach to Analyze Isolated SsDNA Aptamers against Angiotensin II. *J. Biotechnol.* **2016**, *230*, 34–39. <https://doi.org/10.1016/j.jbiotec.2016.05.021>.
- (145) Bruno, J. G. Integration of Multiple Computer Modeling Software Programs for Characterization of a Brain Natriuretic Peptide Sandwich DNA Aptamer Complex. *Journal of Molecular Recognition*. 2019. <https://doi.org/10.1002/jmr.2809>.
- (146) Liu, J.; Wachsmann-hogiu, S. Progress and Challenges of Point-of-Need Photonic Biosensors for the Diagnosis of COVID-19 Infections and Immunity. *Biosensors*

2022, 12, 678.

- (147) Bong, J. H.; Kim, T. H.; Jung, J.; Lee, S. J.; Sung, J. S.; Lee, C. K.; Kang, M. J.; Kim, H. O.; Pyun, J. C. Pig Sera-Derived Anti-SARS-CoV-2 Antibodies in Surface Plasmon Resonance Biosensors. *Biochip J.* **2020**, *14* (4), 358–368. <https://doi.org/10.1007/s13206-020-4404-z>.
- (148) Ehsan, M. A.; Khan, S. A.; Rehman, A. Screen-Printed Graphene/Carbon Electrodes on Paper Substrates as Impedance Sensors for Detection of Coronavirus in Nasopharyngeal Fluid Samples. *Diagnostics* **2021**, *11* (6). <https://doi.org/10.3390/diagnostics11061030>.
- (149) Chiodi, E.; Marn, A. M.; Geib, M. T.; Selim Ünlü, M. The Role of Surface Chemistry in the Efficacy of Protein and Dna Microarrays for Label-Free Detection: An Overview. *Polymers (Basel)*. **2021**, *13* (7), 1–21. <https://doi.org/10.3390/polym13071026>.
- (150) Lautner, G.; Balogh, Z.; Bardóczy, V.; Mészáros, T.; Gyurcsányi, R. E. Aptamer-Based Biochips for Label-Free Detection of Plant Virus Coat Proteins by SPR Imaging. *Analyst* **2010**, *135* (5), 918–926. <https://doi.org/10.1039/b922829b>.
- (151) Lape, J. E. Biophysical Investigations of the Interactions between Calmodulin and Nitric Oxide Synthase Enzymes, University of Waterloo, 2017.
- (152) Khilko, S. N.; Corr, M.; Boyd, L. F.; Lees, A.; Inman, J. K.; Margulies, D. H. Direct Detection of Major Histocompatibility Complex Class I Binding to Antigenic Peptides Using Surface Plasmon Resonance. *J. Biol. Chem.* **1993**, *268* (21), 15425–15434. [https://doi.org/10.1016/S0021-9258\(18\)82275-X](https://doi.org/10.1016/S0021-9258(18)82275-X).
- (153) Chiu, N. F.; Kuo, C. T.; Chen, C. Y. High-Affinity Carboxyl-Graphene Oxide-Based SPR Aptasensor for the Detection of HCG Protein in Clinical Serum Samples. *Int. J. Nanomedicine* **2019**, *14*, 4833–4847. <https://doi.org/10.2147/IJN.S208292>.
- (154) He, Y.; Jiao, B. DNA Covalently Linked to Graphene Oxide for Biotin–Streptavidin Interaction Assay. *Talanta* **2017**, *163*, 140–145. <https://doi.org/10.1016/j.talanta.2016.10.096>.
- (155) Polonschii, C.; David, S.; Tombelli, S.; Mascini, M.; Gheorghiu, M. A Novel Low-Cost and Easy to Develop Functionalization Platform. Case Study: Aptamer-Based Detection of Thrombin by Surface Plasmon Resonance. *Talanta* **2010**, *80* (5), 2157–2164. <https://doi.org/10.1016/j.talanta.2009.11.023>.
- (156) Hong, S. C.; Chen, H.; Lee, J.; Park, H. K.; Kim, Y. S.; Shin, H. C.; Kim, C. M.; Park, T. J.; Lee, S. J.; Koh, K.; Kim, H. J.; Chang, C. L.; Lee, J. Ultrasensitive Immunosensing of Tuberculosis CFP-10 Based on SPR Spectroscopy. *Sensors Actuators, B Chem.* **2011**, *156* (1), 271–275. <https://doi.org/10.1016/j.snb.2011.04.032>.
- (157) Yao, X.; Li, X.; Toledo, F.; Zurita-Lopez, C.; Gutova, M.; Momand, J.; Zhou, F. Sub-Attomole Oligonucleotide and P53 CDNA Determinations via a High-

- Resolution Surface Plasmon Resonance Combined with Oligonucleotide-Capped Gold Nanoparticle Signal Amplification. *Anal. Biochem.* **2006**, *354* (2), 220–228. <https://doi.org/10.1016/j.ab.2006.04.011>.
- (158) Kim, Y. H.; Kim, J. P.; Han, S. J.; Sim, S. J. Aptamer Biosensor for Label-Free Detection of Human Immunoglobulin E Based on Surface Plasmon Resonance. *Sensors Actuators, B Chem.* **2009**, *139* (2), 471–475. <https://doi.org/10.1016/j.snb.2009.03.013>.
- (159) Su, X.; Wu, Y. J.; Robelek, R.; Knoll, W. Surface Plasmon Resonance Spectroscopy and Quartz Crystal Microbalance Study of Streptavidin Film Structure Effects on Biotinylated DNA Assembly and Target DNA Hybridization. *Langmuir* **2005**, *21* (1), 348–353. <https://doi.org/10.1021/la047997u>.
- (160) Mohseni, S.; Moghadam, T. T.; Dabirmanesh, B.; Jabbari, S.; Khajeh, K. Development of a Label-Free SPR Sensor for Detection of Matrixmetalloproteinase-9 by Antibody Immobilization on Carboxymethyl-dextran Chip. *Biosens. Bioelectron.* **2016**, *81*, 510–516. <https://doi.org/10.1016/j.bios.2016.03.038>.
- (161) Piazza, M.; Dieckmann, T.; Guillemette, J. G. Structural Studies of a Complex between Endothelial Nitric Oxide Synthase and Calmodulin at Physiological Calcium Concentration. *Biochemistry.* **2016**, pp 5962–5971. <https://doi.org/10.1021/acs.biochem.6b00821>.
- (162) Grasso, G.; Agata, R. D.; Rizzarelli, E.; Spoto, G.; Andrea, L. D.; Pedone, C.; Picardi, A.; Romanelli, A.; Fragai, M.; Yeo, K. J. Activity of Anchored Human Matrix Metalloproteinase-1 Catalytic Domain on Au (111) Surfaces Monitored By. **2005**, No. 111, 1565–1571. <https://doi.org/10.1002/jms.929>.
- (163) Wang, R.; Tombelli, S.; Minunni, M.; Spiriti, M. M.; Mascini, M. Immobilisation of DNA Probes for the Development of SPR-Based Sensing. *Biosens. Bioelectron.* **2004**, *20* (5), 967–974. <https://doi.org/10.1016/j.bios.2004.06.013>.
- (164) Amaya-González, S.; López-López, L.; Miranda-Castro, R.; de-los-Santos-Álvarez, N.; Miranda-Ordieres, A. J.; Lobo-Castañón, M. J. Affinity of Aptamers Binding 33-Mer Gliadin Peptide and Gluten Proteins: INFLUENCE of Immobilization and Labeling Tags. *Anal. Chim. Acta* **2015**, *873*, 63–70. <https://doi.org/10.1016/j.aca.2015.02.053>.
- (165) Mannelli, I.; Minunni, M.; Tombelli, S.; Wang, R.; Spiriti, M. M.; Mascini, M. Direct Immobilisation of DNA Probes for the Development of Affinity Biosensors. *Bioelectrochemistry* **2005**, *66* (1-2 SPEC. ISS.), 129–138. <https://doi.org/10.1016/j.bioelechem.2004.04.008>.
- (166) Drescher, D. G.; Drescher, M. J.; Ramakrishnan, N. A. Surface Plasmon Resonance (SPR) Analysis of Binding Interactions of Proteins in Inner-Ear Sensory Epithelia. *Methods Mol. Biol.* **2009**, *493*, 323–343. https://doi.org/10.1007/978-1-59745-523-7_20.

- (167) Fischer, M. J. E. Amine Coupling through EDC/NHS A Practical Approach. In *Surface Plasmon Resonance, Methods in Molecular Biology*; de Mol, N. J., Fischer, M. J. E., Eds.; Springer Science+Business Media, 2010; pp 55–73. <https://doi.org/10.1007/978-1-60761-670-2>.
- (168) Zheng, R.; Park, B.-W.; Kim, D.-S.; Cameron, B. D. Development of a Highly Specific Amine-Terminated Aptamer Functionalized Surface Plasmon Resonance Biosensor for Blood Protein Detection. *Biomed. Opt. Express* **2011**, *2* (9), 2731. <https://doi.org/10.1364/boe.2.002731>.
- (169) Pan, B.; Fang, S.; Zhang, J.; Pan, Y.; Liu, H.; Wang, Y.; Li, M.; Liu, L. Chinese Herbal Compounds against SARS-CoV-2: Puerarin and Quercetin Impair the Binding of Viral S-Protein to ACE2 Receptor. *Comput. Struct. Biotechnol. J.* **2020**, *18*, 3518–3527. <https://doi.org/10.1016/j.csbj.2020.11.010>.
- (170) Vo, T.; Paul, A.; Kumar, A.; Boykin, D. W.; Wilson, W. D. Biosensor-Surface Plasmon Resonance : A Strategy to Help Establish a New Generation RNA-Specific Small Molecules. *Methods* **2019**, *167*, 15–27.
- (171) Devi, A.; Chaitanya, N. S. N. Designing of Peptide Aptamer Targeting the Receptor-binding Domain of Spike Protein of SARS-CoV-2:An in Silico Study. *Mol. Divers.* **2022**, *26*, 157–169. <https://doi.org/https://doi.org/10.1007/s11030-020-10171-6>.
- (172) Li, X.; Pei, Y.; Zhang, R.; Shuai, Q.; Wang, F.; Aastrup, T.; Pei, Z. A Suspension-Cell Biosensor for Real-Time Determination of Binding Kinetics of Protein–Carbohydrate Interactions on Cancer Cell Surfaces. *Chem. Commun.* **2013**, *49*, 9908–9910. <https://doi.org/10.1039/c3cc45006f>.
- (173) Park, T.; Choo, J.; Lee, M.; Kim, Y. S.; Lee, E. K.; Lee, H. S. Enhancement of the Protein Loading Density by a Pre-Cleaning Process of a Gold Substrate: Confocal Laser Scanning Microscopic Study. *Anal. Sci.* **2004**, *20* (9), 1255–1258. <https://doi.org/10.2116/analsci.20.1255>.
- (174) Jang, L. S.; Keng, H. K. Modified Fabrication Process of Protein Chips Using a Short-Chain Self-Assembled Monolayer. *Biomed. Microdevices* **2008**, *10* (2), 203–211. <https://doi.org/10.1007/s10544-007-9126-7>.
- (175) Zhu, H.; Lu, Y.; Xia, J.; Liu, Y.; Chen, J.; Lee, J.; Koh, K.; Chen, H. Aptamer-Assisted Protein Orientation on Silver Magnetic Nanoparticles: Application to Sensitive Leukocyte Cell-Derived Chemotaxin 2 Surface Plasmon Resonance Sensors. *Anal. Chem.* **2022**, *94* (4), 2109–2118. <https://doi.org/10.1021/acs.analchem.1c04448>.
- (176) Bartczak, D.; Kanaras, A. G. Preparation of Peptide-Functionalized Gold Nanoparticles Using One Pot EDC/Sulfo-NHS Coupling. *Langmuir* **2011**, *27* (16), 10119–10123. <https://doi.org/10.1021/la2022177>.
- (177) Mattson, G.; Conklin, E.; Desai, S.; Nielander, G.; Savage, M. D.; Morgensen, S. A

- Practical Approach to Crosslinking. *Mol. Biol. Rep.* **1993**, *17* (3), 167–183. <https://doi.org/10.1007/BF00986726>.
- (178) Figueroa-Miranda, G.; Feng, L.; Shiu, S. C. C.; Dirkzwager, R. M.; Cheung, Y. W.; Tanner, J. A.; Schöning, M. J.; Offenhäusser, A.; Mayer, D. Aptamer-Based Electrochemical Biosensor for Highly Sensitive and Selective Malaria Detection with Adjustable Dynamic Response Range and Reusability. *Sensors Actuators, B Chem.* **2018**, *255*, 235–243. <https://doi.org/10.1016/j.snb.2017.07.117>.
- (179) Tokmakov, A. A.; Kurotani, A.; Sato, K. I. Protein PI and Intracellular Localization. *Front. Mol. Biosci.* **2021**, *8*, 1–6. <https://doi.org/10.3389/fmolb.2021.775736>.
- (180) Song, X.; Shi, Y.; Ding, W.; Niu, T.; Sun, L.; Tan, Y.; Chen, Y.; Shi, J.; Xiong, Q.; Huang, X.; Xiao, S.; Zhu, Y.; Cheng, C.; Fu, Z. F.; Liu, Z.; Peng, G. Cryo-EM Analysis of the HCoV-229E Spike Glycoprotein Reveals Dynamic Prefusion Conformational Changes. *Nat. Commun.* **2021**, *12* (141), 1–9. <https://doi.org/10.1038/s41467-020-20401-y>.
- (181) Tu, J.; Xie, Y.; Xu, K.; Qu, L.; Lin, X.; Ke, C.; Yang, D.; Cao, G.; Zhou, Z.; Liu, Y. Treatment of Spleen-Deficiency Syndrome With Atractyloside A From Bran-Processed *Atractylodes Lancea* by Protection of the Intestinal Mucosal Barrier. *Front. Pharmacol.* **2020**, *11*, 1–13. <https://doi.org/10.3389/fphar.2020.583160>.
- (182) NicoyaLifeSciences. Detection and Binding Kinetics of SARS-CoV-2 Antibody with SARS-CoV-2 Spike Protein Receptor Binding Domain. Kitchener, Ontario.
- (183) Krebs, F.; Scheller, C.; Grove-Heike, K.; Pohl, L.; Wätzig, H. Isoelectric Point Determination by Imaged CIEF of Commercially Available SARS-CoV-2 Proteins and the HACE2 Receptor. *Electrophoresis* **2021**, *42* (6), 687–692. <https://doi.org/10.1002/elps.202100015>.
- (184) Gasteiger, H.; Hoogland, C.; Gattiker, A.; Duvaud, S.; Wilkins, M. R.; Appel, R. D.; Bairoch, A. Protein Identification and Analysis Tools on the ExPASy Server. In *The Proteomics Protocols Handbook*; Walker, J. M., Ed.; Humana Press, 2005; pp 571–607.
- (185) Bottari, F.; Daems, E.; De Vries, A. M.; Van Wielendaele, P.; Trashin, S.; Blust, R.; Sobott, F.; Madder, A.; Martins, J. C.; De Wael, K. Do Aptamers Always Bind? The Need for a Multifaceted Analytical Approach When Demonstrating Binding Affinity between Aptamer and Low Molecular Weight Compounds. *J. Am. Chem. Soc.* **2020**, *142* (46), 19622–19630. <https://doi.org/10.1021/jacs.0c08691>.
- (186) Hianik, T.; Ostatná, V.; Sonlajtnerova, M.; Grman, I. Influence of Ionic Strength, PH and Aptamer Configuration for Binding Affinity to Thrombin. *Bioelectrochemistry* **2007**, *70* (1), 127–133. <https://doi.org/10.1016/j.bioelechem.2006.03.012>.
- (187) Zull, J. E.; Reed-Mundell, J.; Lee, Y. W.; Vezenov, D.; Ziats, N. P.; Anderson, J. M.; Sukenik, C. N. Problems and Approaches in Covalent Attachment of Peptides

and Proteins to Inorganic Surfaces for Biosensor Applications. *J. Ind. Microbiol.* **1994**, *13* (3), 137–143. <https://doi.org/10.1007/BF01583997>.

- (188) Zuker, M. Mfold Web Server for Nucleic Acid Folding and Hybridization Prediction. *Nucleic Acids Res.* **2003**, *31* (13), 3406–3415. <https://doi.org/10.1093/nar/gkg595>.
- (189) Centers for Disease Control and Prevention. SARS (10 Years After) | Disease or Condition of the Week | CDC <https://www.cdc.gov/dotw/sars/index.html> (accessed Jun 22, 2022).
- (190) Wu, K.; Peng, G.; Wilken, M.; Geraghty, R. J.; Li, F. Mechanisms of Host Receptor Adaptation by Severe Acute Respiratory Syndrome Coronavirus. *J. Biol. Chem.* **2012**, *287* (12), 8904–8911. <https://doi.org/10.1074/jbc.M111.325803>.
- (191) Li, W.; Moore, M. J.; Vasilieva, N.; Sui, J.; Wong, S. K.; Berne, M. A.; Somasundaran, M.; Sullivan, J. L.; Luzuriaga, K.; Greenough, T. C.; Choe, H.; Farzan, M. Angiotensin-Converting Enzyme 2: A Functional Receptor for SARS Coronavirus. *Cell. Mol. Life Sci.* **2003**, *426*, 450–454. <https://doi.org/10.1038/nature02145>.
- (192) Kuhn, J. H.; Li, W.; Choe, H.; Farzan, M. Angiotensin-Converting Enzyme 2: A Functional Receptor for SARS Coronavirus. *Cell. Mol. Life Sci.* **2004**, *61* (21), 2738–2743. <https://doi.org/10.1007/s00018-004-4242-5>.
- (193) COVID19TreatmentGuidelinesPanel. *Coronavirus Disease 2019 (COVID-19) Treatment Guidelines*.
- (194) Wang, L.; Wu, Y.; Yao, S.; Ge, H.; Zhu, Y.; Chen, K.; Chen, W.; Zhang, Y.; Zhu, W.; Hong-yang, W.; Guo, Y.; Ma, P.; Ren, P.; Zhang, X.; Li, H.; Ali, M. A.; Xu, W.; Jiang, H.; Zhang, L.; Zhu, L.; Ye, Y.; Shang, W.; Bai, F. Discovery of Potential Small Molecular SARS-CoV-2 Entry Blockers Targeting the Spike Protein. *Acta Pharm. Sin. B* **2021**, 1–9.
- (195) Mei, J.; Zhou, Y.; Yang, X.; Zhang, F.; Liu, X.; Yu, B. Active Components in Ephedra Sinica Stapf Disrupt the Interaction between ACE2 and SARS-CoV-2 RBD: Potent COVID-19 Therapeutic Agents. *J. Ethnopharmacol.* **2021**, *278*, 114303. <https://doi.org/10.1016/j.jep.2021.114303>.
- (196) Yang, L. J.; Chen, R. H.; Hamdoun, S.; Coghi, P.; Ng, J. P. L.; Zhang, D. W.; Guo, X.; Xia, C.; Law, B. Y. K.; Wong, V. K. W. Corilagin Prevents SARS-CoV-2 Infection by Targeting RBD-ACE2 Binding. *Phytomedicine* **2021**, *87*, 153591. <https://doi.org/10.1016/j.phymed.2021.153591>.
- (197) Torabi, R.; Ranjbar, R.; Halaji, M.; Heiat, M. Aptamers, the Bivalent Agents as Probes and Therapies for Coronavirus Infections: A Systematic Review. *Mol. Cell. Probes* **2020**, *53* (April), 101636. <https://doi.org/10.1016/j.mcp.2020.101636>.
- (198) Peng, Y.; Du, N.; Lei, Y.; Dorje, S.; Qi, J.; Luo, T.; Gao, G. F.; Song, H. Structures of the SARS -CoV-2 Nucleocapsid and Their Perspectives for Drug Design . *EMBO*

J. **2020**, *39* (20), 1–12. <https://doi.org/10.15252/embj.2020105938>.

- (199) Vashist, S. K.; Vashist, S. K.; Schneider, E. M.; Luong, J. H. T. Surface Plasmon Resonance-Based Immunoassay for Human Fetuin A. *Analyst* **2014**, *139* (9), 2237–2242. <https://doi.org/10.1039/c4an00149d>.
- (200) Basso, C. R.; De Camargo Tozato, C.; Mendes Ribeiro, M. C.; Araujo Junior, J. P.; Pedrosa, V. A. A Immunosensor for the Diagnosis of Canine Distemper Virus Infection Using SPR and EIS. *Anal. Methods* **2013**, *5* (19), 5089–5095. <https://doi.org/10.1039/c3ay41087k>.
- (201) Suzuki, M.; Nakashima, Y.; Mori, Y. SPR Immunosensor Integrated Two Miniature Enzyme Sensors. *Sensors Actuators, B Chem.* **1999**, *54* (1), 176–181. [https://doi.org/10.1016/S0925-4005\(98\)00335-9](https://doi.org/10.1016/S0925-4005(98)00335-9).
- (202) Drake, A. W.; Klakamp, S. L. A Strategic and Systematic Approach for the Determination of Biosensor Regeneration Conditions. *J. Immunol. Methods* **2011**, *371* (1–2), 165–169. <https://doi.org/10.1016/j.jim.2011.06.003>.
- (203) Cui, X.; Yang, F.; Sha, Y.; Yang, X. Real-Time Immunoassay of Ferritin Using Surface Plasmon Resonance Biosensor. *Talanta* **2003**, *60* (1), 53–61. [https://doi.org/10.1016/S0039-9140\(03\)00043-2](https://doi.org/10.1016/S0039-9140(03)00043-2).
- (204) Soler, M.; Estevez, M. C.; Alvarez, M.; Otte, M. A.; Sepulveda, B.; Lechuga, L. M. Direct Detection of Protein Biomarkers in Human Fluids Using Site-Specific Antibody Immobilization Strategies. *Sensors (Switzerland)* **2014**, *14* (2), 2239–2258. <https://doi.org/10.3390/s140202239>.
- (205) Laffeber, C.; de Koning, K.; Kanaar, R.; Lebbink, J. H. G. Experimental Evidence for Enhanced Receptor Binding by Rapidly Spreading SARS-CoV-2 Variants. *J. Mol. Biol.* **2021**, *433* (15), 167058. <https://doi.org/10.1016/j.jmb.2021.167058>.
- (206) Barton, M. I.; Macgowan, S.; Kutuzov, M.; Dushek, O.; Barton, G. J.; Anton Van Der Merwe, P. Effects of Common Mutations in the Sars-Cov-2 Spike Rbd and Its Ligand the Human Ace2 Receptor on Binding Affinity and Kinetics. *Elife* **2021**, *10*, 1–19. <https://doi.org/10.7554/eLife.70658>.
- (207) Liang, P.; Canoura, J.; Yu, H.; Alkhamis, O.; Xiao, Y. Dithiothreitol-Regulated Coverage of Oligonucleotide-Modified Gold Nanoparticles to Achieve Optimized Biosensor Performance. *ACS Appl. Mater. Interfaces* **2018**, *10* (4), 4233–4242. <https://doi.org/10.1021/acsami.7b16914>.
- (208) Yu, S.; Zhu, Y.; Xu, J.; Yao, G.; Zhang, P.; Wang, M.; Zhao, Y.; Lin, G.; Chen, H.; Chen, L.; Zhang, J. Glycyrrhizic Acid Exerts Inhibitory Activity against the Spike Protein of SARS-CoV-2. *Phytomedicine* **2021**, *85*, 153364. <https://doi.org/10.1016/j.phymed.2020.153364>.
- (209) Torabi, R.; Ranjbar, R.; Halaji, M.; Heiat, M. Aptamers, the Bivalent Agents as Probes and Therapies for Coronavirus Infections: A Systematic Review. *Mol. Cell. Probes* **2020**, *53*, 101636. <https://doi.org/10.1016/j.mcp.2020.101636>.

Appendix i:

Supplementary Information (Chapter 2)

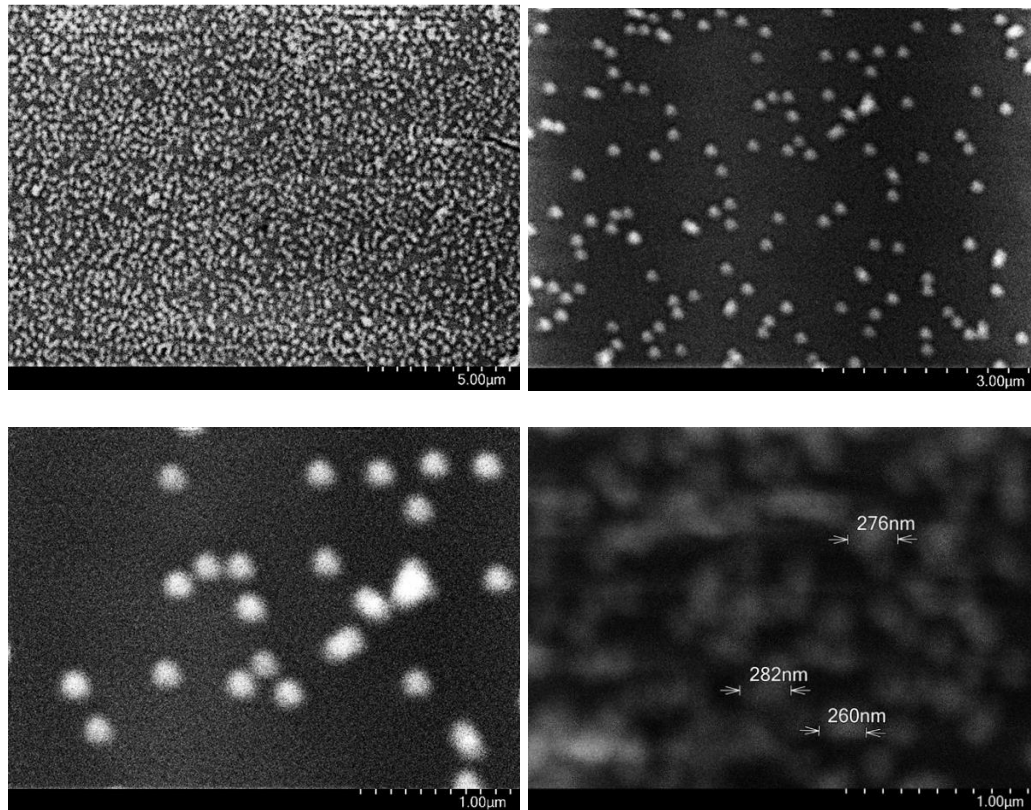


Figure A2.1. SEM images of LSPR chip at various magnifications. The chip surface contains biotin film on gold nanoparticles.

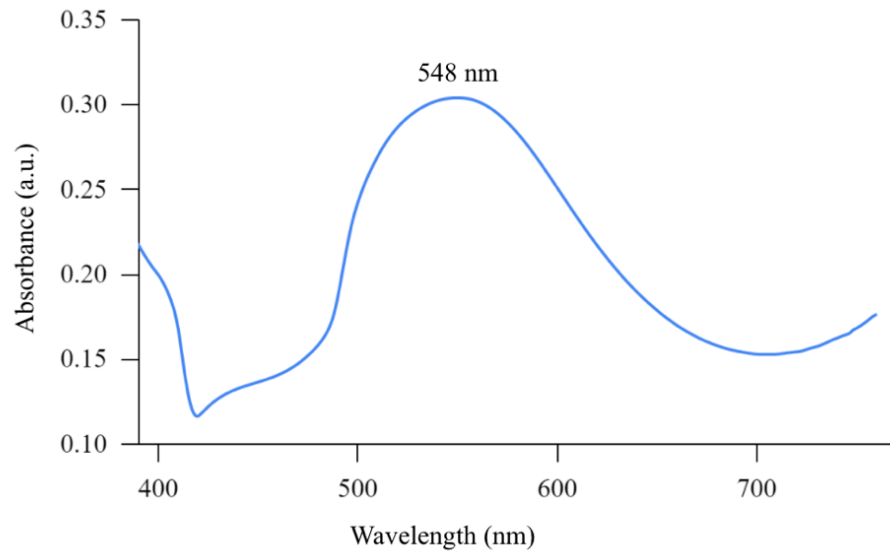


Figure A2.2. Absorbance spectrum of LSPR Biotin-Au chip.

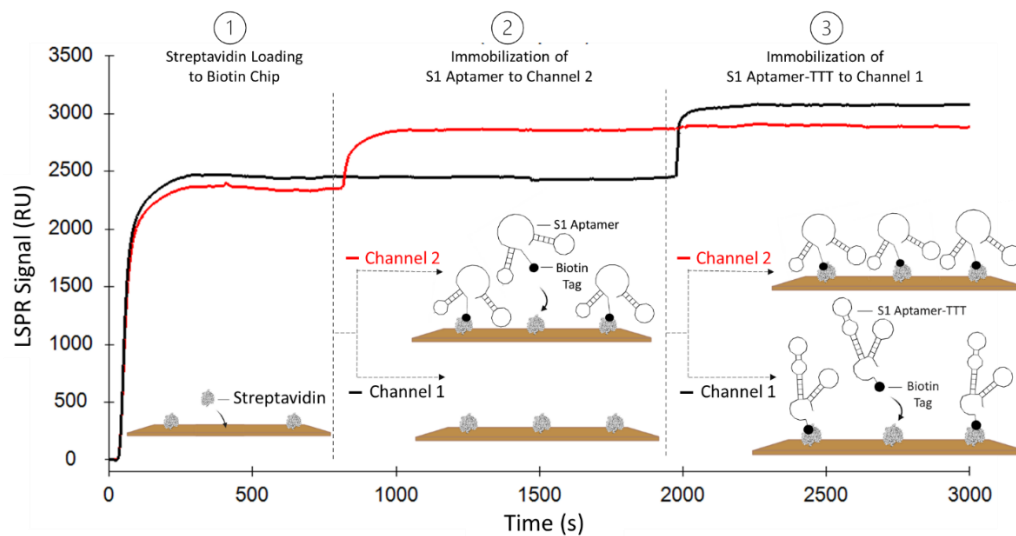


Figure A2.3. Sensorgram showing fabrication process involving streptavidin protein loading to the biotin-gold chip followed by immobilization of S1 and S1-T aptamers on two different channels ($[\text{streptavidin}] = 0.5 \mu\text{M}$; $[\text{S1 aptamer}] = 50 \mu\text{g/mL}$; $[\text{S1 aptamer-T}] = 50 \mu\text{g/mL}$; flow rate = $20 \mu\text{L/min}$).

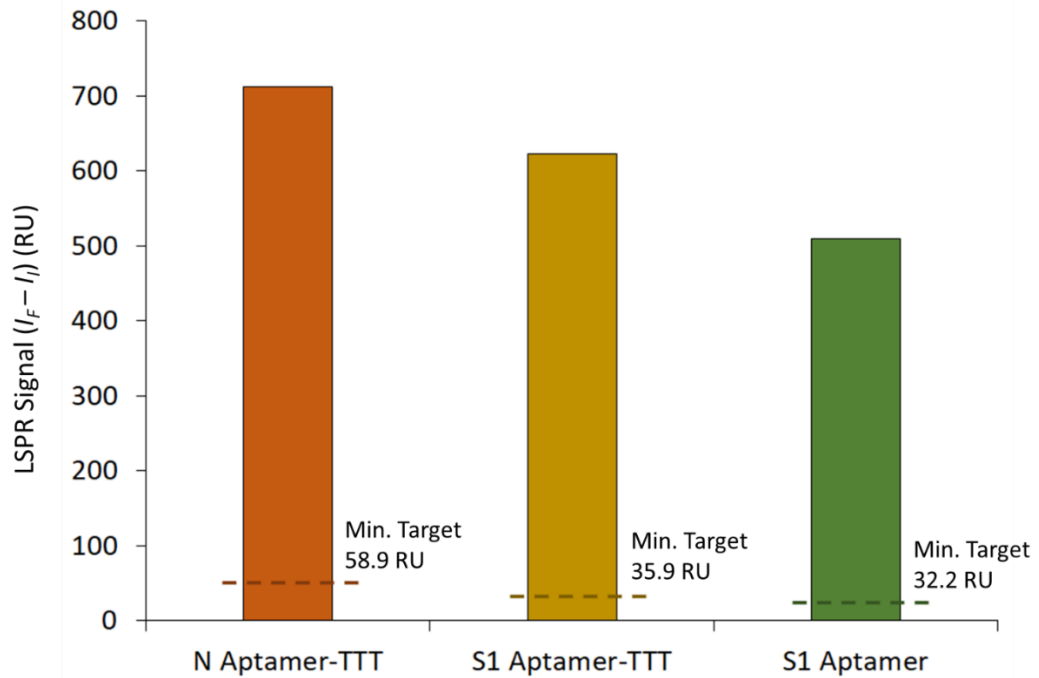


Figure A2.4. Signal response after immobilization of N, S1- and S1-T aptamer on individual channels with minimum target values provided for each ($[Aptamer] = 50 \mu\text{g/mL}$).

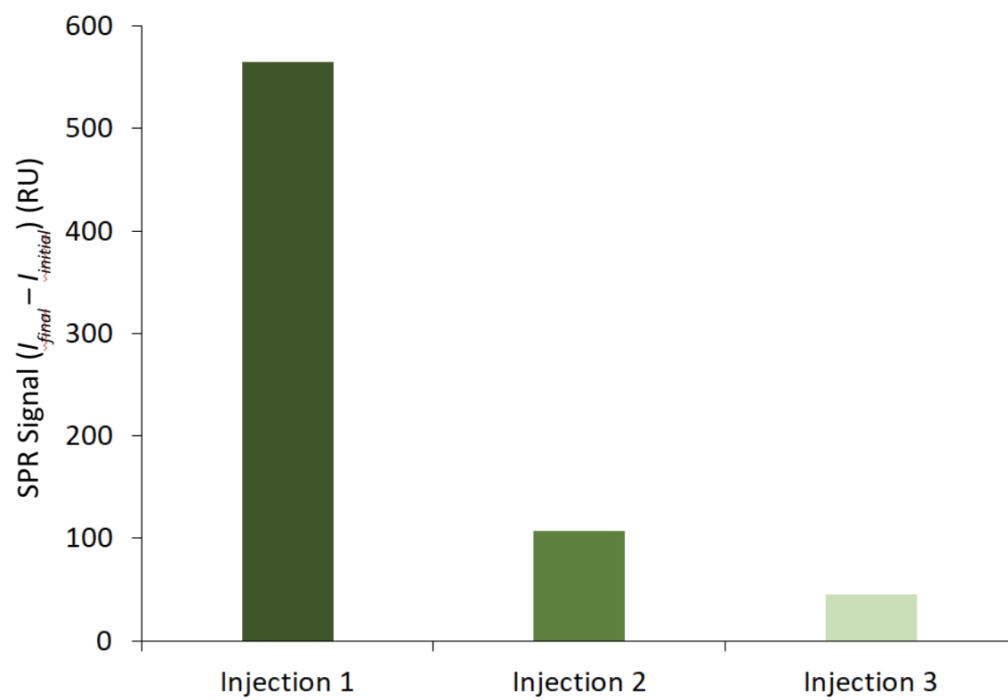


Figure A2.5. Signal response after immobilization of S1 aptamer with 3 subsequent aptamer injections ($[Aptamer] = 16 \mu\text{g/mL}$).

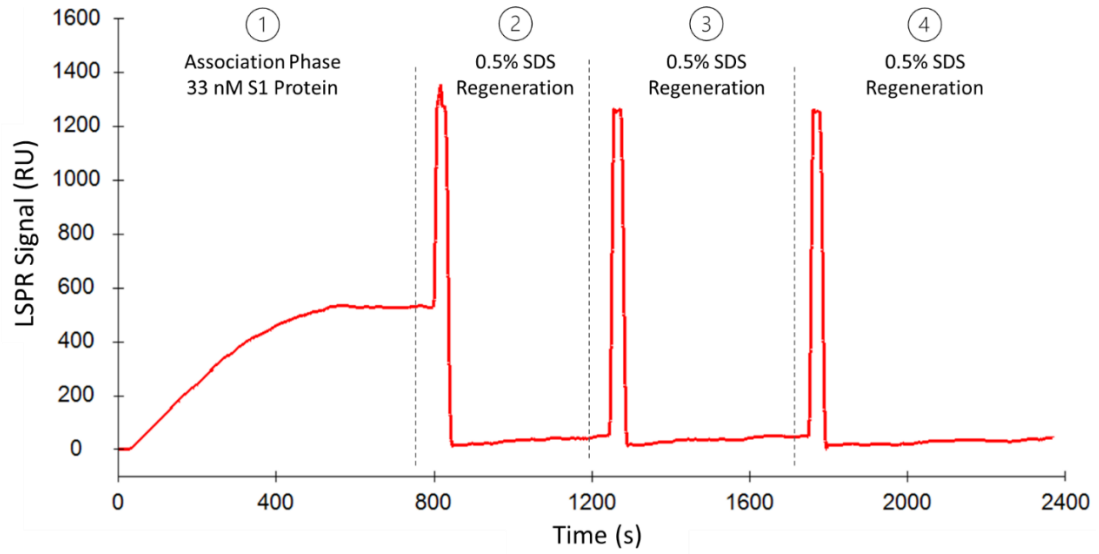


Figure A2.6. Representative sensorgram of the S1 protein binding (1) followed by the regeneration optimization with subsequent injections of 0.5% SDS buffer (2-3) ([S1 Protein] = 33 nM (2.5 $\mu\text{g}/\text{mL}$), regeneration flow rate = 150 $\mu\text{L}/\text{min}$).

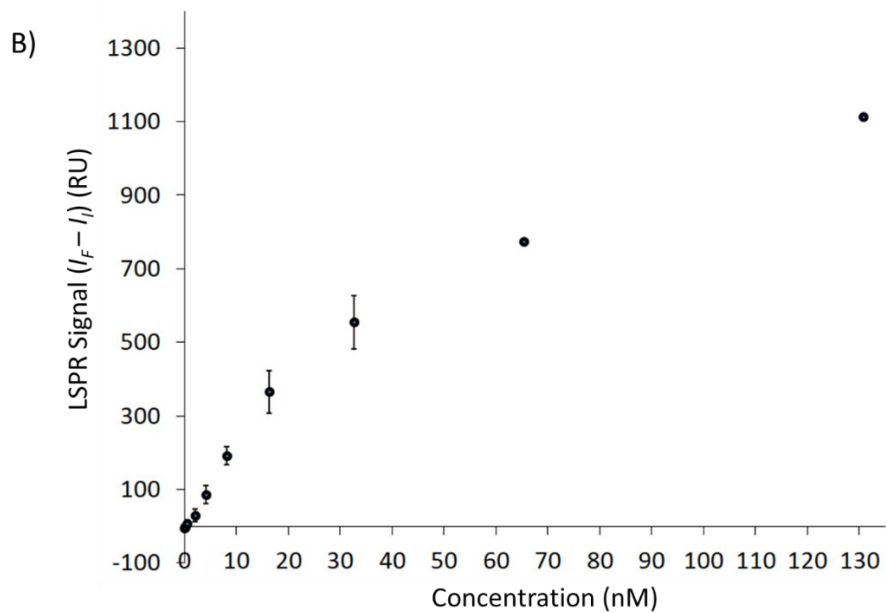
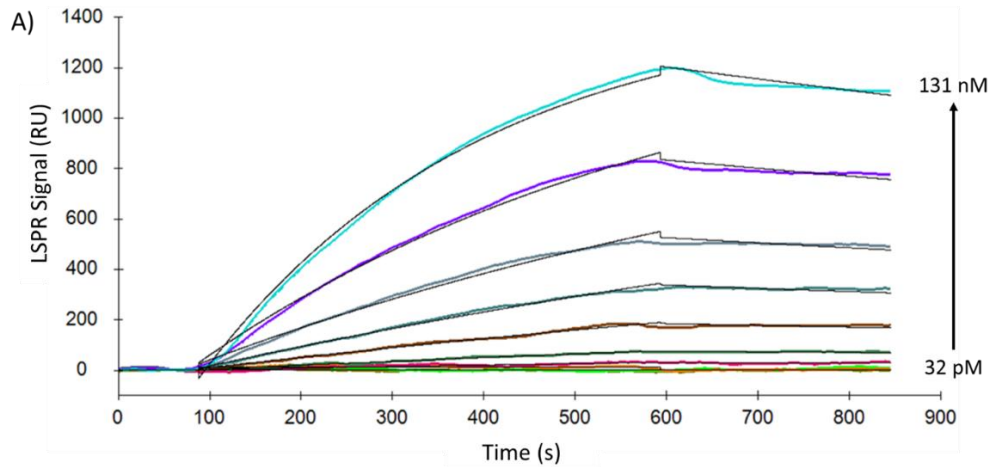


Figure A2.7. (A) Representative sensorgram of fitted data (black lines) for varying concentrations of S1 protein (colored lines) using the S1 aptasensor ([S1 protein] = 32 pM to 131 nM). (B) LSPR signal change as a function of S1 protein concentration determined from sensorgram (A) ([S1 protein] = 0 to 131 nM).

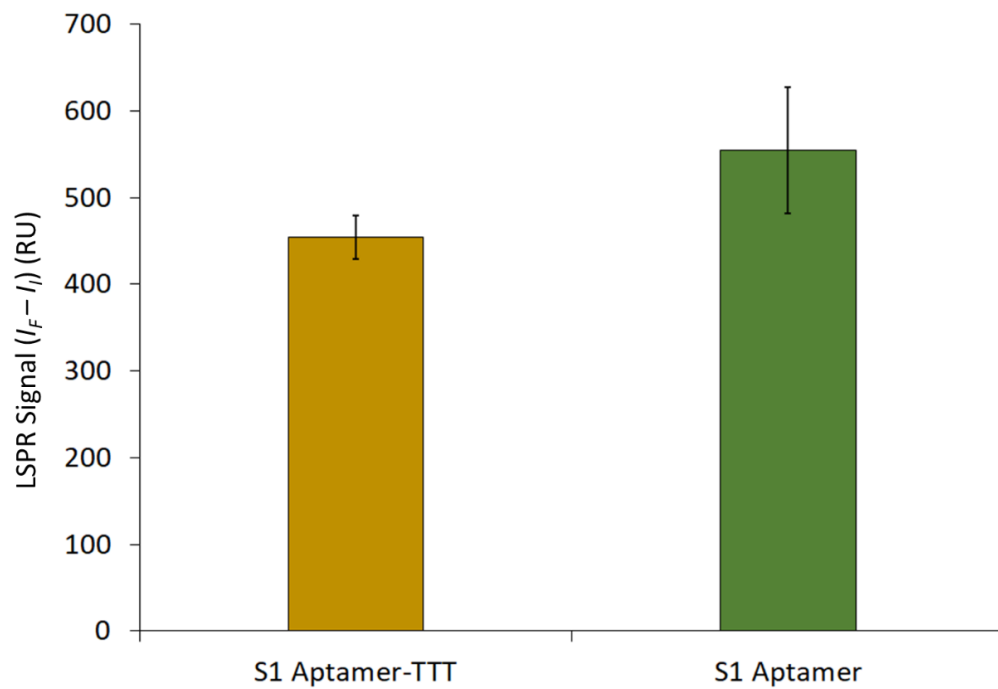


Figure A2.8. Comparison of LSPR signal responses for S1 protein using the S1 Aptamer-T or the S1 Aptamer ([Aptamer] = 50 $\mu\text{g/mL}$, data represent average and error bars of triplicate measurements).

Table A2.1. Experimental fitting parameters for various SARS-CoV-2 proteins using S1 aptamer

Protein	k_a (1/M*s)	k_d (1/s)	K_D (nM)
SARS-CoV-2 S1	$9.26 \times 10^4 \pm 1.05 \times 10^4$	$3.72 \times 10^{-5} \pm 1.66 \times 10^{-5}$	0.41 ± 0.23
SARS-CoV-2 S2	$2.37 \times 10^5 \pm 3.82 \times 10^4$	$1.51 \times 10^{-3} \pm 4.03 \times 10^{-4}$	6.29 ± 0.69
SARS-CoV-2 RBD	$4.10 \times 10^4 \pm 1.13 \times 10^3$	$6.98 \times 10^{-4} \pm 5.40 \times 10^{-4}$	17.28 ± 13.75

Table A2.2. Experimental fitting parameters for various SARS-CoV-2 proteins using S1-T aptamer

Protein	k_a (1/M*s)	k_d (1/s)	K_D (nM)
SARS-CoV-2 S1	$6.65 \times 10^4 \pm 1.22 \times 10^4$	$1.01 \times 10^{-4} \pm 5.19 \times 10^{-5}$	1.48 ± 0.7
SARS-CoV-2 S2	$1.86 \times 10^5 \pm 9.39 \times 10^4$	$1.84 \times 10^{-2} \pm 2.91 \times 10^{-2}$	104.13 ± 160.2
SARS-CoV-2 RBD	$8.25 \times 10^4 \pm 3.36 \times 10^3$	$5.02 \times 10^{-4} \pm 8.21 \times 10^{-4}$	5.94 ± 9.7

Table A2.3. Experimental fitting parameters for various SARS-CoV-2 proteins using N-T aptamer

Protein	k_a (1/M*s)	k_d (1/s)	K_D (nM)
SARS-CoV-2 S1	$2.22 \times 10^5 \pm 9.05 \times 10^4$	$8.44 \times 10^{-4} \pm 3.62 \times 10^{-4}$	3.78 ± 0.07
SARS-CoV-2 S2	$3.92 \times 10^4 \pm 2.55 \times 10^4$	$4.55 \times 10^{-2} \pm 1.08 \times 10^{-2}$	2389.67 ± 2867.2
SARS-CoV-2 RBD	$1.52 \times 10^5 \pm 1.83 \times 10^5$	$7.87 \times 10^{-3} \pm 8.78 \times 10^{-3}$	152.69 ± 167.1

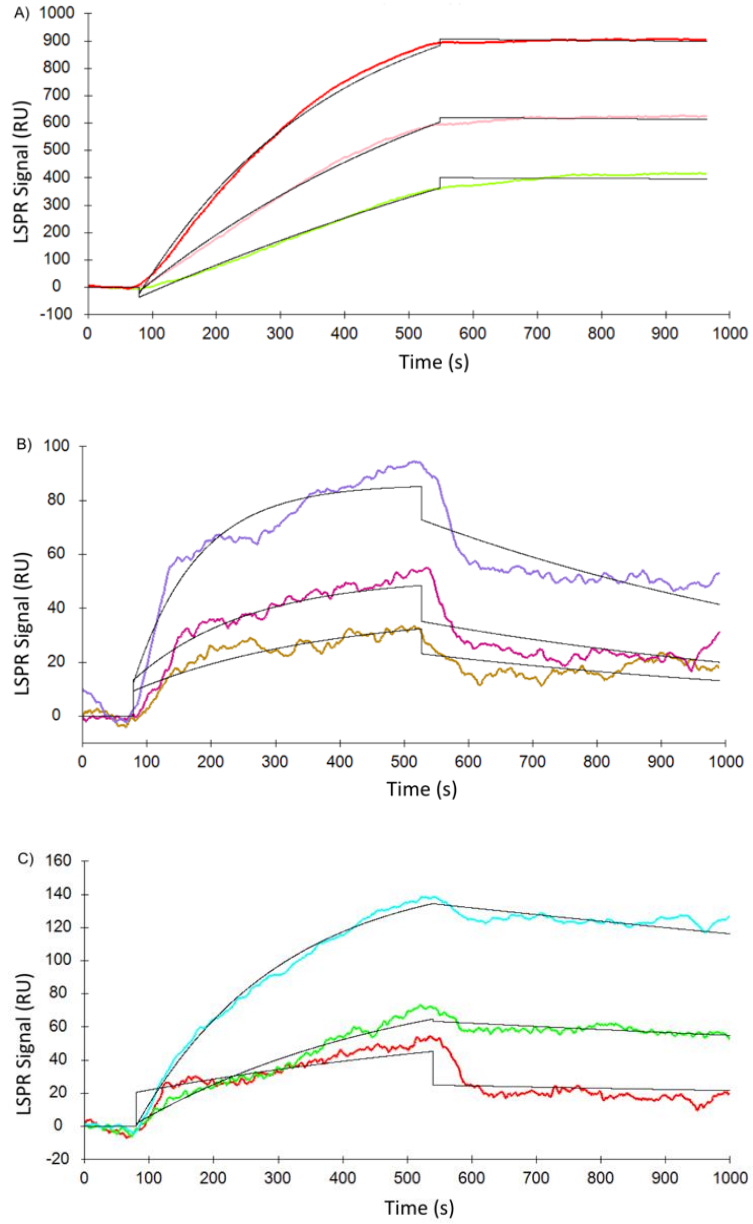


Figure A2.9. Representative sensorgrams of fitted data (black lines) for varying concentrations of A) S1 protein (colored lines), B) S2 protein, C) RBD protein using the S1 aptasensor ($[\text{protein}] = 0 - 2.5 \mu\text{g/mL}$).

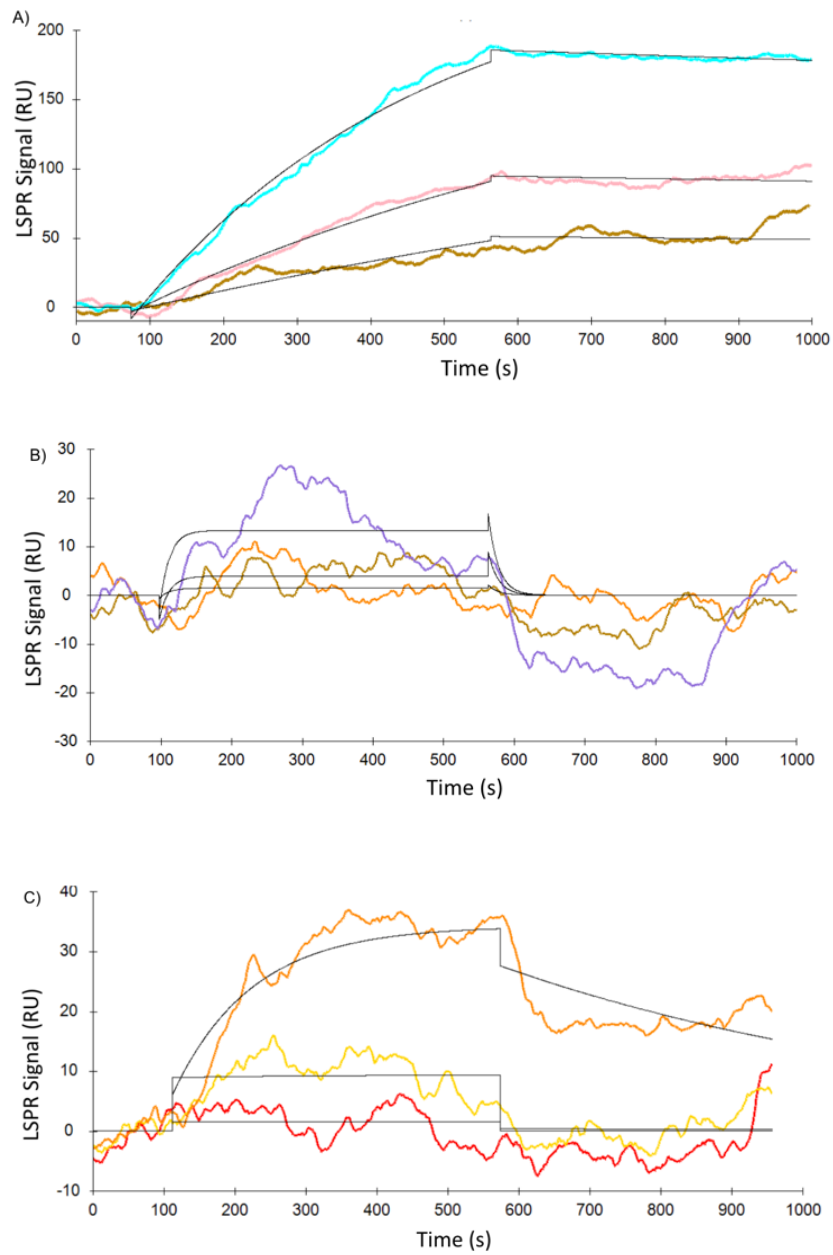


Figure A2.10. Representative sensorgrams of fitted data (black lines) for varying concentrations of A) S1 protein (colored lines), B) S2 protein, C) RBD protein using the S1-T aptasensor ($[\text{protein}] = 0 - 2.5 \mu\text{g/mL}$).

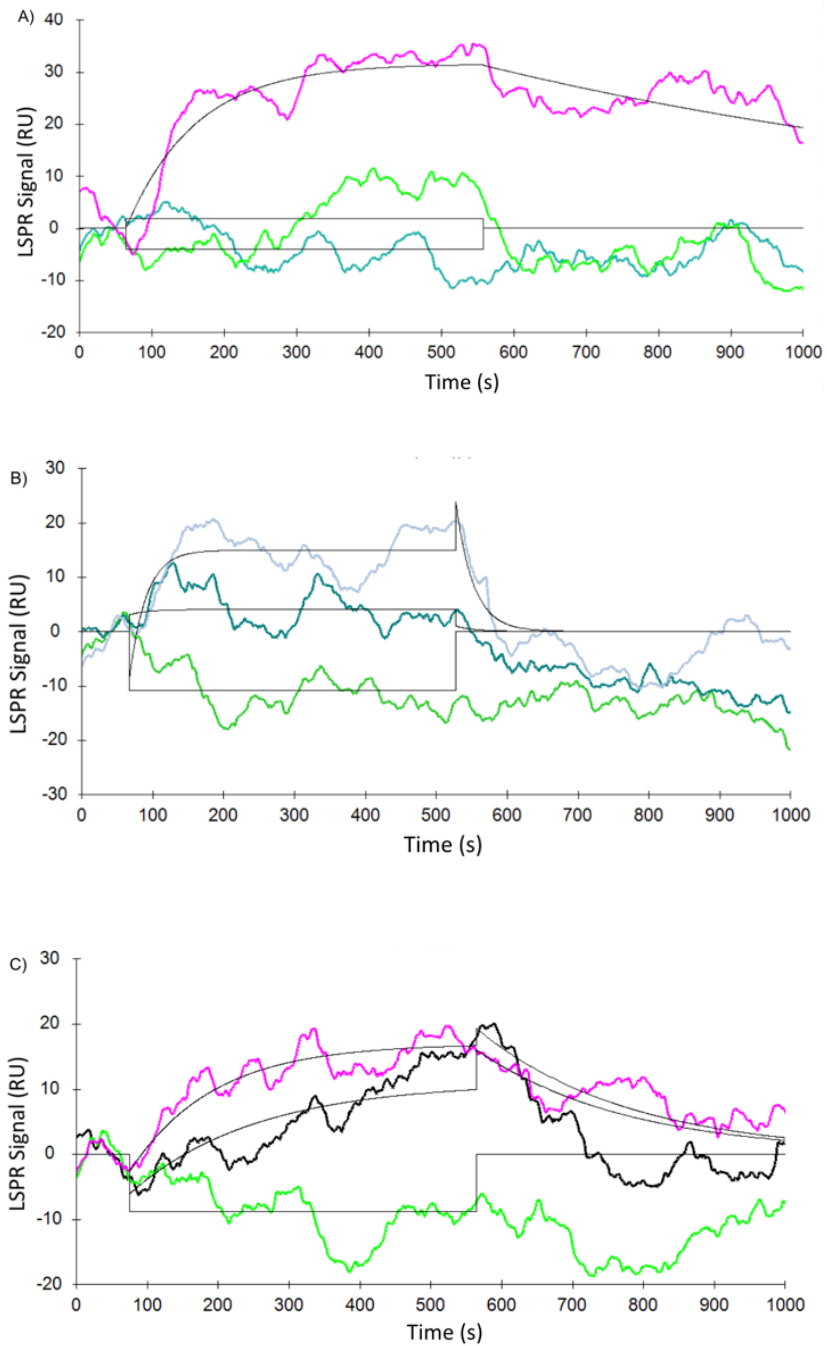


Figure A2.11. Representative sensorgrams of fitted data (black lines) for varying concentrations of A) S1 protein (colored lines), B) S2 protein, C) RBD protein using the N-T aptasensor ($[\text{protein}] = 0 - 2.5 \mu\text{g/mL}$).

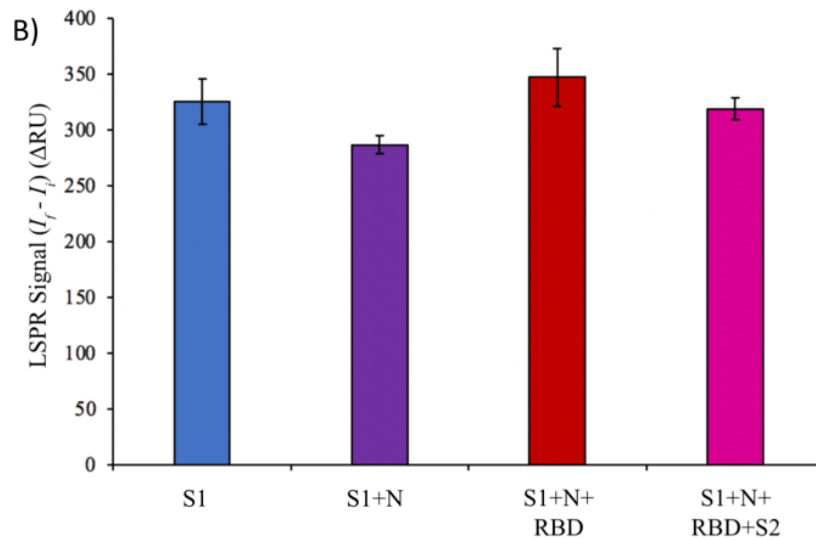
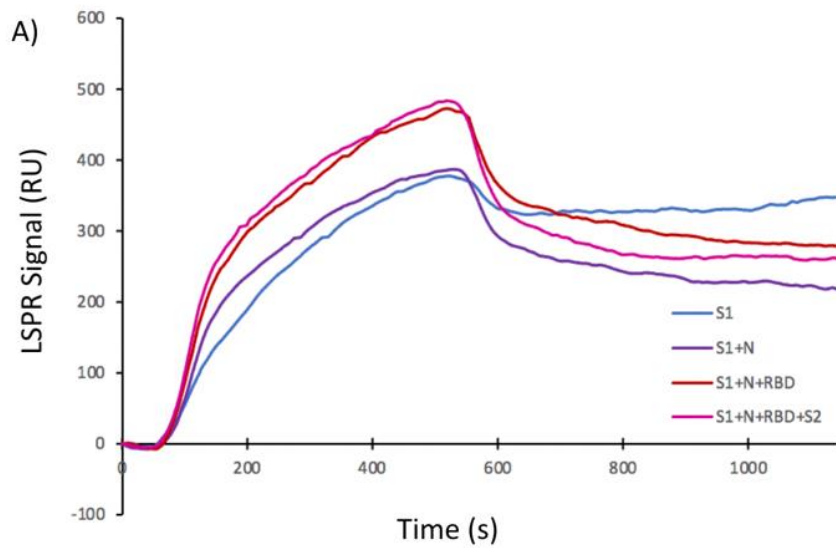


Figure A2.12. A) Representative sensorgram and B) plot of LSPR signals at $t=610$ s, of SARS-CoV-2 S1, and various mixtures; S1+N, S1+N+RBD, S1+N+RBD+S2 ([each protein] = $2.5 \mu\text{g/mL}$).

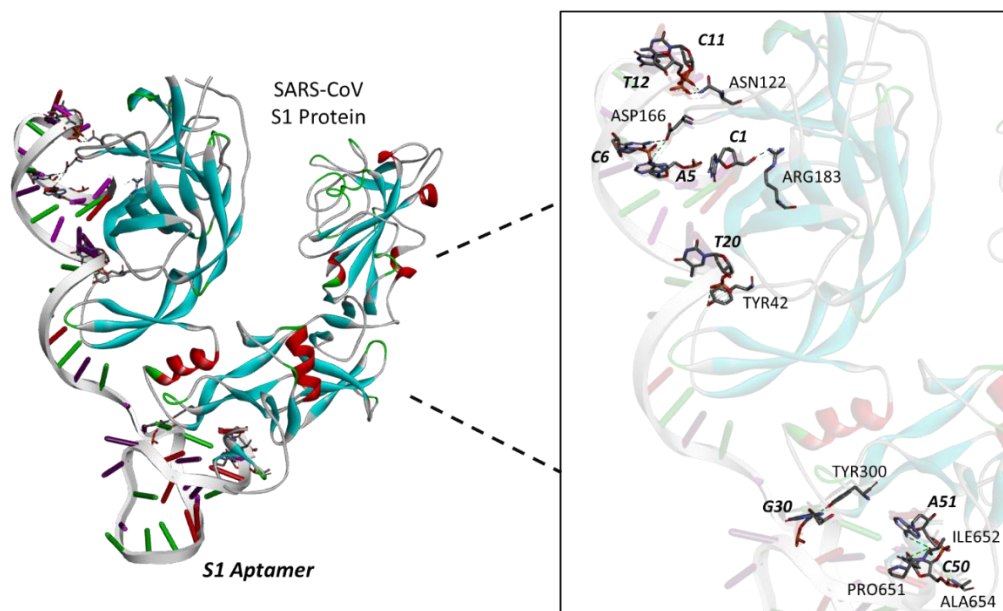


Figure A2.13. Molecular docking modelling of SARS-CoV S1 protein (PDB ID: 6CRZ) and S1 aptamer using PatchDock WebServer and visualized with Discovery Studio Visualizer Software.

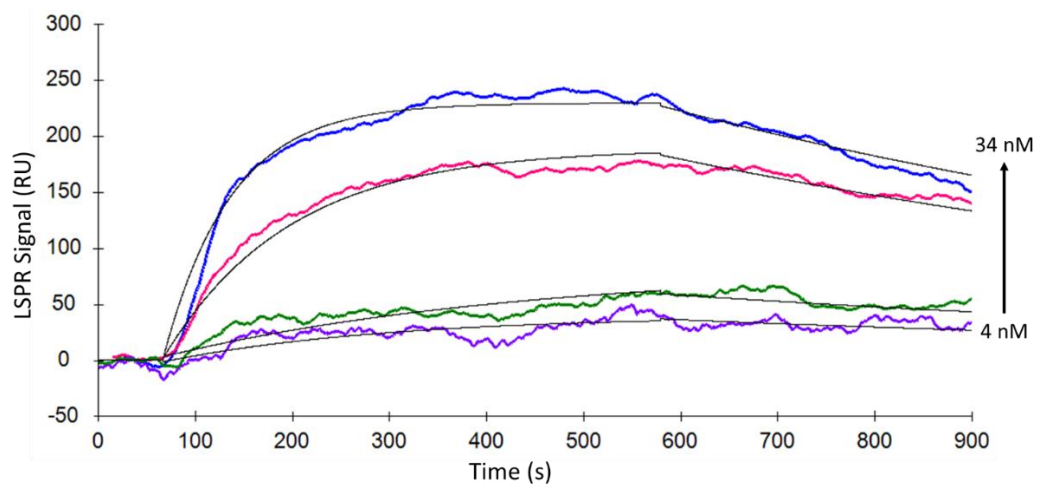


Figure A2.14. Representative sensorgram of fitted data (black lines) for various concentrations of SARS-CoV S1 protein (colored lines) using the S1 aptasensor ([SARS CoV S1] = 4.2, 8.4, 16.8 and 33.6 nM (0.3 to 2.5 $\mu\text{g/mL}$)).

Table A2.4. Curve fitting data for SARS-CoV S1 protein with the S1 aptasensor. The 1:1 binding model was used in the TraceDrawer Software to obtain the k_a , k_d , and K_D values.

Values represent triplicate measurements.

	k_a (1/M*s)	k_d (1/s)	K_D (nM)
SARS-CoV	$3.99 \times 10^5 \pm 2.65 \times 10^4$	$1.17 \times 10^{-3} \pm 2.10 \times 10^{-4}$	2.9 ± 0.4

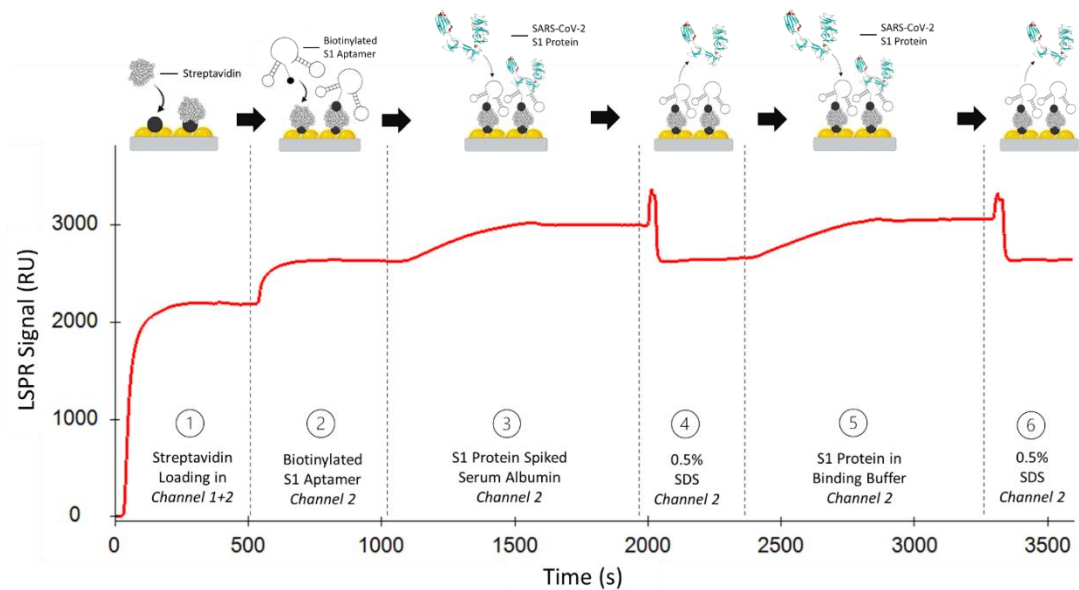


Figure A2.15. Sensorgram showing sensor fabrication and performance: (1) streptavidin protein loading to the biotin-gold chip (flow rate = 20 $\mu\text{L}/\text{min}$); followed by (2) immobilization of S1 aptamer (flow rate = 20 $\mu\text{L}/\text{min}$); then (3) injection of 1000x diluted serum albumin spiked with S1 protein sample (flow rate = 10 $\mu\text{L}/\text{min}$); (4) surface regeneration with 0.5% SDS (flow rate = 150 $\mu\text{L}/\text{min}$); (5) injection of S1 protein in buffer (flow rate = 20 $\mu\text{L}/\text{min}$); (6) surface regeneration with 0.5% SDS (flow rate = 150 $\mu\text{L}/\text{min}$) ([streptavidin] = 0.5 μM ; [S1 aptamer] = 50 $\mu\text{g}/\text{mL}$; [S1 protein] = 0.25 $\mu\text{g}/\text{mL}$).

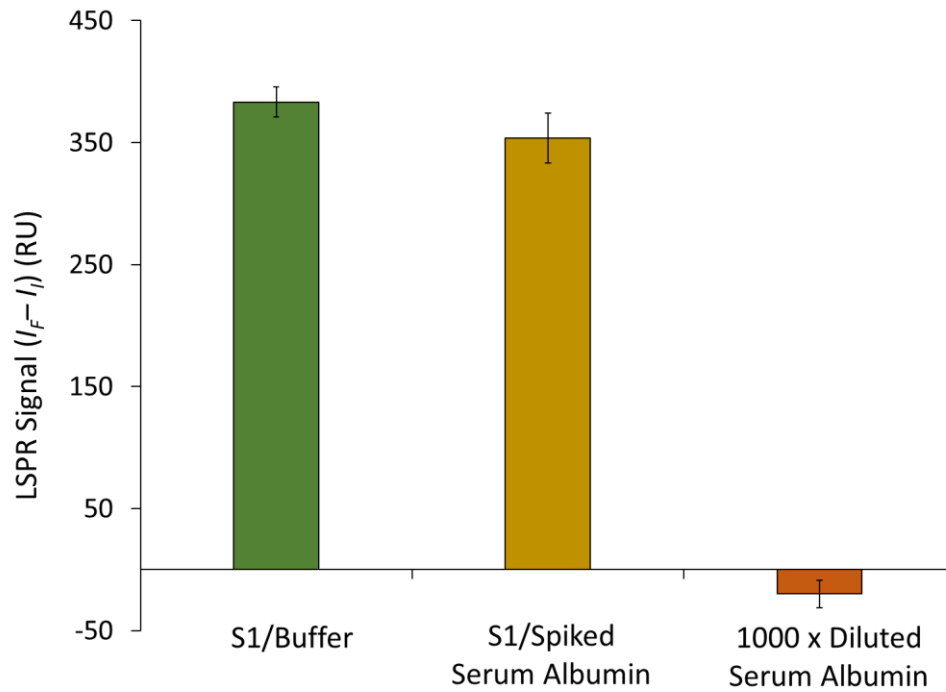


Figure A2.16. Plot of LSPR signal change for SARS-CoV-2 S1 protein in spiked buffer solution compared to the 1000x diluted spiked serum albumin solution with or without S1 protein ([S1 Protein] = 2.5 $\mu\text{g/mL}$; signals represent average of triplicate measurements with standard deviations shown as error bars).

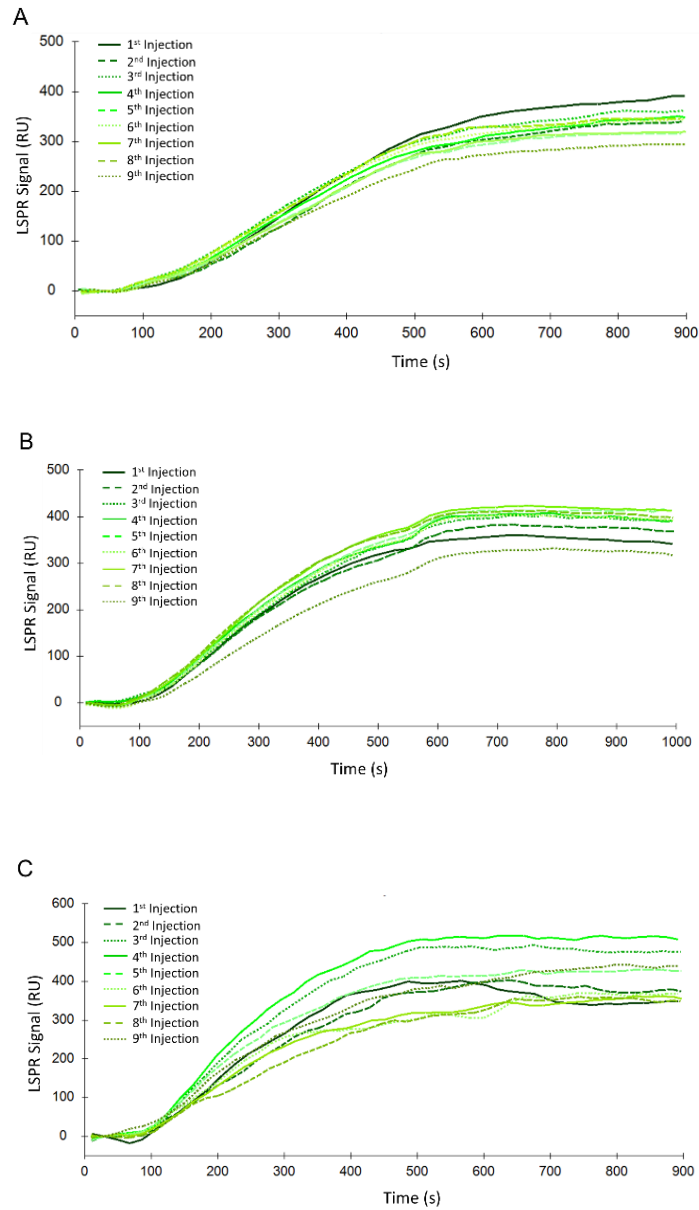


Figure A2.17. Representative sensorgrams showing repeatability of the SARS-CoV-2 S1 protein injections using offline prepared S1 aptamer sensor after specific storage time: (A) at $t = 0$ days; (B) $t = 10$ days; (C) $t = 24$ days (all S1 protein injections were followed by regeneration using 0.5% SDS buffer; [S1 Protein] = 1 $\mu\text{g/mL}$).

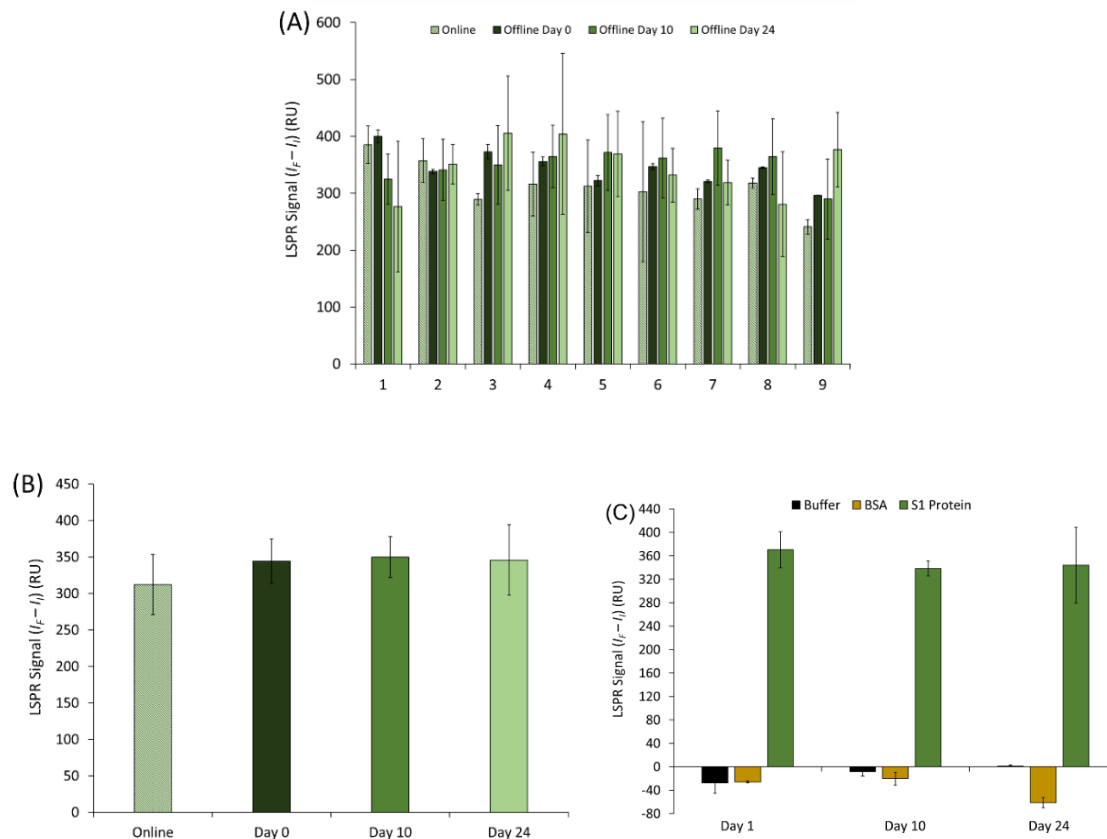


Figure A2.18. (A) LSPR signals for 9 repeat injections of S1 protein using the online sensor or offline-prepared sensor with the shelf-life = 0, 10 or 24 days (data represent average of duplicate measurements with error bars showing standard deviation); (B) Average LSPR signals for the online or offline-prepared sensors used for 9 repeat injections of S1 protein on 0, 10 or 24 days; (C) Average LSPR signals for the offline-prepared sensor used for triplicate injections of blank buffer, BSA and S1 Protein ($[S1 \text{ protein}] = [BSA] = 1 \mu\text{g/mL}$; regeneration conditions = 0.5% SDS).

Appendix ii:

Supplementary Information (Chapter 3)

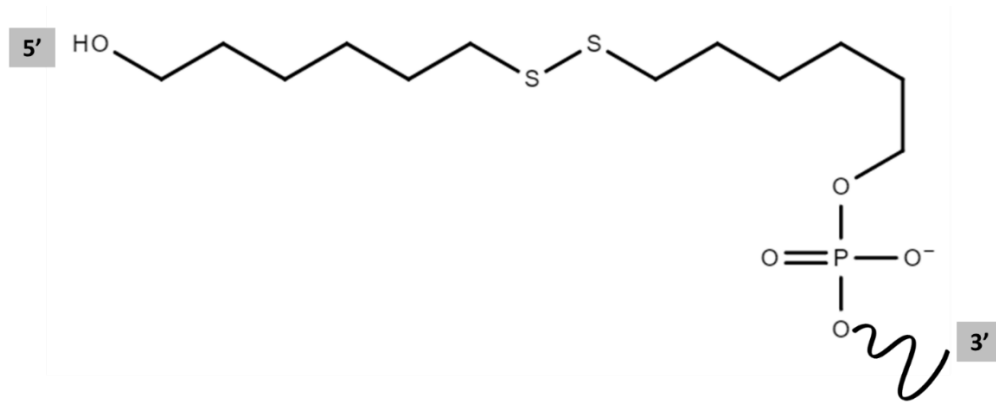


Figure A3.1. Structural illustration of the 5'-thiol modification of the aptamer (represented by the scribbled line) with a 6-carbon chain spacer.

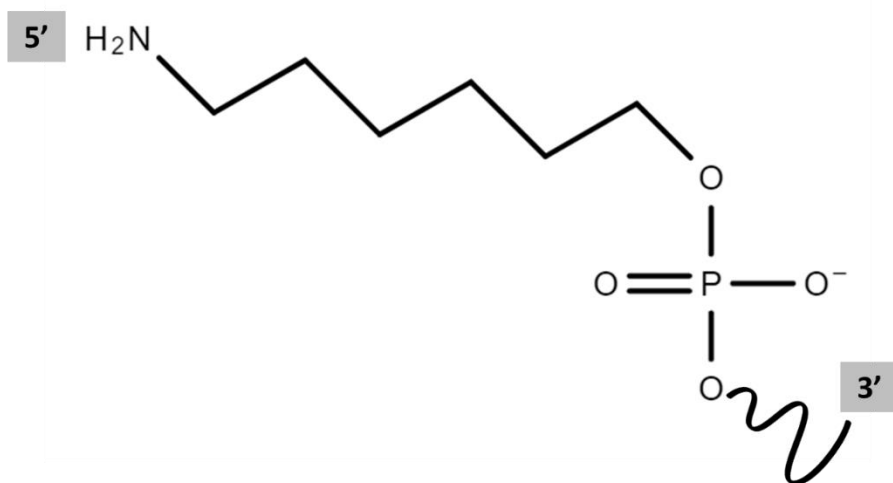


Figure A3.2. Structural illustration of the amine modification positioned at the 5'-end of the aptamer (represented by the scribbled line) with a 6-carbon chain spacer.

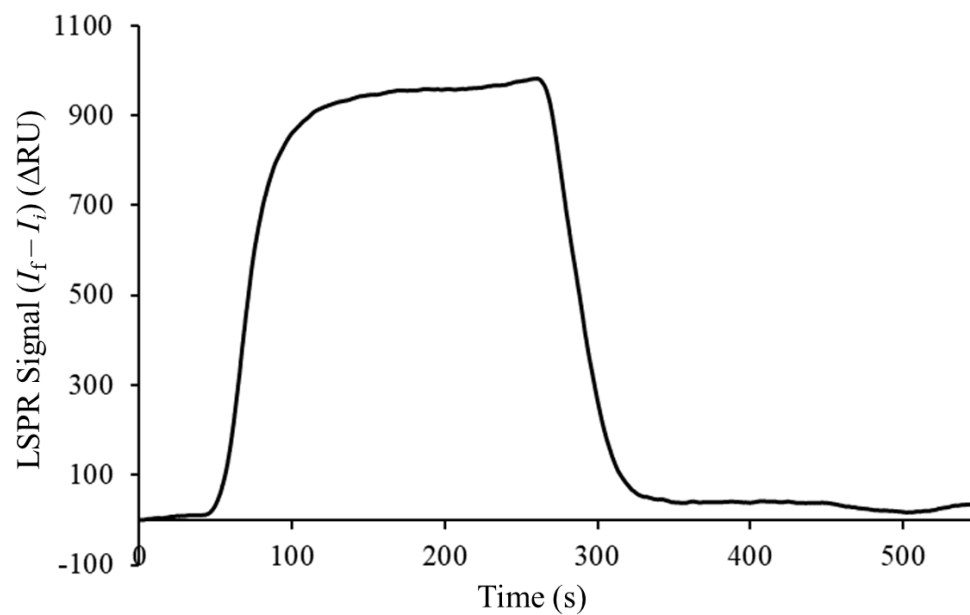


Figure A3.3. Representative sensorgram showing NH_2 -aptamer injection after completion of surface activation; [aptamer] = 50 $\mu\text{g}/\text{mL}$; flow rate = 20 $\mu\text{L}/\text{min}$.

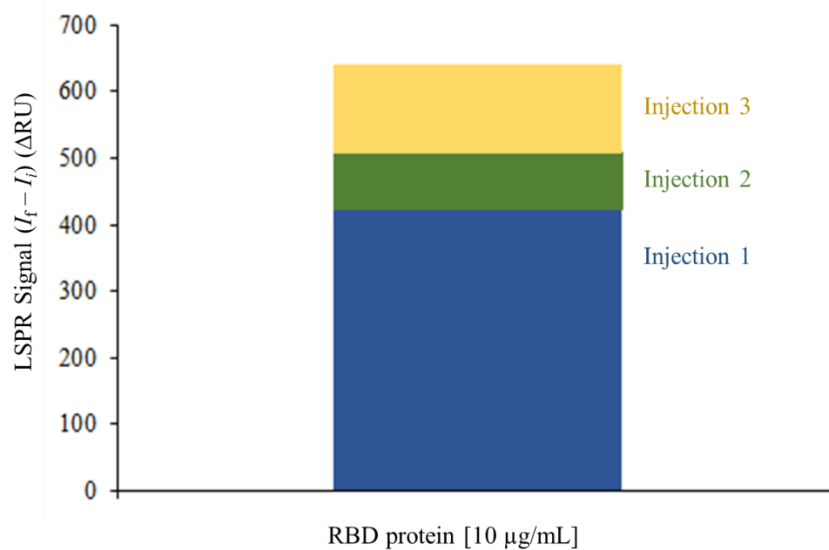
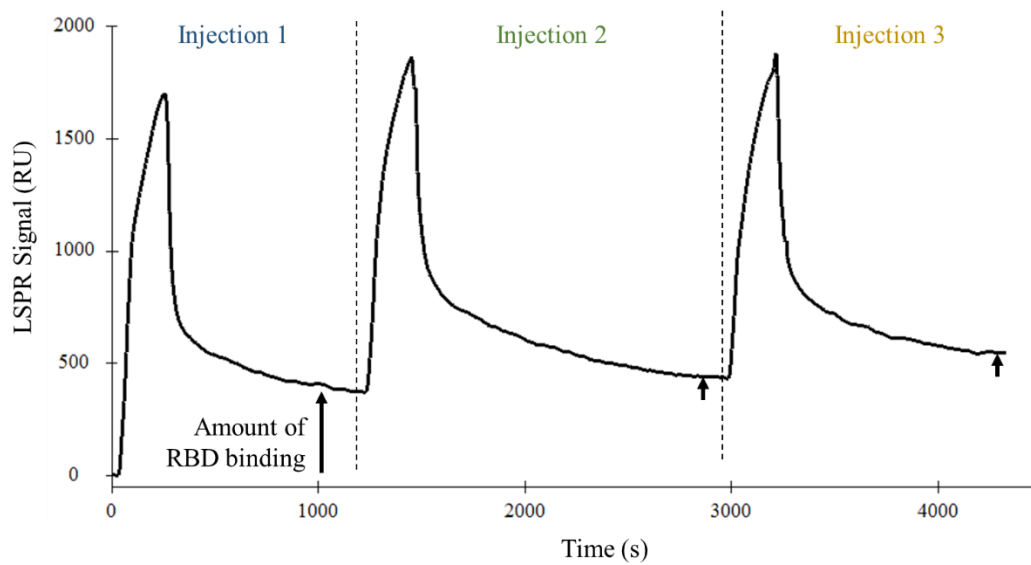


Figure A3.4. Representative sensorgram and average LSPR signal change with sequential addition of RBD protein; for each injection; [RBD] = 10 $\mu\text{g/mL}$; flow rate = 20 $\mu\text{L/min}$.

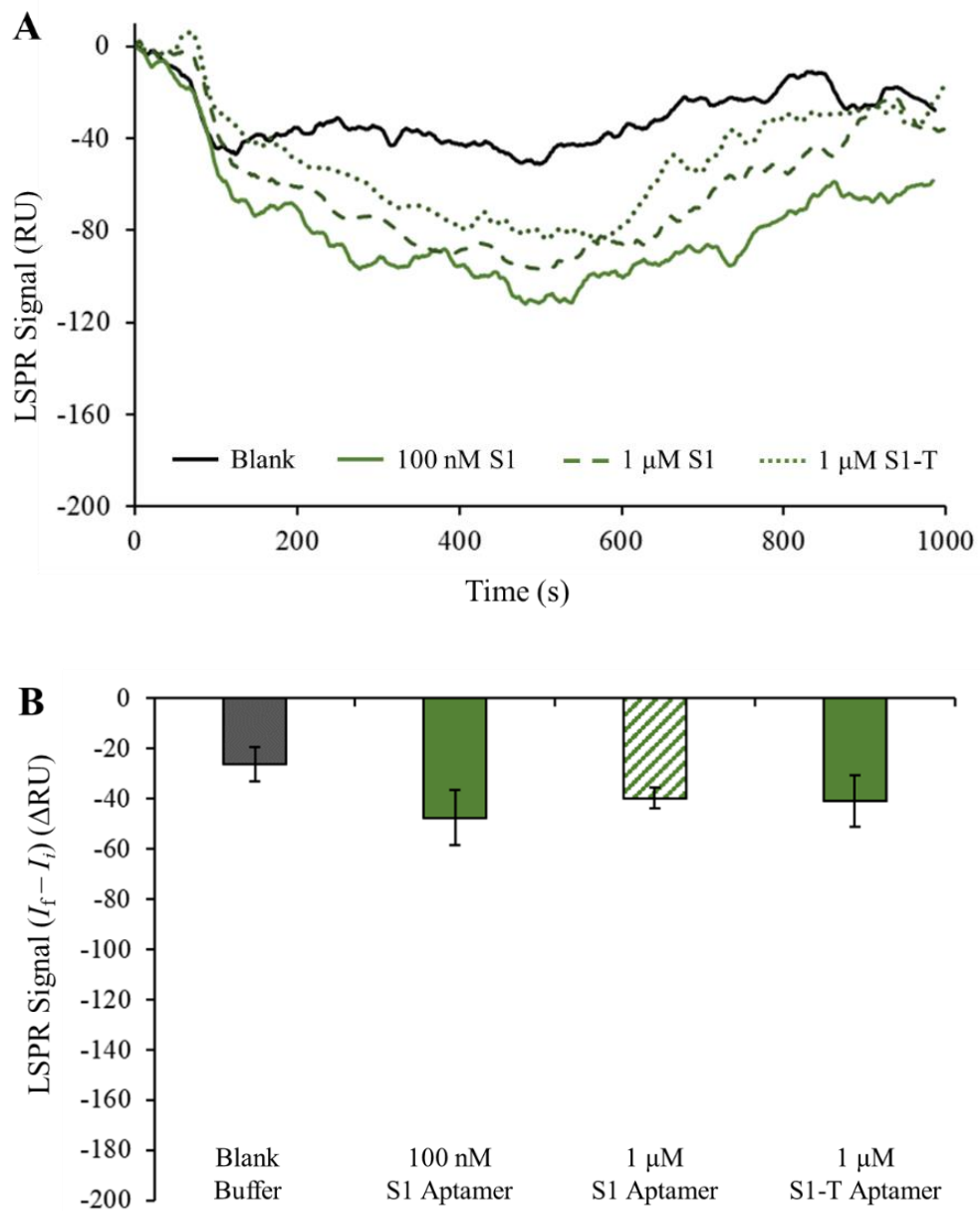


Figure A3.5. (A) Representative LSPR signals and (B) plot of LSPR signal comparison with blank buffer, S1 and S1-T aptamers using the RBD functionalized carboxyl surface; immobilized [RBD] = 25 μ g/mL; [S1 aptamer] = 100 nM or 1 μ M; [S1-T aptamer] = 1 μ M; flow rate = 10 μ L/min; (I_f = 800 s).

Appendix iii:

Supplementary Information (Chapter 4)

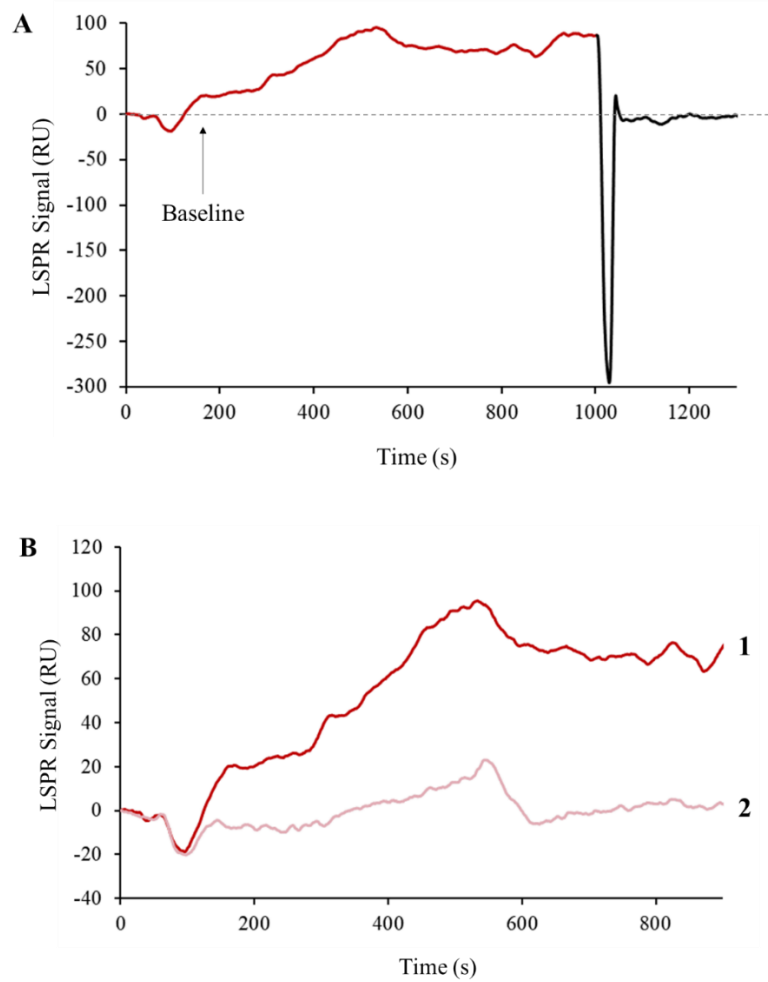


Figure A4.1. Representative LSPR sensorgrams demonstrating (A) ACE2 binding to a RBD functionalized carboxyl surface followed by regeneration using 10 mM glycine-HCl solution and (B) ACE2 signals prior (1) and post (2) regeneration with glycine-HCl; immobilized [RBD] = 10 $\mu\text{g/mL}$; [ACE2] = 100 nM; flow rate (ACE2) = 10 $\mu\text{L/min}$; flow rate (regeneration) = 150 $\mu\text{L/min}$.

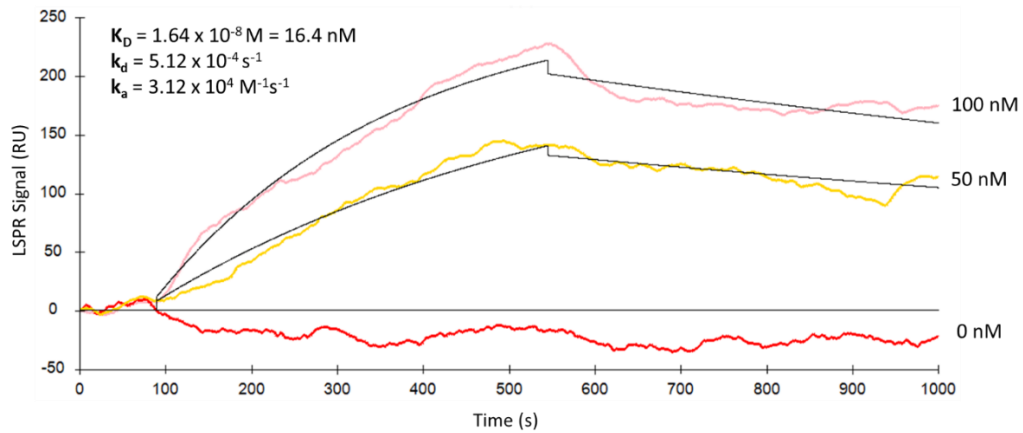
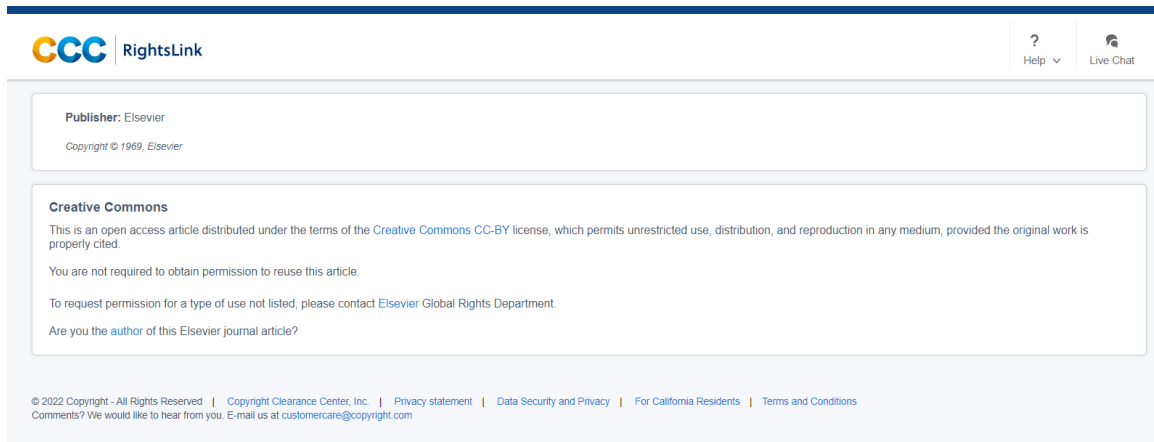


Figure A4.2. Representative LSPR sensorgrams of 0-100 nM ACE2 using the RBD functionalized carboxyl surface fitted using a 1:1 binding model for calculation of k_a , k_d and K_D values; immobilized [RBD] = 25 $\mu\text{g/mL}$; flow rate = 10 $\mu\text{L/min}$; regeneration of RBD-ACE2 interaction with 10 mM HCl, flow rate = 150 $\mu\text{L/min}$.

Appendix iv:

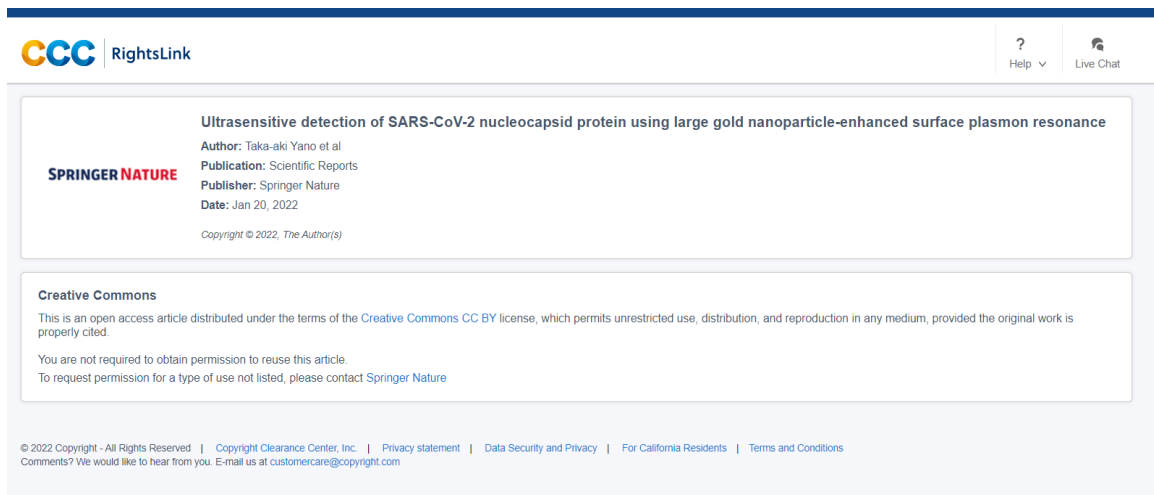
Copyright Releases

Figure 1.4B [Rightslink® by Copyright Clearance Center:](#)



The screenshot shows the RightsLink interface for Elsevier content. At the top left is the CCC RightsLink logo. At the top right are links for Help and Live Chat. The main content area is divided into two sections. The first section, titled "Publisher: Elsevier", includes the text "Copyright © 1969, Elsevier". The second section, titled "Creative Commons", contains the following text: "This is an open access article distributed under the terms of the Creative Commons CC-BY license, which permits unrestricted use, distribution, and reproduction in any medium, provided the original work is properly cited." "You are not required to obtain permission to reuse this article." "To request permission for a type of use not listed, please contact Elsevier Global Rights Department." "Are you the author of this Elsevier journal article?" At the bottom of the page, there is a footer with copyright information and contact details: "© 2022 Copyright - All Rights Reserved | Copyright Clearance Center, Inc. | Privacy statement | Data Security and Privacy | For California Residents | Terms and Conditions Comments? We would like to hear from you. E-mail us at customercare@copyright.com"

Figure 1.4C [Rightslink® by Copyright Clearance Center:](#)



The screenshot shows the RightsLink interface for Springer Nature content. At the top left is the CCC RightsLink logo. At the top right are links for Help and Live Chat. The main content area is divided into two sections. The first section, titled "Ultrasensitive detection of SARS-CoV-2 nucleocapsid protein using large gold nanoparticle-enhanced surface plasmon resonance", includes the following information: "Author: Taka-aki Yano et al", "Publication: Scientific Reports", "Publisher: Springer Nature", "Date: Jan 20, 2022", and "Copyright © 2022, The Author(s)". The Springer Nature logo is also present. The second section, titled "Creative Commons", contains the following text: "This is an open access article distributed under the terms of the Creative Commons CC BY license, which permits unrestricted use, distribution, and reproduction in any medium, provided the original work is properly cited." "You are not required to obtain permission to reuse this article." "To request permission for a type of use not listed, please contact Springer Nature". At the bottom of the page, there is a footer with copyright information and contact details: "© 2022 Copyright - All Rights Reserved | Copyright Clearance Center, Inc. | Privacy statement | Data Security and Privacy | For California Residents | Terms and Conditions Comments? We would like to hear from you. E-mail us at customercare@copyright.com"

Chapter 2 was published in *Analyst* 2021, Issue 23

Lewis, T.; Giroux, E.; Jovic, M.; Martic-Milne, S. Localized Surface Plasmon Resonance Aptasensor for Selective Detection of SARS-CoV-2 S1 Protein. *Analyst* 2021, 146, 7207-7217. doi: <https://doi.org/10.1039/D1AN01458G>

The screenshot shows the article page for 'Localized surface plasmon resonance aptasensor for selective detection of SARS-CoV-2 S1 protein' in the journal *Analyst*, Issue 23, 2021. The authors listed are Tyra Lewis, Erin Giroux, Marko Jovic, and Sanela Martic-Milne. The abstract states: 'In this work, we designed and developed a method to detect S1 spike protein of SARS-CoV-2. The portable Localized Surface Plasmon Resonance instrument equipped with a two-channel system was combined with the biotin-streptavidin platform on a nanogold surface to immobilize biotinylated aptamers. The proposed assay does not utilize antibodies or enzyme-based reagents, further simplifying the detection method. Using aptamer-protein bioaffinity interactions, the aptasensor selectively and specifically detected in real-time S1 spike protein, rather than S2 spike protein.' On the right side, there is a 'Cited by' tab with a pop-up window containing the following text: 'Localized surface plasmon resonance aptasensor for selective detection of SARS-CoV-2 S1 protein', 'T. Lewis, E. Giroux, M. Jovic and S. Martic-Milne, *Analyst*, 2021, 146, 7207 DOI: 10.1039/D1AN01458G', 'To request permission to reproduce material from this article, please go to the [Copyright Clearance Center request page](#).', 'If you are an author contributing to an RSC publication, you do not need to request permission provided correct acknowledgement is given.', 'If you are the author of this article, you do not need to request permission to reproduce figures and diagrams provided correct acknowledgement is given. If you want to reproduce the whole article in a third-party publication (excluding your thesis/dissertation for which permission is not required) please go to the [Copyright Clearance Center request page](#).', and 'Read more about [how to correctly acknowledge RSC content](#).'

Figure 3.2B:



This is a License Agreement between Tyra Lewis ("User") and Copyright Clearance Center, Inc. ("CCC") on behalf of the Rightsholder identified in the order details below. The license consists of the order details, the Marketplace Order General Terms and Conditions below, and any Rightsholder Terms and Conditions which are included below. All payments must be made in full to CCC in accordance with the Marketplace Order General Terms and Conditions below.

Order Date	21-Jul-2022	Type of Use	Republish in a thesis/dissertation
Order License ID	1249988-1	Publisher	Royal Society of Chemistry
ISSN	1364-5528	Portion	Chart/graph/table/figure

LICENSED CONTENT

Publication Title	The analyst online	Publication Type	e-Journal
Article Title	Aptamer-based biochips for label-free detection of plant virus coat proteins by SPR imaging.	Start Page	918
Author/Editor	Society of Public Analysts (Great Britain), Chemical Society (Great Britain), Society for Analytical Chemistry, Society of Public Analysts (Great Britain), Royal Society of Chemistry (Great Britain)	End Page	926
Date	01/01/1876	Issue	5
Language	English	Volume	135
Country	United Kingdom of Great Britain and Northern Ireland	URL	http://www.rsc.org/is/journals/current/an...
Rightsholder	Royal Society of Chemistry		

REQUEST DETAILS

Portion Type	Chart/graph/table/figure	Distribution	Canada
Number of charts / graphs / tables / figures requested	1	Translation	Original language of publication
Format (select all that apply)	Print, Electronic	Copies for the disabled?	No
Who will republish the content?	Academic institution	Minor editing privileges?	No
Duration of Use	Life of current edition	Incidental promotional use?	No
Lifetime Unit Quantity	Up to 499	Currency	CAD
Rights Requested	Main product		

NEW WORK DETAILS

Title	SARS-CoV-2 protein-based detection using localized surface plasmon resonance	Institution name	Trent University
Instructor name	Dr. Sanela Martić	Expected presentation date	2022-08-01

ADDITIONAL DETAILS

Order reference number	N/A	The requesting person / organization to appear on the license	Tyra Lewis
------------------------	-----	---	------------

REUSE CONTENT DETAILS

Title, description or numeric reference of the portion(s)	Figure 1	Title of the article/chapter the portion is from	Aptamer-based biochips for label-free detection of plant virus coat proteins by SPR imaging.
Editor of portion(s)	Lautner, Gergely; Balogh, Zsolt; Bardócz, Viola; Mészáros, Tamás; Gyurcsányi, Róbert E.	Author of portion(s)	Lautner, Gergely; Balogh, Zsolt; Bardócz, Viola; Mészáros, Tamás; Gyurcsányi, Róbert E.
Volume of serial or monograph	135	Issue, if republishing an article from a serial	5
Page or page range of portion	918-926	Publication date of portion	2010-05-01

Figure 3.2C:

ELSEVIER LICENSE TERMS AND CONDITIONS

Jul 21, 2022

This Agreement between Ms. Tyra Lewis ("You") and Elsevier ("Elsevier") consists of your license details and the terms and conditions provided by Elsevier and Copyright Clearance Center.		Type of Use	reuse in a thesis/dissertation
License Number	5353790493704	Portion	figures/tables/illustrations
License date	Jul 21, 2022	Number of figures/tables/illustrations	1
Licensed Content Publisher	Elsevier	Format	both print and electronic
Licensed Content Publication	Biosensors and Bioelectronics	Are you the author of this Elsevier article?	No
Licensed Content Title	Development of a label-free SPR sensor for detection of matrixmetalloproteinase-9 by antibody immobilization on carboxymethylidextran chip	Will you be translating?	No
Licensed Content Author	Sara Mohseni, Tahereh Tohidi Moghadam, Bahareh Dabirmanesh, Safoura Jabbari, Khosro Khajeh	Title	SARS-CoV-2 protein-based detection using localized surface plasmon resonance
Licensed Content Date	Jul 15, 2016	Institution name	Trent University
Licensed Content Volume	81	Expected presentation date	Aug 2022
Licensed Content Issue	n/a	Portions	Figure 1
Licensed Content Pages	7	Requestor Location	Ms. Tyra Lewis Trent University
Start Page	510	Publisher Tax ID	Peterborough, ON K9L 0G2 Canada Attn: Tyra Lewis
End Page	516		
Type of Use	reuse in a thesis/dissertation		GB 494 6272 12

Figure 4.1:

SPRINGER NATURE LICENSE TERMS AND CONDITIONS

Jul 21, 2022

This Agreement between Ms. Tyra Lewis ("You") and Springer Nature ("Springer Nature") consists of your license details and the terms and conditions provided by Springer Nature and Copyright Clearance Center.

License Number 5353791049106

License date Jul 21, 2022

Licensed Content Publisher Springer Nature

Licensed Content Publication Nature

Licensed Content Title Structure of the SARS-CoV-2 spike receptor-binding domain bound to the ACE2 receptor

Licensed Content Author Jun Lan et al

Licensed Content Date Mar 30, 2020

Type of Use Thesis/Dissertation

Requestor type academic/university or research institute

Format print and electronic

Portion figures/tables/illustrations

Number of figures/tables/illustrations 1

High-res required no

Will you be translating? no

Format print and electronic

Portion figures/tables/illustrations

Number of figures/tables/illustrations 1

High-res required no

Will you be translating? no

Circulation/distribution 1 - 29

Author of this Springer Nature content no

Title SARS-CoV-2 protein-based detection using localized surface plasmon resonance

Institution name Trent University

Expected presentation date Aug 2022

Portions Extended Figure 4

Ms. Tyra Lewis
Trent University

Requestor Location Peterborough, ON K9L 0G2
Canada
Attn: Tyra Lewis